Plaster modelling of fault development and geometry in contractional settings

Marie Djupevåg Eri

Master of science thesis

Department of Earth Science

UNIVERSITY OF BERGEN

June 2015

Abstract

The aim of this study has been to analyse the development of contractional structures using analogue plaster models. Structures similar to natural fault systems are generated using plaster of Paris as the deforming medium and barite as basement. Detailed studies of plaster models are useful in the understanding of sub seismic features related to faults and to understand 4D evolution of contractional faults.

Six experiments have been analysed based on photos and videos. Characteristic parameters regarding thrust fault development have been investigated including; main fault activity, fault dip evolution, fault displacement, fault spacing, wedge height and geometry, folds and secondary faults. The analysis revealed that faults initiated at the base of the models and propagated upwards forming a wider monoclinal fault-propagation fold in front, whereas in other cases, faults initiated as sets of conjugated shears. Faults initiated had an average dip between 29° and 35°. In most of the models, the faults developed as in-sequence thrusts where mainly one fault was active at any given time. Initiation point of the first faults varies between 1-7% shortening and was strongly controlled by the plaster properties. The wedge geometry and angle varied from 16°-62° and was controlled by the firmness of plaster were more firm plaster created a higher wedge angle. Through balancing of an experiment, three dominant deformation mechanisms are established; layer parallel shortening (LPS), folding and thrusting. Different domains within the model throughout the experimental period was recorded; the front of the wedge was dominated by fault ramp initiation and thrust propagation, the middle was characterised by rotation, steepening and eventual locking of the faults due to the effect of imbrication, whereas the back of the wedge was dominated by vertical thickening. A trend of stepwise increase in imbricate thrust spacing and a decrease in rate of initiation of imbricate thrusts in the transport direction is evident. The latest and thereby the youngest faults developed larger displacement than the older faults, most likely due to increased mechanical strength of the plaster. Smaller structures such as pop ups, fault splay, antithetic and synthetic minor faults forms in association with main faults.

Acknowledgements

This thesis is a part of my Master's Degree in geodynamics and has been written at the Department of Earth Science at the University of Bergen.

I would like to take this opportunity to thank all the people that have contributed academically and practically to support me during the work with this master thesis. First of all, I would like to thank my head supervisor Haakon Fossen (UiB, Department of Earth Science) for his time, valuable inputs and support over the last two years. I would also like to thank my co-supervisors Eivind Bastesen (UNI/CIPR), Atle Rotevatn (Department of Earth Science), Tore Odinsen (STATOIL) and Signe Ottesen (STATOIL) for valuable ideas and comments throughout the time I have been working on this project. Also, thank you to Hamed Fazli Khani (UiB, Department of Earth Science) for his engagement.

Secondly, I would like to thank my friends and fellow students Margrethe Sæterdal Bøyum and Maria Helena Seim for a great teamwork with good discussions, comments and support. They have contributed to a social and enjoyable study period. I would also like to thank Christine T. Andersen, Renate Eimind Tveit and Ingvild Blækkan for their contribution in the experimental work.

Last but not least, I would like to thank my family Kjell, Anne Kari, Sandra and Gaute, and my boyfriend Jørgen for being helpful and supportive during my time studying geology at the University of Bergen. Your patience, encouragement and understanding have been highly valued.

Bergen 01.06.2015

Marie Djupevåg Eri

Contents

CHAPTER 1 - INTRODUCTION

1.1 Introduction

Contractional faults have been of interest since they were first mapped and described in the 1800s (Elliott, 1976). Studying the evolution of fold and thrust belts (Fig. 1.1) is vital both for the understanding of orogenesis and for hydrocarbon exploration, as major hydrocarbon accumulations occur in complex structural traps in fold and thrust belts. The tectonic setting and internal characteristics of fold and thrust belts are remarkably varied and diverse. They include classic thin skinned Canadian Rocky mountain style foreland fold and thrust belts (Bally et al., 1966), basement involved Laramide uplift (Schmidt et al., 1993), subduction related thrust systems (e.g. Ramos et al., 2004), collision terrains (e.g. Mugnier et al., 2004) and deep-water gravitationally driven fold and thrust belts (Rowan et al., 2004). Analysis of fold and thrust belts have proven that thrust nappes have been transported up to several hundred kilometres (e.g. Ramberg et al., 2008) and the formation process can take millions of years. A good tool to study this slow and complex development of contractional faults is analogue modelling, which provides a complete record of the formation history.

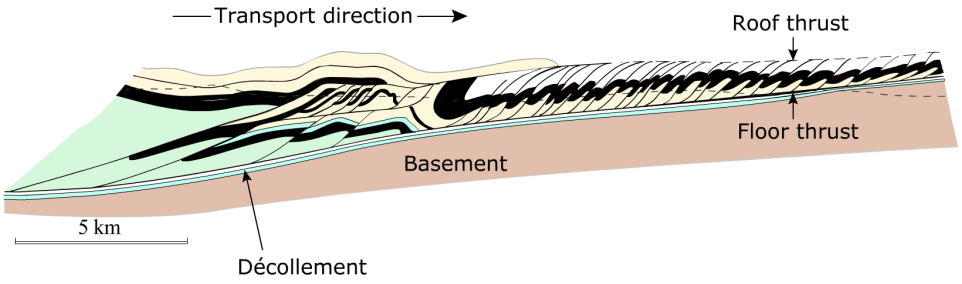

Fig. 1.1: Fold and thrust belt in the south Norwegian Caledonides. From Fossen (2010).

Large-scale faults are well observed and mapped by interpretation of 2D and 3D seismic data. However, minor faults with throw less than 15-20 meters and smaller scale features are difficult to identify since the resolution of seismic images is limited (Fossen, 2010). With information from plaster experiments, it is possible to

study details that cannot be observed on seismic profiles. The deformation history, fault evolution and associated small-scale structures can be studied and results linked to the nature of subsurface structures. These details are important in the hydrocarbon industry because they clarify the complexity of subsurface oil and gas reservoirs. In addition, since almost no geologic event can be thoroughly studied in 3D, either during the formation or after, analogue plaster experiments can provide information of key parameters involved in the structural evolution of contractional settings.

Different techniques and modelling materials have previously been used to construct tectonic environments. The most widely used material is sand which is relative easy to work with (e.g. Hubbert, 1951; McClay and Ellis, 1987). However, sand is not suited for developing the most complex structures and does not preserve the structures after the experiment. Plaster as an experimental material was first used by Cadell (1889) and later by Sales (1987). Plaster has a finer grain size than dry quartz and provides for a much wider range of discernible fault sizes (Mansfield and Cartwright, 2001). In addition, plaster solidifies quickly when mixed with water and results in perfect preservation of the models, which is beneficial when complex structures are to be studied.

The experiments were performed at the Department of Earth Science at the University of Bergen from 2013-2015. Using plaster modelling to study tectonics has previously been performed at the University of Bergen from 1991-2002, some of which are described in Ottesen (1991), Odinsen (1992), Fossen and Gabrielsen (1996), Gabrielsen and Clausen (2001) and Øygaren (2002). The current master thesis is carried out in collaboration with two other students working with strike-slip and extensional regimes.

1.2 Main objectives

The main objective of this project is firstly to create realistic contractional structures by the use of analogue plaster modelling. Second, to use the models to extract information of thrust and wedge characteristics, such as thrust displacement, dip angle, shortening, wedge height etc. (Fig. 1.2). Last, use the information to compare the results with thrust faults found in nature and other experimental work concerning fold and thrust belts.

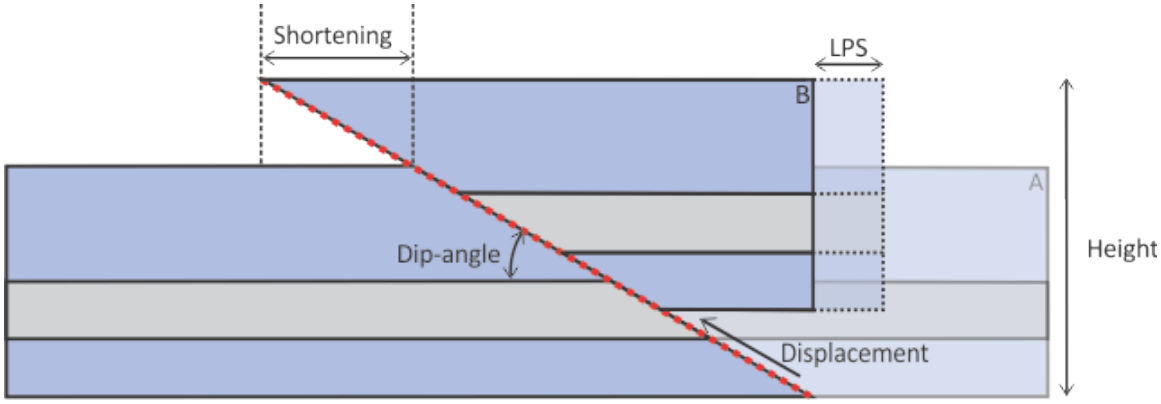

Fig. 1.2: Some factors investigated from the experiments; dip angle, displacement, shortening (both offset on the fault and layer parallel shortening (LPS)) and wedge height. A) Illustrate the plaster prior to contraction, whereas B) illustrates the plaster after initiation of a main fault.

CHAPTER 2 - STRUCTURES IN THE CONTRACTIONAL REGIME

2.1 Introduction

This chapter aims to provide basic geological background theory for the contractional regime, with focus on the type of structures observed in the experiments. Starting with a general outline of ductile and brittle deformation and how faults originate and develop, then focus on the geometry of thrusts and terminology associated with a contractional setting.

2.2 Definition of ductile and brittle deformation

Rocks and minerals react to stress differently and the form of deformation depend on a numerous factors, such as anisotropy, temperature, presence of fluids, strain rate and pressure (Fossen, 2010). Brittle structures such as faults and fractures are most common in the upper part of the crust and will deform by fracturing when subjected to stress beyond the yield point, i.e. the strength of the rock (Burov, 2011). At greater depths, plastic flow will dominate and the transition zone is referred to as the brittle-plastic or brittle-ductile transition zone (Fossen, 2010). A ductile material accumulates permanent strain without macroscopically visible fracturing. Ductile structures such as folds are common in metamorphic rocks of the middle to lower crust and in sedimentary rocks of the upper crust.

2.3 General fault architecture

A fault is defined as a surface or zone where one side has moved relative to the other in a direction parallel to the surface or zone (Twiss and Moores, 1992). Faults grow differently according to what kind of rock they are propagating in (Fossen, 2010). In porous rocks, faults often form by growth of deformation bands (Aydin and Johnson, 1983) whereas in brittle rocks, faults form by interlinkage and growth of shear fractures and joints. Well developed fault zones are commonly described as a fault core surrounded by a damage zone (Fig. 2.1) (Caine et al., 1996). The damage zone consists of joints, minor shear fractures and faults. The centre of the fault is called the fault core. This zone comprises slip surfaces, fault rocks, lenses, shale

smear and fractures (Caine et al., 1996; Chester et al., 1993). Displacement is commonly largest at the fault core and decreases towards its tips (Walsh and Watterson, 1988). Ahead of the fault tip is the process zone where rocks are "processed" prior to fault propagation (Fossen, 2010).

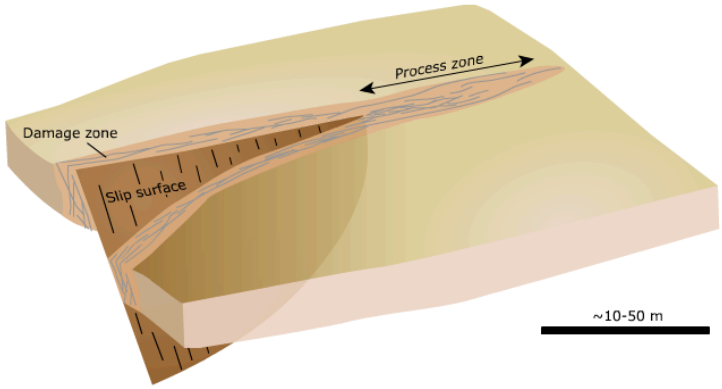

Fig. 2.1: Fault related damage- and process zone. From Fossen (2010).

Related to a fault zone, several secondary faults occur such as synthetic, antithetic (Fig. 2.2) and listric faults. Synthetic faults are minor faults that have the same dip direction as the main fault, whereas antithetic faults are minor faults that have a dip direction opposite of the main fault (Fossen, 2010). Listric faults however, are characterised by decreasing dip with depth (Fossen, 2010).

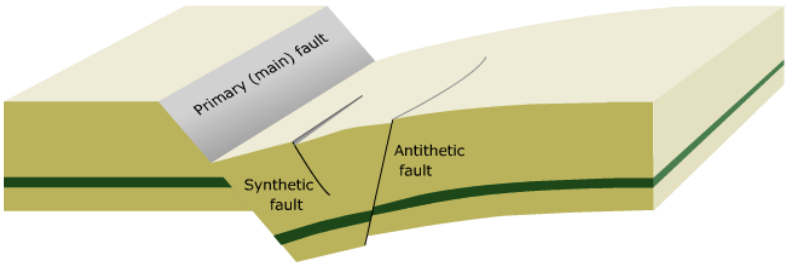

Fig. 2.2: Antithetic and synthetic faults. From Fossen (2010).

Anderson (1905) defined three different fault regimes (Fig. 2.3). The definition was based on the assumption that the Earth is a principal plane of stress containing two of the three stress directions. The third stress direction was oriented normal to the Earth's surface. The fault regimes were divided according to the orientation of the largest (σ_1), intermediate (σ_2) and smallest (σ_3) stress directions;

- Normal-fault regime; σ_2 and σ_3 are horizontal and σ_1 is vertical
- Strike-slip regime; σ_1 and σ_3 are horizontal and σ_2 is vertical
- Revers-fault regime; σ_1 and σ_2 are horizontal and σ_3 is vertical

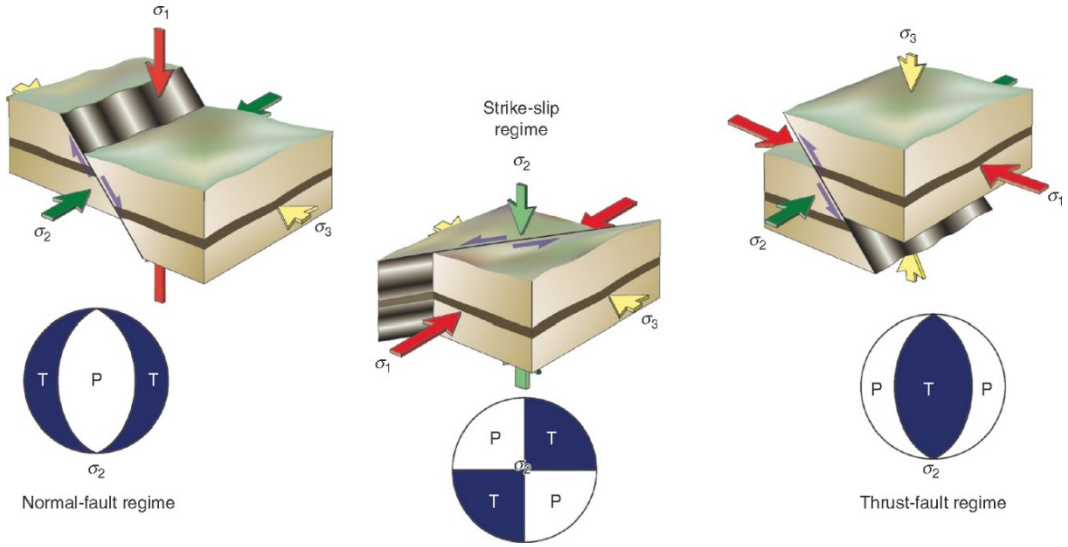

Fig. 2.3: Andersonian stress regimes for normal, strike-slip and thrust faults. From Fossen (2010).

2.4 Contractional faults

When contractional faults are formed, the hanging wall moves up relative to the footwall and a horizontal reference surface is being shortened. The dip slip motion causes older rocks to be brought above younger rocks, producing a repetition of stratigraphic units. If the angle of the fault is steeper than 30° it is called a reverse fault, however if the angle is shallow with a dip of 30° or less it is called a thrust fault (Fig. 2.4) (Fossen, 2010).

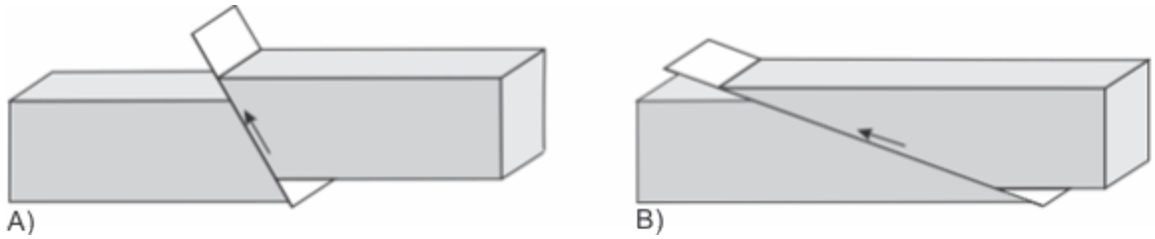

Fig. 2.4: The main types of contractional faults. A) Reverse and B) thrust faults.

Thrust sheets (nappes) stacked on top of each other are collectively called a nappe complex. If a nappe is eroded and only parts is left, the remains are referred to as a "klippe" (Fig. 2.5A), which represents the minimum extent of the original thrust

sheet toward the foreland. If a nappe is eroded and the underlying rocks become exposed, a tectonic window is created (Fig. 2.5B) (Van der Pluijm and Marshak, 2004). Comparing rock units in nappes with underlying, unaffected basement can reveal whether the nappes belonged to the same unit or not. This makes estimations of thrust displacement possible. Rocks located in their original position are referred to as autochthonous units. Allochthonous units lie above the autochthonous and consist of thrust sheets transported away from their original position (Fig. 2.5B) (Dennis et al., 1981).

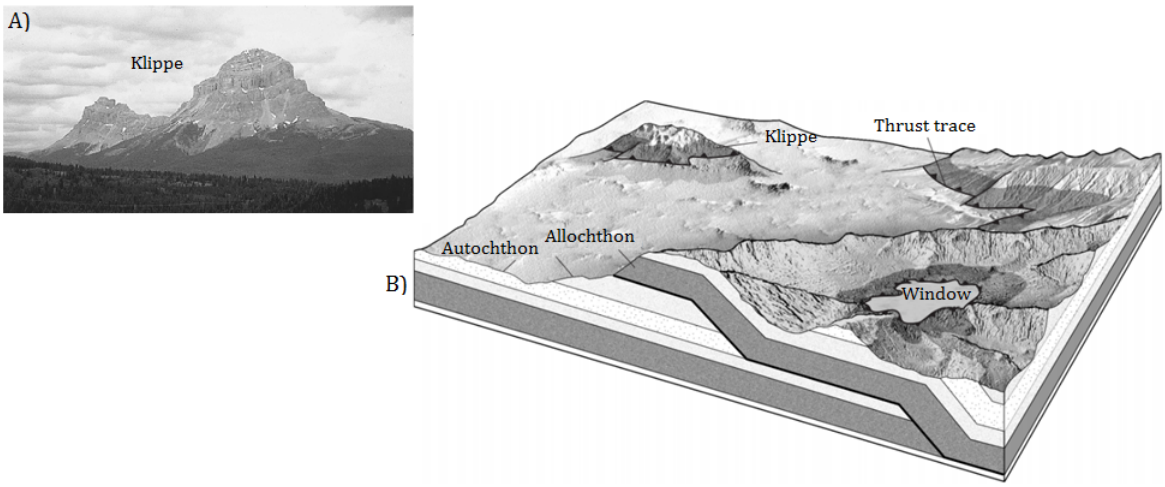

Fig. 2.5: A) Cow's Neste Mountain Klippe, Alberta, Canada. B) Block diagram illustrating klippe, window, allochthonous and autochthonous units. From Van der Pluijm and Marshak (2004).

When referring to the orientations and directions of structures within thrust nappes, the terms hinterland and foreland are widely used (Boyer and Elliott, 1982). Hinterland is where the deformation has caused most damage and is found in the mountainous area of a collision zone. Deformation usually includes both the basement and cover and this is known as thick-skinned deformation. The foreland is the marginal parts of the orogenic belt where there is a lesser degree of deformation and no involvement of basement. This is called thin-skinned deformation (Hatcher, 1995) .

2.5 Contractional fault geometries

2.5.1 Imbrication zone and duplexes

The foreland of orogenic belts is often formed by several similarly oriented reverse faults that are connected through a low angle floor thrust, which collectively are referred to as an imbrication zone. However, if the imbrication zone also bound a roof thrust, the resultant formation is termed a duplex structure (Boyer and Elliott, 1982). The small structures in a duplex are called horses and each is shaped like an "S" in the vertical profile. Stacked horses are called piggy-back thrusts if they are formed by in-sequence thrusting, which means that progressively younger faults form in the footwall of the previous fault and they become increasingly younger towards the foreland (Butler, 1982). However, if a new thrust develop in the hanging wall of an older thrust, it will propagate towards the hinterland and this is called out-of-sequence thrusting (Fig. 2.6) (Butler, 1982).

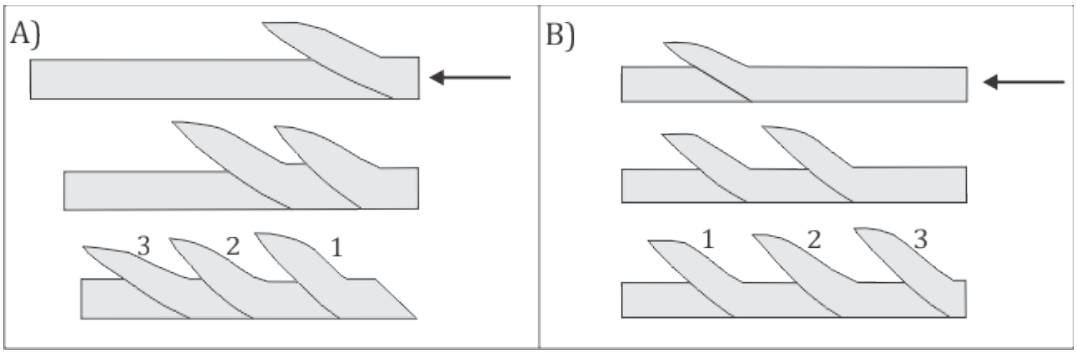

Fig. 2.6: Two possible thrust propagation sequences; A) In-sequence and B) out-of -sequence thrusting. Redrawn from Butler (1982)

2.5.2 Ramps

Two horizontal layers that are found in different stratigraphic levels and are connected through a thrust fault are called a flat-ramp-flat fault. The flat is usually composed of a weak rock layer such as shale or an evaporitic rock layer, then cutting up section in the transport direction to create a ramp, which typically forms in stronger rock units (Twiss and Moores, 1992). There are different types of ramps, which are classified according to their orientation compared to the main transport direction (Poblet and Lisle, 2011). Frontal ramps are placed normal to the thrust

transport direction and are dominated by dip slip movements, lateral ramps are placed parallel to the transport direction and are very steep whilst oblique ramps are placed oblique to the transport direction and are dominated by both dip-slip and strike-slip movements (Fig. 2.7) (Poblet and Lisle, 2011).

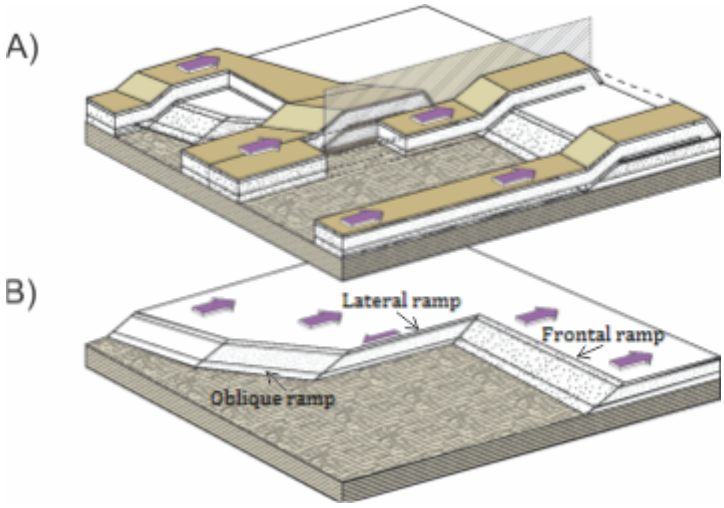

Fig. 2.7: Frontal, lateral and oblique ramps that are found in the contractional regime. The arrows indicate the main transport direction. B) Hanging wall removed. Modified from Fossen (2010).

2.6 Back thrusts

A thrust sheet climbing up a (steep) frontal ramp can result in the formation of a back thrust, which has displacement opposite to the main transport direction (Fossen, 2010). Butler (1982) suggested that layer parallel shortening was accommodated by back thrusts prior to the ramp formation, which resulted in a "pop up" structure. The pop up refers to the part of the structure between the back thrust and the frontal ramp (Fig. 2.8). An alternative model for development of back trusts was presented by Mandl and Crans (1981). Mandl and Crans (1981) suggested that the back thrust was formed after the ramp formation in associated with rotation of the hanging wall during frontal ramp climb (Fig. 2.9).

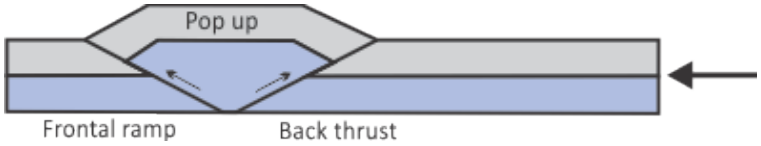

Fig. 2.8: Pop up structure. Redrawn from Butler (1982)

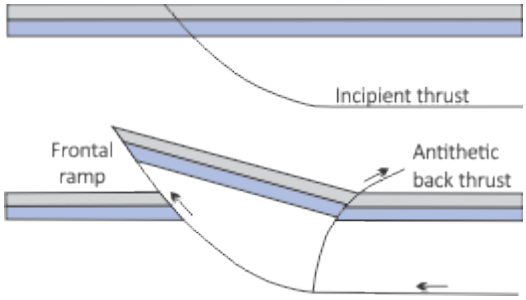

Fig. 2.9: Antithetic back thrust. Redrawn from Butler (1982).

2.7 Fault related folds

According to Brandes and Tanner (2014), folds related to faulting are a result of changes in fault parameters are divided into three categories; detachment folds, fault-bend folds and fault-propagation folds. Detachment folds are created if two layers above each other with different strength experience shortening (Fig. 2.10B). Folding will happen in the strongest layer, whilst the weakest layer, often a detachment layer, will remain unfolded. A fault-bend fold is formed when a fault starts to climb over a ramp (Fig. 2.10C). The geometry of the fold will reflect the geometry of the underlying ramp. Angular ramps will make angular folds and gently curved ramps make a smoother, less angular fold (Fossen, 2010). Fault-propagation folds are formed if slip decrease along the faults length, and results in asymmetric folds that develop in front of the fault (Fig. 2.10D). In association with fault-propagation folds, a triangular shear zone of deformation (Fig. 2.11) focused on the tip of the propagating fault can be formed if the material in the footwall is fixed while the material in the hanging wall is moving with a constant velocity (Erslev, 1991).

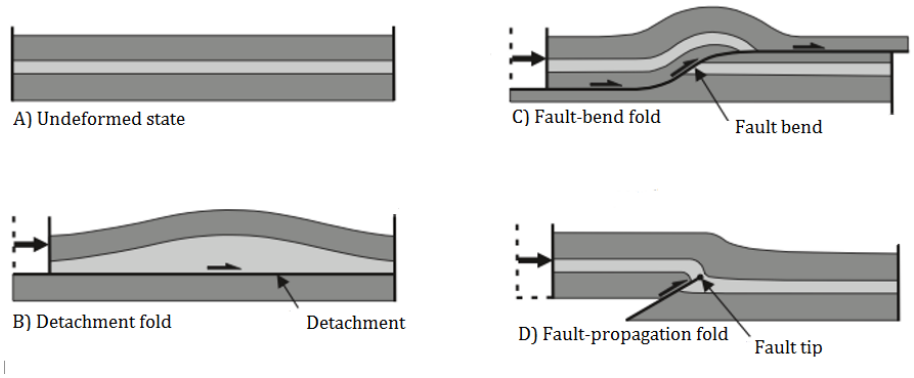

Fig. 2.10: Folds in association with faults. From Brandes and Tanner (2014).

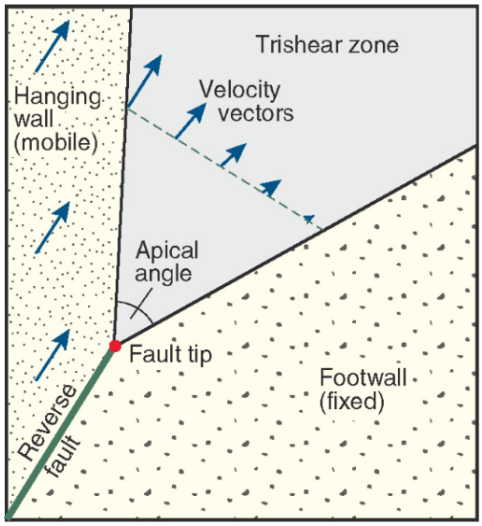

Fig. 2.11: Trishear zone at the tip of a propagating fault. From Fossen (2010).

2.8 Critical taper theory

Several geologists have since the early 1980s considered the evolution of thin-skinned fold and thrust belts to be analogous to wedges of snow in front of a moving bulldozer (Fig. 2.12) (e.g. Davis et al., 1983). The material in front will deform until reaching a critical taper and the characteristic stable wedge shape is achieved when the wedge is everywhere at the critical angle and at the verge of failure. The critical taper is the opening angle between the surface slope and the basal décollement, and its magnitude is dependent on the frictional and pore fluid pressure within the wedge and along the basal décollement (Buiter, 2012). The stress within the wedge must be critical at every point, i.e. have the same strength as the material being deformed. If the stress gets higher, material will instantly deform until equilibrium

is regained (Fossen, 2010). The wedge will slide without any internal deformation and become stable when no new material is added (Buiter, 2012). The critical taper theory is useful to explain the overall geometry of wedges and the shape of a wedge depends on basal friction, the strength of the wedge material and erosion. A strong wedge with high basal friction will form higher wedge with a steeper slope.

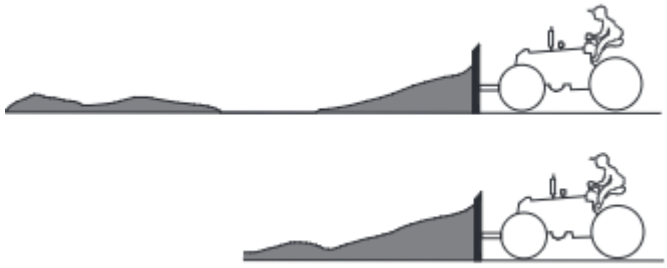

Fig. 2.12: The top illustration show a stable snow wedge prior to an accretion event. The bottom illustration shows ongoing accreting snow wedge, trying to reach critical taper. From Buiter (2012).

CHAPTER 3 - DESCRIPTION OF ANALOGUE MODEL EXPERIMENTS AND BALANCING CROSS-SECTIONS

3.1 Introduction

Different kinds of models have been used for a long time to support geological structures observed in the field and theories have been applied to check if the models can be geometrically accepted. Modelling is a good method to get a better understanding of how structures evolve in time and space. Different materials have been used to simulate tectonic developments. This short summary presents pioneering experimental work and important experiments performed over the last 60 years. Lastly, scaling issues with modelling and historical background for balancing cross sections are presented.

3.2 Pioneering experimental work

Tectonic processes involving formation of fold and thrust belts have been of interest for a long time and experimental modelling have been performed since the beginning of the 19th century (Graveleau et al., 2012). Earliest documentation of experiments to explain geological processes was the work performed by Hall (1815) (Graveleau et al., 2012). Hall (1815) wanted to explain the evolution of folds he observed in geological strata along the east coast of Scotland. To do this, he stacked layers of cloth between two wooden boards and compressed the cloth horizontally while a load confined the cloth vertically (Graveleau et al., 2012). This resulted in the formation of folds (Fig. 3.1A). Another experiment performed by Hall is similar to modern fold and thrust belt experiments, in which he used clay in a box that had two adjustable sides and the clay was confined vertically by the use of screw jacks. This experiment resulted in the generation of folds similar to those observed in the field (Fig. 3.1B). Hall concluded that there must be similar mechanisms producing the folds in the experiments and the folds he observed in the field, and that folds must be a result of horizontal compression in the crust (Graveleau et al., 2012).

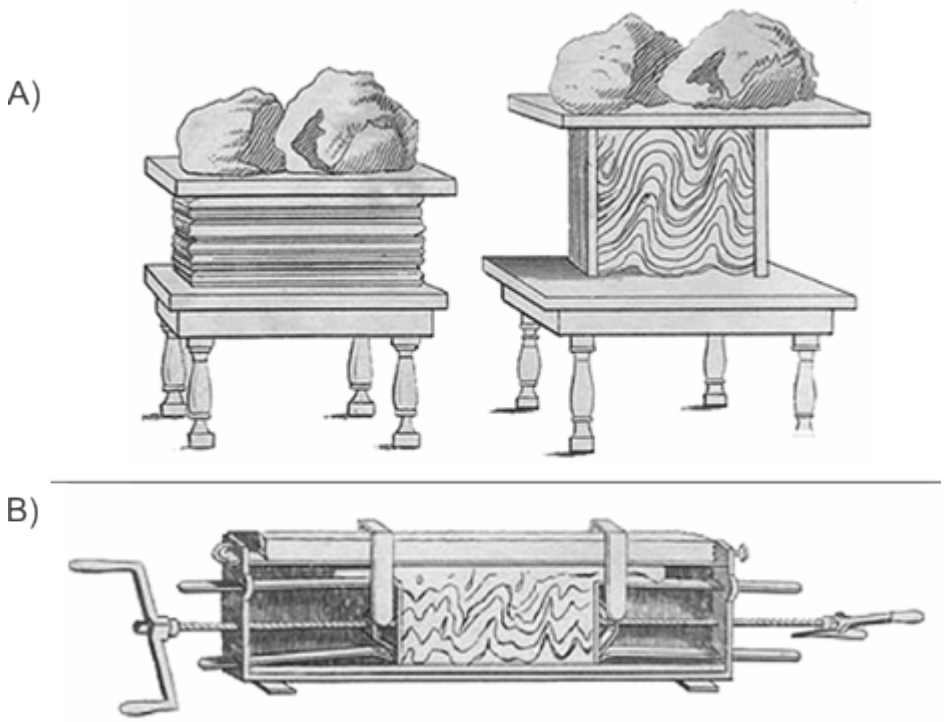

Fig. 3.1: Experiments performed by Hall (1815) to investigate fold development. A) Stacked layers of cloth between two wooden boards compressed horizontally while a load confined the cloth vertically. B) Clay confined vertically by the use of screw jacks in a box with two adjustable sides. From Graveleau et al. (2012).

Decades after Hall had presented his work, new geologists tried to improve his methods with new set ups and techniques. Cadell (1889) explained mechanisms behind thrusting in layered rocks. His experiments consisted of compressing brittle materials like sand, clay and plaster of Paris in a "squeeze box" (Fig. 3.2). He obtained good results and created structures similar to the ones observed in the field. Cadell (1889) concluded that thrust structures are a result of horizontal forces and that thrust planes have a dip towards the side from which force was applied.

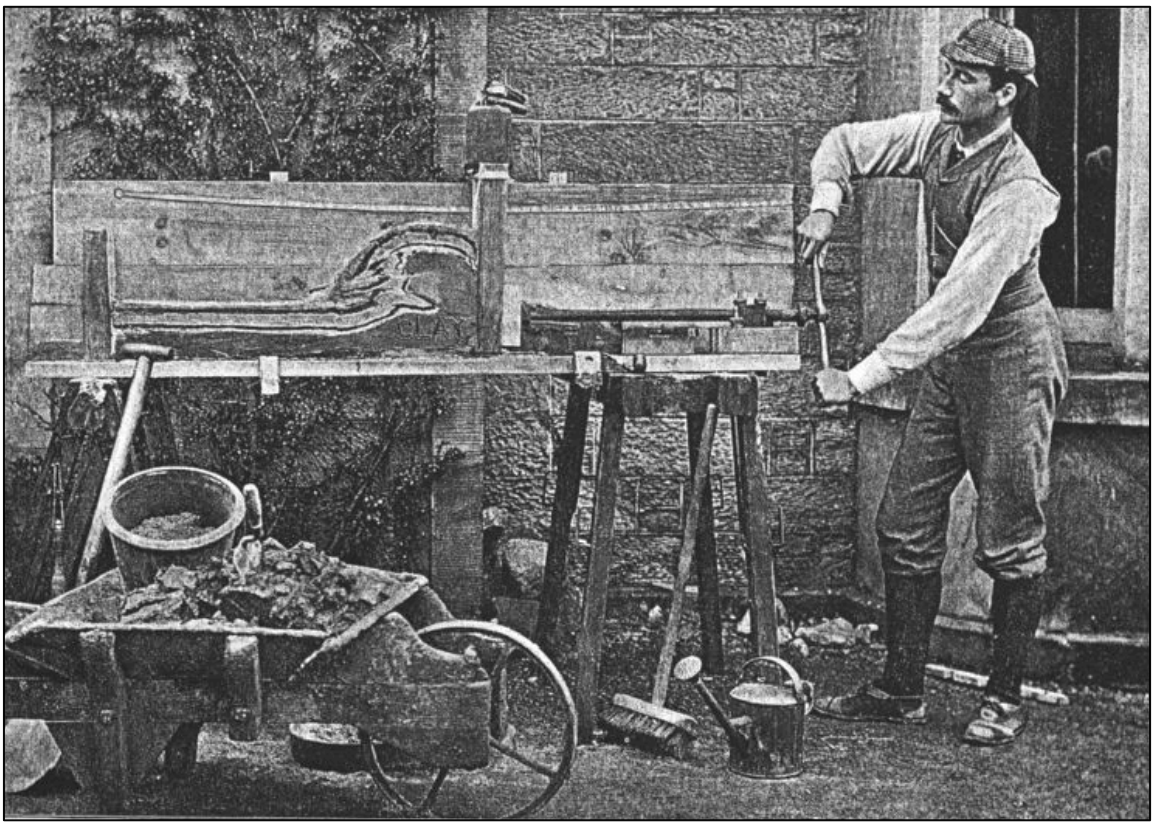

Fig. 3.2: Cadell´s experimental "squeeze box". Thrust structures are formed and the thrust planes have a dip towards the side from which force was applied. From Cadell (1889).

3.3 Modern experimental modelling

The pioneering work done in the 1800´s became an inspiration for modern day geologists that want to study tectonic processes. In the 20th century, a range of geological structures have been investigated using analogue models. Modelling have been done with both strike-slip (e.g. Wilcox et al., 1973), extension (e.g. McClay, 1990) and compression (e.g. Koyi, 1995). The models have valuable information as they present faults progressing in time on a miniature scale that is easy to study. Parameters in the experiments are varied in order to get a better understanding of what will affect the formation of faulting and other geological structures. The parameters that are most often varied are properties of the basal décollement, the material used, the fluxes, the backstop, kinematics and surface processes (Graveleau et al., 2012). The materials wax and honey have been used to illustrate

ductile/plastic properties (Steyrer, 2009). Sand, gypsum and clay have been used to illustrate brittle properties and will be discussed further.

3.3.1 Analogue sandbox model

One of the most common used models to explain plate tectonics is the sandbox model. Processes on Earth that take millions of years can be simulated in just a few hours in a laboratory under controlled conditions (Steyrer, 2009). Dry cohesionless material like sand is found to develop the same deformation mechanisms and structures found in natural conditions, because sand has an angle of internal friction of 30-32°, which is similar to that determined for brittle sedimentary rocks in the upper continental crust (Graveleau et al., 2012).

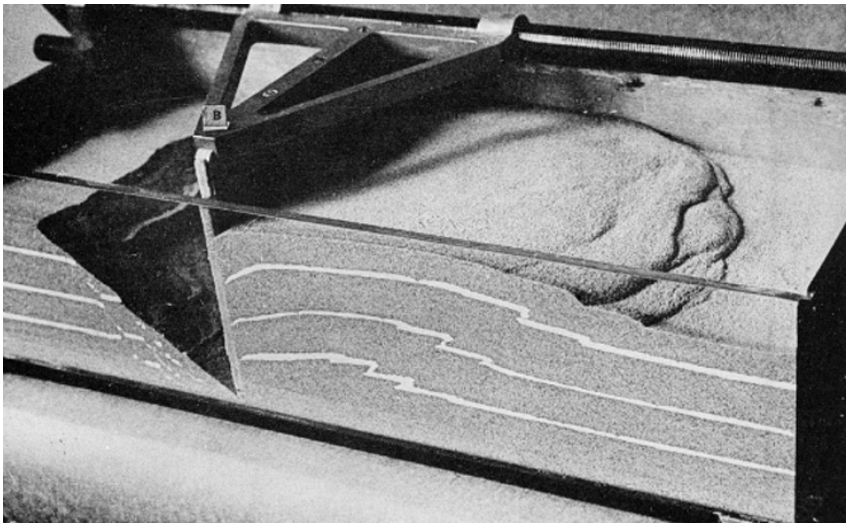

Fig. 3.3: Hubbert's devise used to show the development of normal and thrust fault. From Hubbert (1951).

One of the first scientists that explored the sandbox model and scaling was Hubbert (1951). Hubbert used a box with glass walls filled with loose, dry sand and had powdered plaster of Paris as maker layers (Fig. 3.3). The experiment was set up so that both extensional and compressive environment could be studied together. Many people have followed Hubbert's lead in doing sandbox experiments. Yamada et al. (2006) pulled a plastic sheet underneath dry quartz sand and dry microbeads (Fig. 3.4A). The microbeads were inserted between the sand layers to act as a décollement layer with lower friction. The result was a foreland vergent piggy-back

sequence created in the sand layer above the microbeads. The sand layer below the microbeads was not affected by the deformation (Fig. 3.4B). Compared with an experiment without microbeads (no décollement layer) it was found that the spacing between the faults increased and the slope angle was reduced.

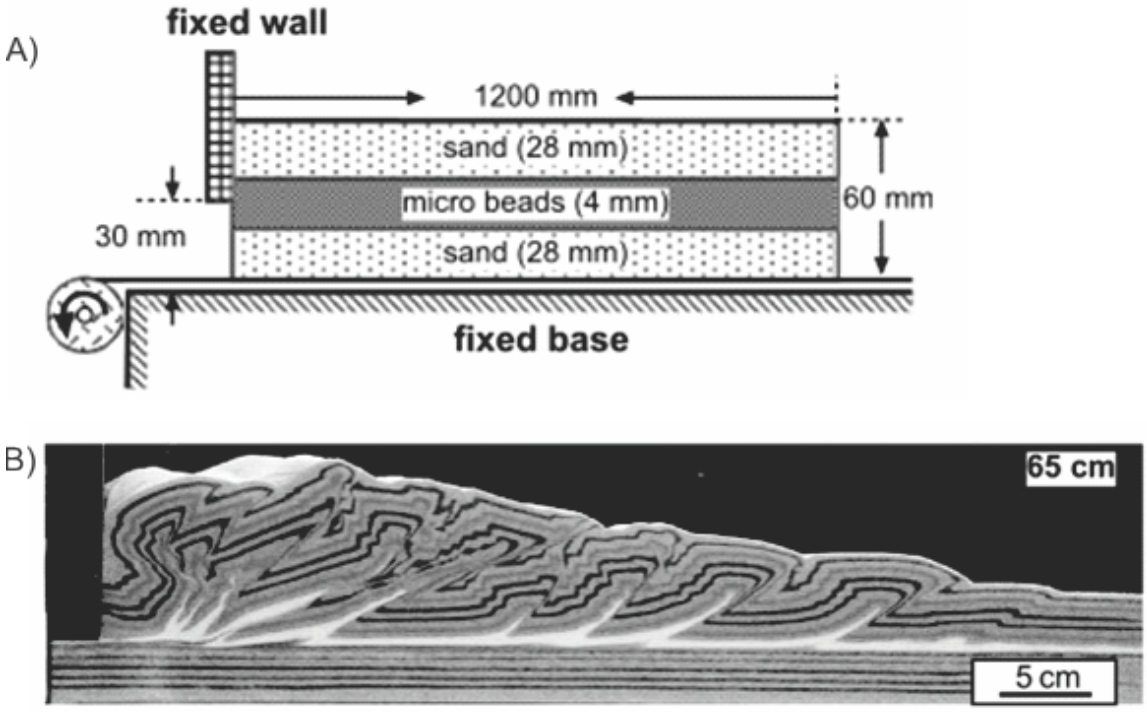

Fig. 3.4: Experiment performed by Yamada et al. (2006). A) Set up for sandbox experiment with a layer of microbeads to act as a horizontal décollement. B) Result of the sandbox experiment. Only layers above the décollement are being faulted. The drag of an underlying sheet creates a piggy-back thrusting sequence.

3.3.2 Analogue clay models

The first scientist that used clay in his experiment was Cloos (1955). Cloos (1955) chose to work with clay because he could change its physical properties by adding water. The material was also cheap and easy to obtain. Cloos (1955) investigated the fracture patterns found in rocks. In one of his experiment (Fig. 3.5) he placed a 40-50 cm clay square with a smooth surface on a movable square of wire that he pulled diagonally in two opposite corners. On the clay he drew circles so he could see how the circles changed shape during the experiment and thus see the degree of deformation that developed. If water was sprinkled on the clay, tension fractures

formed perpendicular to the pull. However, if no water was added, the circle would be more deformed before any fractures appeared, this time as shear fractures. As deformation continued, fractures would rotate and become more evident. At the end of the experiment, the circle had turned into an ellipse and been faulted (Cloos, 1955).

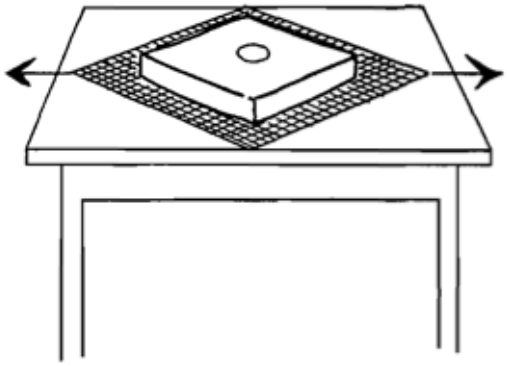

Fig. 3.5: Experimental set up by Cloos (1955). Clay square on top of a movable wire grid. The circle is drawn in the clay as a reference to the degree of deformation. From Cloos (1955).

Cloos could change his experiment so that other geological features would form. For instance, if he placed the clay cake above a rubber base and extended the rubber, the clay would form a fault system with small and high angled faults. Cloos did the same experiment but replaced the rubber with two tin plates. This created larger, but fewer faults that experienced a higher degree of rotation and had a more gentle dip. By constantly changing his experiment, he managed to produce several other geological features like domes, folds, grabens and joints.

3.3.3 Previous work with plaster

Previous works with plaster experiments are not too extensive, although some have been performed and documented. Sales (1987) used plaster to simulate both the strike-slip, contractional and extensional regime. In the contractional experiment, he deformed the plaster by pushing a piston inward in an experimental box and observed faults formed in an in-sequence fashion and dipping toward the piston. Most plaster experiments are studies of the extensional regime (e.g. Fossen and

Gabrielsen, 1996; Gabrielsen and Clausen, 2001; Mansfield and Cartwright, 2000). Extensional plaster experiments reviled that major through cutting faults accommodate about 60-70% of the total deformation, while smaller faults accommodated 10-20% and ductile deformation accommodated 20-30% of the total deformation (Fossen and Gabrielsen, 1996).

3.4 Scaling

Models of brittle compressional wedges usually attempt to simulate kilometre thick and tens of kilometres wide upper crustal/sedimentary structures (Buiter, 2012). Analogue models must therefore be scaled from cm scale in the lab, to km scale in nature. The most widely known work considering scaling was performed by Hubbert (1937). Hubberts scaling approach has also been the base for later work with small-scale geological structures (e.g. Ramberg, 1981).

Two bodies (an original and its model) of any shape are said to be geometrically alike when all corresponding lengths are proportional and all corresponding angles are equal. Kinematic similarity is when two geometrically similar bodies undergo the same geometric changes of shape and/or position, provided that the time required for the changes is proportional in the two bodies. Dynamic similarity however, is when two bodies are both geometrically and kinematically alike and the mass ratio between the two bodies is the same. Hubbert (1937) found that small bodies are stronger than large bodies of the same material, and that the larger the body, the greater its weakness. This means that both the strength and the size of the body need to be considered when scaling, because generally the strength of a body decrease with increasing size.

According to Fossen and Gabrielsen (1996), scaling different modelling materials (e.g. sand, plaster etc.) can be challenging. Dry sand for instance, has no cohesive strength, a parameter that is neglected in most experiments as natural rocks have cohesive strength. On the other hand, plaster exhibits a cohesive strength, but this strength becomes too high when scaled to natural size. In addition, when scaling sand and plaster grain sizes, the grains become too large and unrealistic.

3.5 Balancing cross sections

An important part of the experimental modelling is to check if the models can be geometrically accepted, which means that they must be able to be reconstructed back to the shape they had prior to the deformation. A cross section is said to be balanced when it is admissible, meaning that the section contains geologically reasonable structures both in respect to each other and the tectonic setting, and retro-deformable meaning it is possible to undo the deformation, moving rocks back to their initial, pre-deformable configuration (Fossen, 2010). It is important to remember that a balanced cross-section is not necessarily a correct interpretation of the deformation.

Geologists have used balancing of cross sections for decades to test their interpretation. The first who introduced the term "balanced" in geology and managed to quantitatively predict the shape and position of a basal detachment was Chamberlain in 1910 (Wiltschko and Groshong, 2012). By presuming that the area above a sole thrust was the same before and after deformation, he found the depth of the sole thrust in the zone of contraction (Fig. 3.6). Later, the contraction percent for several fold and thrust belts are found by the use of balancing cross sections; 35-43% contraction for the Appalachians (Gwinn, 1970; Dennison and Woodward, 1963), 54% contraction for the Alberta thrust belt (Price and Mountjoy, 1970) and 43% contraction for the Etnedal nappes (Hossack, 1979). Thin-skinned fold and thrust belts are well suited for balancing since the deformation usually occurs in the upper crust. The deformation mechanism in the upper crust is mostly brittle and folds formed are usually concentric or kink-band folds, with little ductile flow of material from the limb to the hinges.

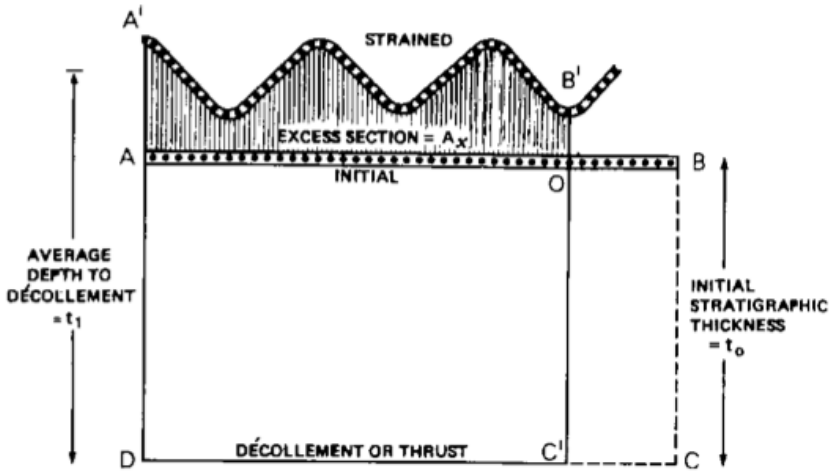

Fig. 3.6: The method of balancing a cross section presented by Chamberlain (Hossack, 1979). Equal area calculation. The bed AB at original height of BC is folded into a new position A´B´, AB=l_0, AO=l_1, OB= shortening. ABCD=A´B´C´D. Therefore AA´B´O=OBCC´ (excess section A_x). Shortening OB=A_x/t_0. Within the shortened area, faulting and/or folding may affect the rocks.

CHAPTER 4 - EXPERIMENTAL PROCEDURE AND METHODS

4.1 Introduction

This chapter explains the rheological properties of plaster of Paris and the advantages and limitations associated with using plaster as a modelling material. A review of the experimental set up, as well as documentation method is also presented. Lastly, restoration method is explained.

4.2 Properties of plaster of Paris

The type of plaster used in the experiments is called plaster of Paris, which is a pure (minimum 91% gypsum), white powder with 97% of the grains at 100 μm, and the remaining 3% at 200μm (Saint-gobain, 2015). Plaster of Paris is made when gypsum is heated up to high temperatures to create calcium sulphate (Vekinis et al., 1993), then grinded to a fine white powder. When the powder is mixed with water, the mixture gradually solidifies at a rate depending on the water/plaster ratio. The physical property of plaster is determined by amount of water added and length of the solidification period. High water/plaster ratio and short solidification period leads to softer plaster. On the contrary, high amount of plaster with long solidification period leads to more firm plaster. The ability of the plaster to resist deformation, i.e. the strength of the plaster, increase with increasing firmness of the material.

The plaster is pored into the glass box when still liquid and weaker than the structure tried to simulate. The deformation starts first when the plaster has a strength assumed to be proportional to the strength of the natural structure. The right consistency is found by dipping a nail into the plaster. If the nail gets a collar of plaster around the nail head, the plaster has the right consistency and the deformation can start. With some experience and knowledge about the plaster, the experiment can be controlled and began with plaster that has approximately the same strength each time. It is important not to start the deformation process before the plaster has the right viscosity. Too wet plaster results in viscous flow of the

plaster rather than clear faults. On the contrary, too stiff plaster results in open fractures or immobility of the moving wall.

4.3 Advantages and limitations with plaster experiments

The advantages of plaster experiments in general are the simplicity of the model setup, formation of detailed structures and preservation of end results. The fault evolution can be followed from start to finish from two cross-sections in addition to the top. The plaster dries fast and is preserved perfectly after solidification. After the experiments, the models can be kept for detailed study of the structures and future reference. Plaster of Paris is especially good to work with compared to other materials (e.g. sand and clay) because of its fine grains and massive consistency, which creates small structures which can be seen both during deformation and at the end result.

When performing plaster experiments, some complications may arise, as with any other modelling material. During the experiment, one of the wooden sides was moved by hand, which created an uneven strain rate that needs to be considered during analysis. From the moment the plaster is mixed with water, a solidification process starts. The plaster is therefore constantly changing physical properties throughout the experiment, becoming more and more viscous. Plaster also release water that accumulates at the top of the constant solidifying plaster, making it hard to know when the plaster has a perfect consistency for modelling. Also, internal reference layering has proved to be difficult to achieve. In this study, paint has proved to be a good option for reference layering, however only present at the sides of the models. Painting the reference layers is done by hand which makes it difficult to make straight, horizontal lines.

4.4 The experimental set up

The modelling setup for this experiment is described in both Sales (1987) and Fossen and Gabrielsen (1996). The same set up has been used in current experiments, although a few alterations have been made along the way. Two boxes have been designed. They are very similar, only the width was different. Both boxes were made of two fixed glass walls (100x30cm) at the long sides and two wooden walls (9x50x5 and 14x50x5) at the short sides (Fig. 4.1). One of the wooden walls was fixed, while the other was movable. The edges of the wooden walls were covered with strips of rubber to reduce friction with the glass and to reduce leakage of the plaster. The base of the box consisted of a wooden plank, on which there were smeared wet barite mixed with food colouring to be able to differentiate between the plaster and the barite. The barite had varying thickness (approximately 0.2-4 cm) for each experiment and represented the basement in addition to seal for the cracks in the box. Barite is white in colour and very fine grained. When mixed with water, barite gets the consistency of soft butter. The glass walls were covered with canola oil to reduce friction along the sides. After placing the plaster in the box and before solidifying, the glass was marked with 1-3 stripes of blue paint that acted as reference layers, which makes it easier to trace the deformation. Lighting was important to get good quality photos. There were installed two bright lamps on the wall, in addition to the use of two handheld lamps during the experiments. When the plaster has the consistency of thick cream, the movable wooden wall was moved towards the stable wooden wall. Plaster represents the sedimentary cover above the basement. Constant plaster content and the ability to follow the marker layers throughout the experiment are important to get a realistic end result and to simplify the analysing process.

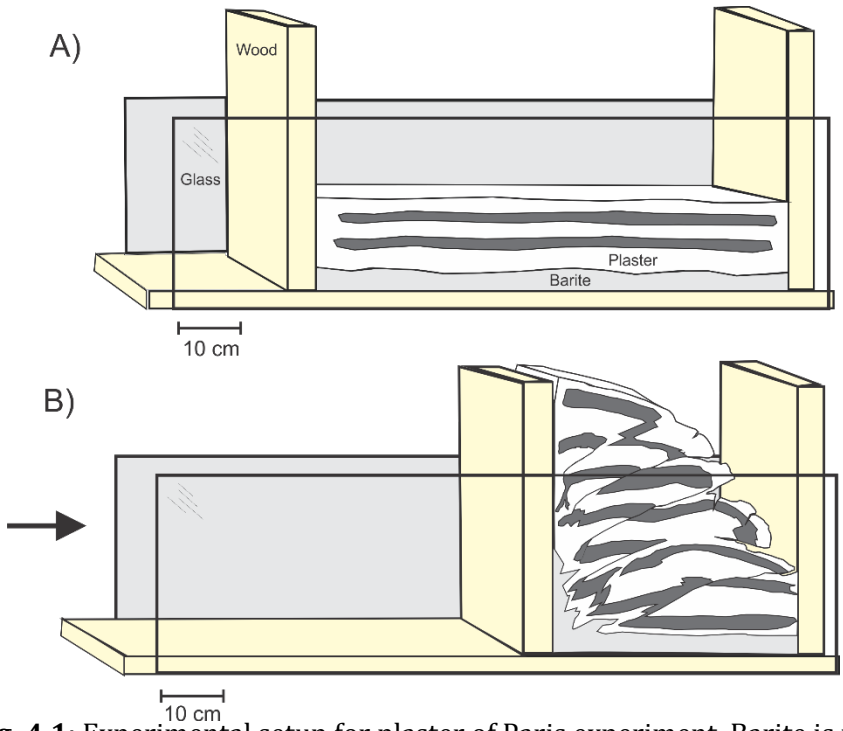

Fig. 4.1: Experimental setup for plaster of Paris experiment. Barite is used as basement. The width of the vertical wooden plates vary (9x50x5 and 14x50x5 cm). A) The undeformed plaster prior to contraction B) After contraction.

4.5 Documentation of the experiments

The experiments were documented with two cameras placed on each long side of the experimental box and one hanging from the ceiling directly above the experimental box. The cameras are controlled manually with the use of remote shutter releases for each camera to simplify the photography. There are taken 4 photos each second. A high resolution Nikon D800 each with AF-S Nikkor 50mm f/1.4G lens is used with a resolution of 7360 x 4912 pixels. Close-ups were taken after the experiments and small and large structures are documented. In addition, photos are put together to create videos of the experiments. This way, the entire experiment can be viewed numerous times when analysed.

4.6 Restoration

The plaster experiment 12-14 is described through six steps in chapter 5 (see subchapter 5.2 for step-by-step development and figures). Three intermediate steps

at 15%, 34% and 50% are chosen for restoration to analyse the evolution of deformation through the shortening. The starting model is used as a reference. In the plaster models, a thick, painted stripe represents the reference layers. However, a thin horizontal line will represent these stripes in the restoration and they are traced to connect the same points as the painted reference layers. During restoration, the curved lines were sheared part by part to their horizontal state and moved to connect the other reference layers, making a horizontal line (see principal illustration of restoring, Fig. 4.2). Measuring the segment length of each deformed layer and adding them together, found the effects of imbrications. By comparing this restored length with the undeformed length of the model, it was possible to calculate and find the amount of shortening accommodated by layer parallel shortening (Koyi et al., 2004). Worth mentioning is that the restoration is not completely accurate as it is conducted in Adobe Illustrator. To get a more accurate restoration, more time consuming and complicated programs should be used (e.g. 2D move).

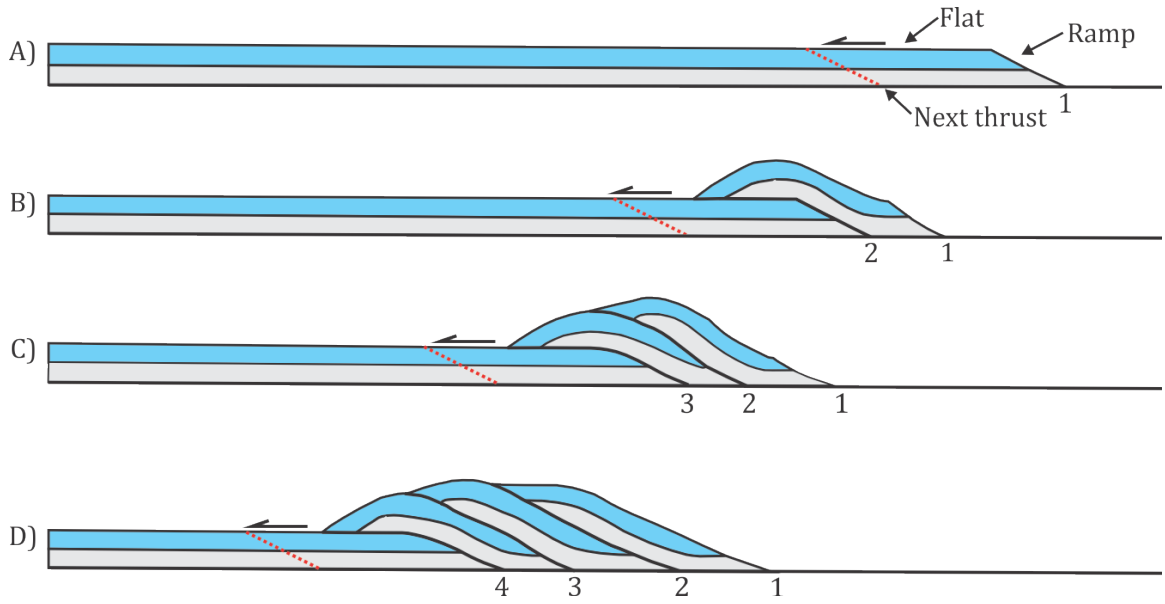

Fig. 4.2: Principal sketch of a how to balance and restore cross sections, here for a hypothetical hinterland-dipping duplex. Numbers 1 (oldest)-4 (youngest) indicates when in the faults are formed. Redrawn from Butler (1987).

CHAPTER 5 – DESCRIPTION OF THE EXPERIMENTS

5.1 Introduction

The aim of this chapter is to give the reader a detailed description of the plaster deformation throughout the experiments. Six experiments are chosen on the basis of good photo documentation, no leakage of plaster and interesting structure developments, and the experiments are presented in the order they were performed. Both sides of the experimental box are presented with a summary following each experiment and a figure showing active periods for the individual faults. Step-by-step figures and pictures of the final models are attached to give a better illustration of the deformation process. The step-by-step figures are chosen on basis of structural development rather than specific time slices. This is apparent as structural development happens at different compression percentages in each individual experiment. Videos of the six experiments are attached in Appendix A.

The experiments are described by percent of shortening for each step studied, using the ratio $R = [L_1/L_0] \times 100$, where (l_1) is the amount of shortening (in cm) and (l_0) is the initial length (in cm). For each experiment, the initial and final length (in cm), as well as the initial and final height (in cm) are stated. The height is measured from the highest point in the model. The first main fault is presented as F_1 and is assigned a letter (A/B), which differentiates sides of the model. The second main fault is presented as F_2 and so on. Active faults on each step are marked with red colour.

5.2 Experiment 12-14

The stepwise development of deformation through the experiment can be followed in figure 5.1 and 5.2.

Table 5.1: Experimental data for experiment 12-14.

Date	29.01.14
Plaster/water ratio	4.5 L plaster / 4 L water
Experimental conditions	4 cm horizontal barite basement
Experimental box	Wide (14 cm width)
Start length	64 cm
End length	32 cm
Start height	10 cm
End height	25 cm
Note	Water percolated through the plaster, leaving a film of water on the surface

Step 2 – 2% contraction

Side A (Fig. 5.1-2): F_1A is initiated in the lowermost reference layer after 1,5% contraction and has propagated to the top after 2% contraction. At this stage, the fault has a dip of 38° towards the moving wall and displacement of 0.5 cm in the lower reference layer, which decrease with a few mm as the fault approaches the surface.

Side B (Fig. 5.2-2): F_1B has the same initiation characteristics as F_1A and formed after 3% shortening. Both F_1A and F_1B developed from the barite/plaster boundary. However, the dip of F_1B is 40° towards the moving wall and the displacement is 0.2 cm, which also on this side decrease with a few mm as the fault approaches the surface.

Step 3 – 14% contraction

Side A (Fig. 5.1-3)**:** F_1A has climbed up the underlying ramp and has a dip of approximately 39° towards the moving wall. Maximum displacement of 5 cm is found close to the plaster/barite boundary. The fault tip of F_1A is bending down as the fault passes the ramp, creating several small vertical cracks at the surface from the extension. After this stage, F_1A is not developing any more displacement and is therefore said to be inactive. A second main fault, F_2A, formed further towards the stable wall close to the barite/plaster boundary after 8% contraction. At this point, the fault has developed a displacement of 3 cm and a dip of 33° towards the moving wall.

Side B (Fig. 5.2-3)**:** F_1B is at this stage inactive. The fault developed a displacement of 8 cm and a dip of approximately 47° towards the moving wall, which indicate that side A and B are very similar. The top of F_1B has a more gentle dip than the rest of the fault since the fault tip is bending as the passes the ramp. A second main fault, F_2B, was initiated after 9% contraction, and is at this stage well established with a dip of 38°. As before, the fault is first initiated in the lower part of the plaster, then propagating upwards to the top of the model.

Step 4 – 25% contraction

Side A (Fig. 5.1-4)**:** F_2A has propagated upwards and developed a maximum displacement of 8 cm and a dip of approximately 39°. The tip of F_2A bends down towards the foreland as the fault passed the ramp. F_2A is at this stage inactive. The third main fault, F_3A, was initiated close to the barite/plaster boundary at 20% contraction and has at this point a 3 cm displacement and cuts through both reference layers with a 34° dip. Two small, almost vertical faults with approximately 1 cm displacement develops in the lower reference layer in the third fault block, but do not become larger as the deformation continues.

Side B (Fig. 5.2-4)**:** The displacement and dip angle of F_2B is similar to F_2A. The tip of F_2B has bended and extended so much that it is nearly broken off. This forms a large vertical crack at the top of the thrust. F_2B is at this point no longer active. Small reverse faults with a few mm displacements have developed in the lowermost

reference layer close to the moving wall. In addition, also close to the moving wall, a back thrust with 1 cm displacement is formed. None of these structures develop further as the contraction continues. The third main fault, F_3B, was initiated at 19% contraction close to the barite/plaster boundary and has at this stage a displacement of 3.5 cm. A back thrust with a displacement of 0.3 cm and a dip of 68° is formed between F_2B and F_3B in the lower reference layer.

Step 5 - 34 % contraction

Side A (Fig. 5.1-5): The dip angles of F_1A and F_2A have increased as subsequent faults developed at the toe of the wedge. The tip of F_2A has been bended and extended so much that it breaks off. At the same time, a large vertical crack surrounded by several small vertical cracks developed at the tip of F_3A. As the third thrust sheet is climbing over the ramp, a lens structure is formed between the hanging wall and the footwall. The lens structure lens is dragged towards the stable wall (or foreland) as the shortening proceeds. A fourth major fault, F_4A, is formed in the plaster/barite boundary close to the stable wall.

Side B (Fig. 5.2-5): F_3B has developed a displacement of 13.5 cm and a dip of 30°. The fault tip of F_3B breaks off and is smeared underneath the hanging wall as the fault propagates forward. The back thrust described at 25% contraction has developed further, now with a displacement of 1 cm. Two small reverse faults are formed close to the stable wall shortly after 34% contraction.

Step 6 - 50% contraction

Side A (Fig. 5.1-6): F_3A has developed a displacement of 16 cm and is at this stage no longer active. The large vertical crack developed in F_3A after 34% contraction has developed further and is at this stage cutting through the entire top reference layer. F_4A has developed a steep angle of 47° as the fault approaches the stable wall. Two back thrusts with a dip towards the stable wall have been formed in the fourth fault block. The back thrusts have a displacement of approximately 0.6 cm and a dip of 42°. At the end of shortening, F_4A has a displacement of 4 cm.

Side B (Fig. 5.2-6): After 50% contraction, one of the small reverse faults formed close to the stable wall has developed further and formed the fourth main fault, F_4B. F_4B has a steep dip of 49° towards the moving wall and a maximum displacement of 2.5 cm in the lowermost reference layer. In the hanging wall of F_4B, a back thrust was initiated after 43% contraction in the lower reference layer and formed a popup structure. The back thrust has a displacement of 1.5 cm at the end of the experiment.

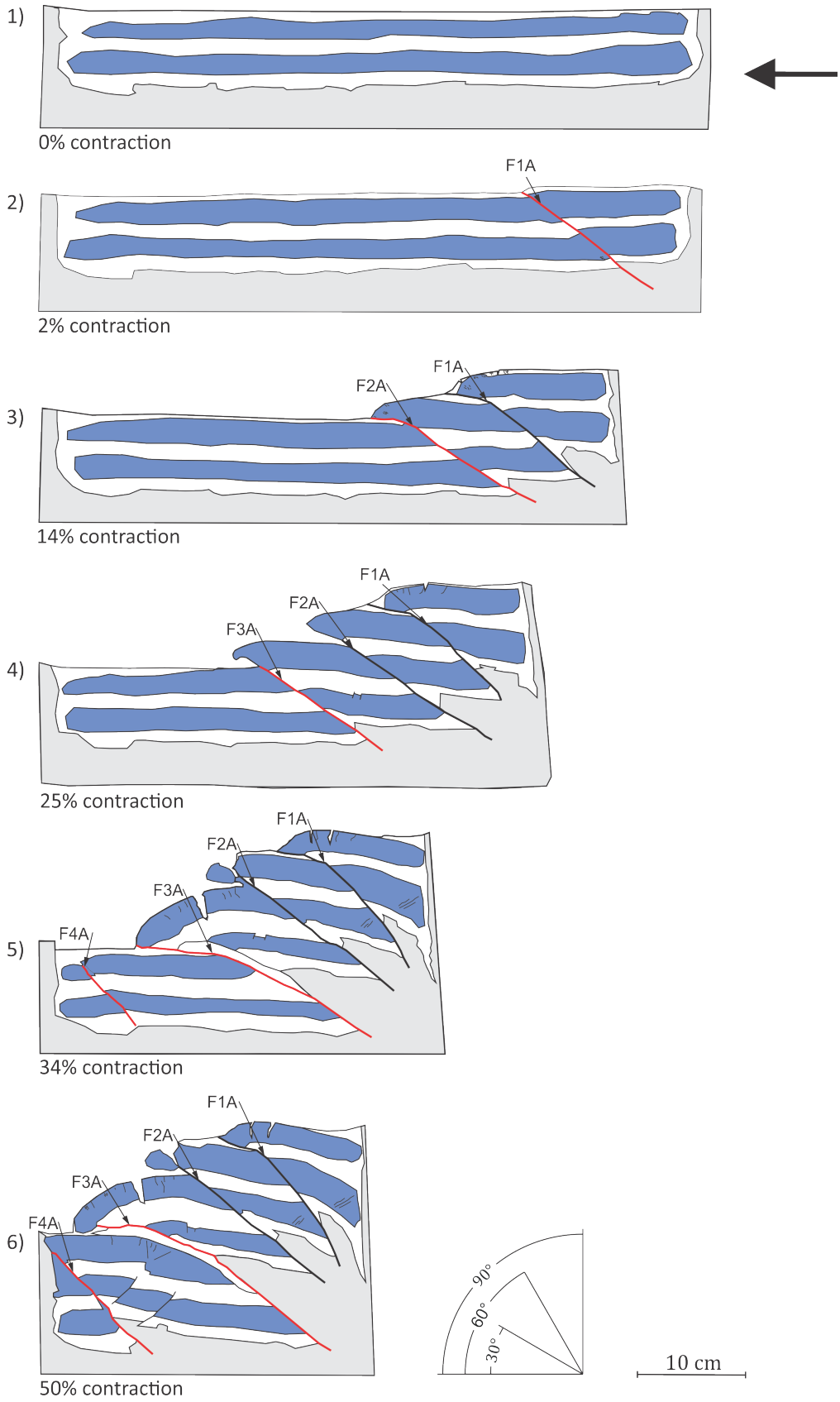

Fig. 5.1: Step-by-step development of experiment 12-14, side A. Red lines indicates active main faults on each step.

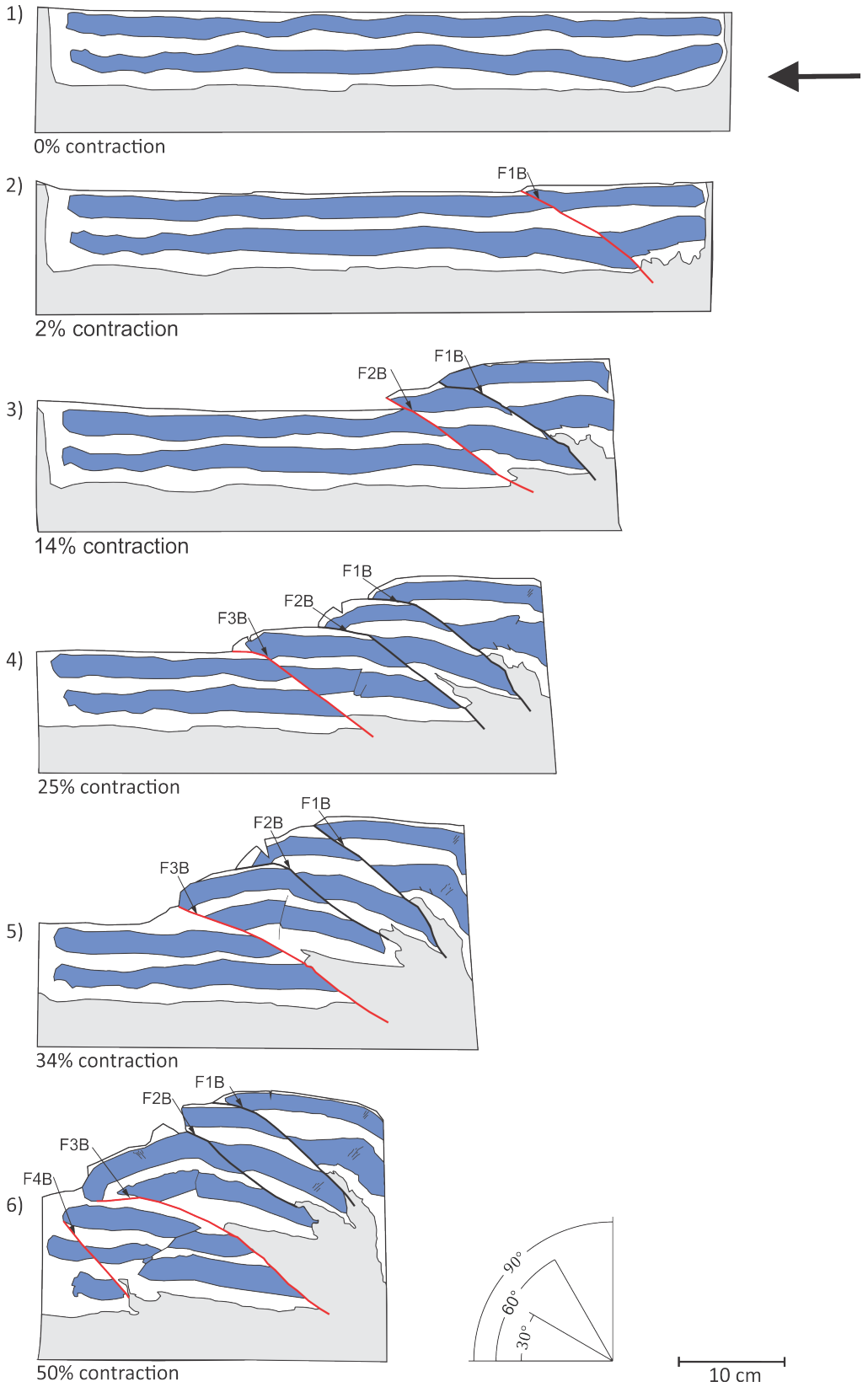

Fig. 5.2: Step-by-step development of experiment 12-14, side B.

Summary

Total contraction in this experiment was 50% and a presentation of the active faults at side A and B are shown in figure 5.3. A photo of the final result is shown in figure 5.4. Side A and B formed four main faults and produced faults after roughly the same amount of contraction with the biggest difference of 2%. F1 formed after 1.5-3% contraction on both sides and becomes inactive at 7-9% contraction. F2 is formed after 8-9% contraction and becomes inactive after 19-20% contraction. F3 fault is formed after 19-20% contraction and F4 is formed after 39% contraction. The two last main faults are active until the end of the experiment. The first fault has a short active period, and the active period of the faults increases progressively throughout the experiment. In addition, the displacement increases with progressive shortening. Side A creates two back thrusts, both around 40% contraction and both in the fourth fault block. Side B however, creates a back thrust in the third fault block after about 25% contraction and one back thrust within the fourth fault block after 43% contraction.

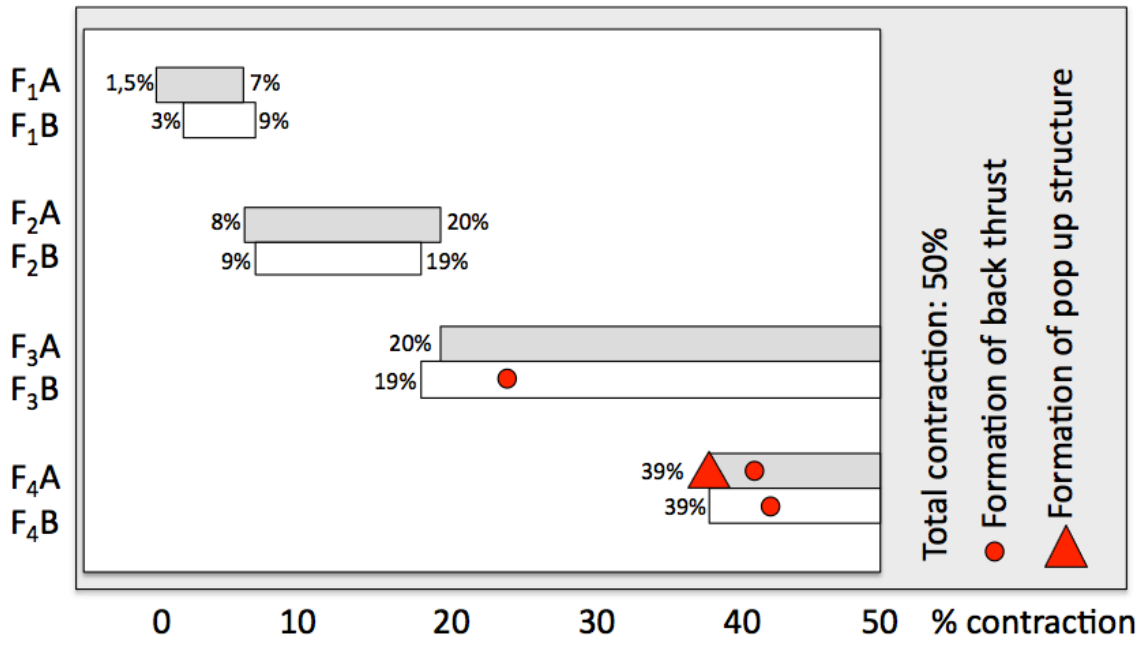

Fig. 5.3: Active faults in experiment 12-14. Fault number and side (A or B) are stated at the vertical axis and amount (%) contraction is stated at the horizontal axis. Formation of pop up structures and back thrusts are marked with red squares and dots respectively.

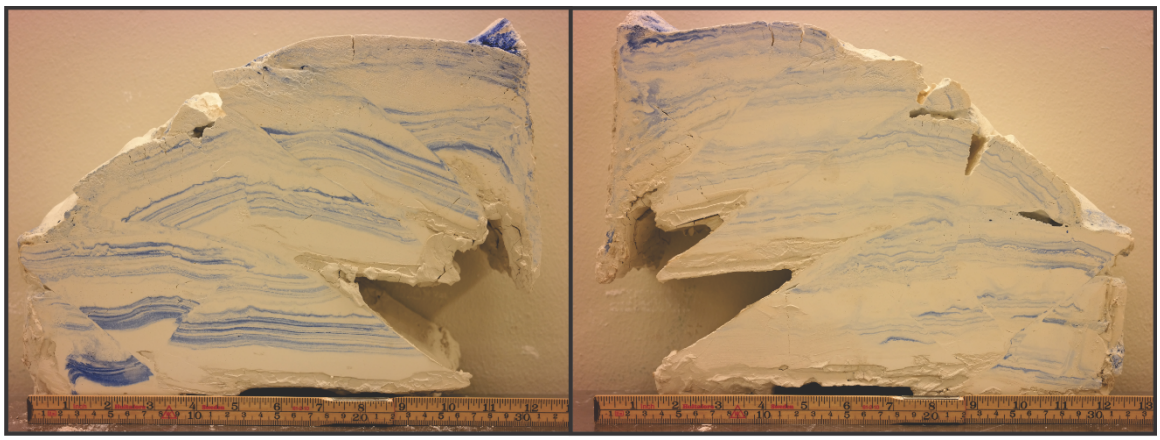

Side A Side B

Fig. 5.4: Side A (left) and B (right) photograph of the final result for experiment 12-14.

5.3 Experiment 15-14

The stepwise development of deformation throughout the experiment can be followed in figure 5.5 and 5.6.

Table 5.2: Experimental data for experiment 15-14.

Date	07.02.14
Plaster/water ratio	4 L plaster / 4 L water
Experimental conditions	2 cm horizontal barite basement
Experimental box	Narrow (9 cm width)
Start length	80 cm
End length	30 cm
Start height	6 cm
End height	17 cm
Note	Water percolated through the plaster, leaving a film of water on the surface

Step 2 – 6% contraction

Side A (Fig. 5.5-2): Small faults were formed in the top reference layer close to the moving wall after 4% contraction. These small faults have a displacement of approximately 0.4 cm and dip towards the moving wall. One of the faults develops into the first main fault, F_1A. At this stage, the fault has a displacement of 1 cm and a dip of 27°.

Side B (Fig. 5.6-2)**:** Initiation of two segments close to the moving wall is evident, one initiated from the base propagating upward and one initiated at the surface and propagates downward, until they submerge and form the first main fault, F_1B, just after 6% contraction.

Step 3 - 16% contraction

Side A (Fig. 5.5-3): F_1A has a displacement of 3 cm and a dip of 55°. The hanging wall bended towards the foreland as the fault propagated up the ramp. F_1A is at this stage no longer active. The small faults formed at the same time as initiation of F_1A,

have not developed further. The second main fault, F_2A, was formed after 13% contraction followed by the formation of two synthetic minor faults in the footwall.
Side B (Fig. 5.6-3)*:* F_1B is at this stage inactive with a displacement of 2 cm in the lowermost reference layer. The second main fault, F_2B, is initiated in the top reference layer. In the hanging wall, there are formed two smaller thrust faults with the same dip as F_2B of 20°.

Step 4 - 26% contraction

Side A (Fig. 5.5-4): F_2A is no longer active. The third main fault, F_3A, was formed after 20% shortening at the top of the reference layer and the displacement has progressively increased and is now 6 cm and the dip is 23°. The dip of F_1A and F_2A are constantly steepening as the shortening continues.
Side B (Fig. 5.6-4): F_1B and the synthetic faults are no longer active. F_2B has developed a displacement of 3 cm at the tip of the fault and is no longer active. The third main fault, F_3B, was formed after 19% contraction and is at this stage well developed with a displacement of 10 cm and a dip of 23°. The hanging wall has two thrust faults at the surface that have 0.2 cm displacement. As the fault grows, it bends down towards the stable wall.

Step 5 - 36% contraction

Side A (Fig. 5.5-5): F_3A has propagated developed a displacement of 9 cm in the lowermost reference layer. The dip is decreasing as the fault bends over the undeformed layers. F_3A is at this stage no longer active. The fourth main fault, F_4A, is formed after 35% contraction and has a dip of 32° and a displacement of 1.5 cm in the lowermost reference layer. The fault plane is divided in two parallel lines, which leads to the formation of a lens shape structure close to the top of the fault. F_3A bends towards the stable wall.
Side B (Fig. 5.6-2): F_3B has at this stage a displacement of 10 cm and becomes inactive. The small thrust faults on top of F_3B have not developed any further. After 31% contraction, the fourth main fault, F_4B, was formed. The fault has now climbed

over the ramp and is bending towards the stable wall. F_4B has at this stage developed a displacement of 4 cm and a dip of 20°.

Step 6 - 56% contraction

Side A (Fig. 5.5-6): Three small normal faults are formed at the tip of F_3A as a result of the bending and extension of the fault. F_4A has created a large displacement of 13 cm. The fault is still active and has bended, almost reaching the stable back wall. A small thrust fault has formed underneath F_4A and has a shallow dip of 13° and a displacement of 1.5 cm. Two small reverse faults are also formed close to the stable back wall.

Side B (Fig. 5.6-6): F_4B has bended so much that the fault breaks and creates several normal faults at the tip as a result of the bending. Another main fault, F_5B, was developed in the footwall of F_4B after 40% contraction and became inactive after further 3% shortening. The fault has some irregularities on the fault plane and has developed a displacement of 4 cm. A sixth main fault, F_6B, is developed close to the stable wall, with a dip of 24° and a displacement of 1 cm.

Step 7 - 62% contraction

Side A (Fig. 5.5-7): F_4A has a displacement of 20 cm. The small fault formed in the footwall of F_4A formed at 56% contraction has not developed any further. One of the small reverse faults created close to the stable wall at 56% contraction has developed to become the fifth main fault, F_5A. At this stage, F_5A has a dip of 23° and a displacement of 4 cm. The fault is developing to become an out-of-the-hinge thrust at the end of shortening.

Side B (Fig. 5.6-7): F_4B is no longer active. F_5B has not developed more displacement and has also become inactive. F_6B has propagated forward and the tip bended down as the rest of the fault propagated, which lead to the development of an out-of-the-hinge thrust.

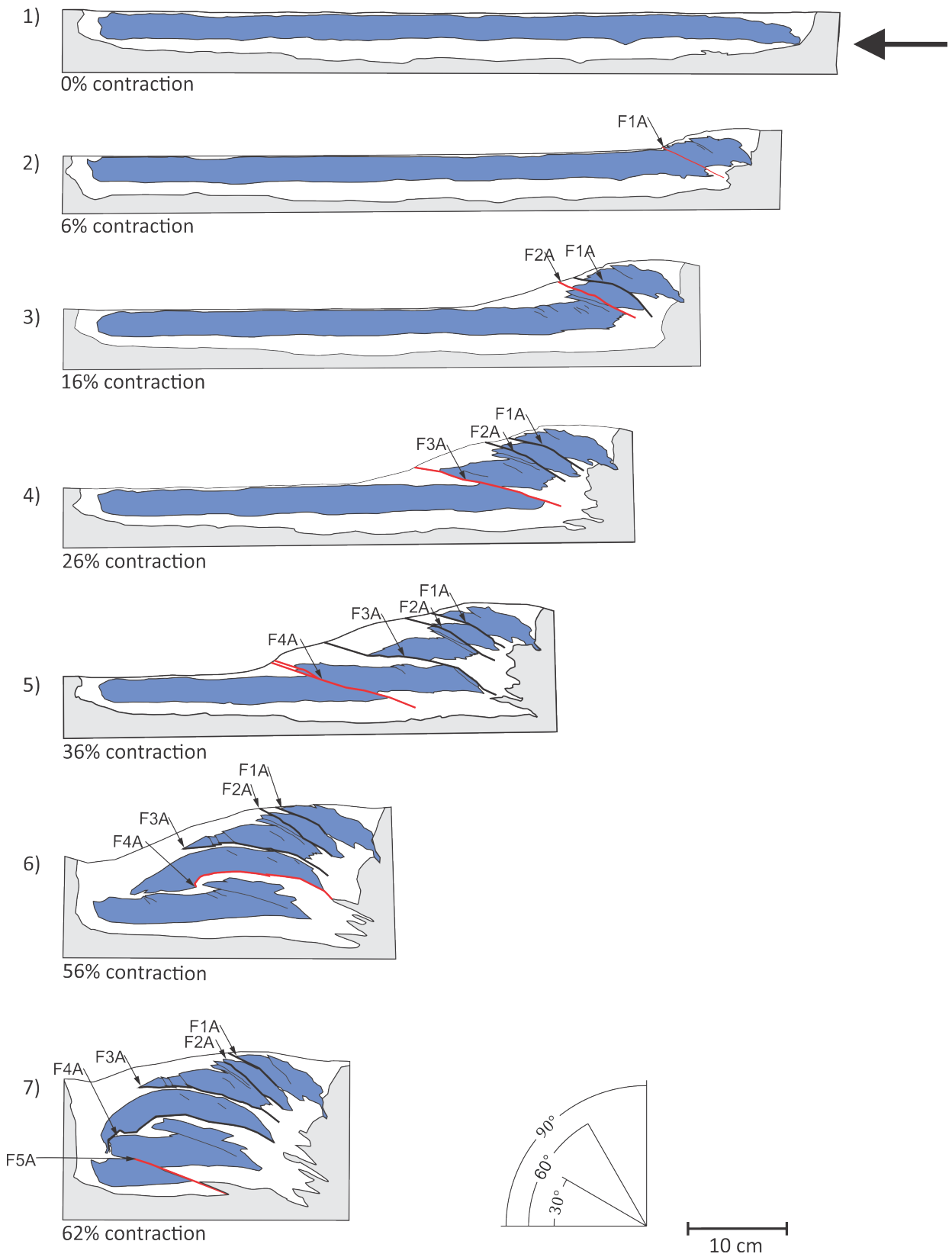

Fig. 5.5. Step-by-step development of experiment 15-14, side A

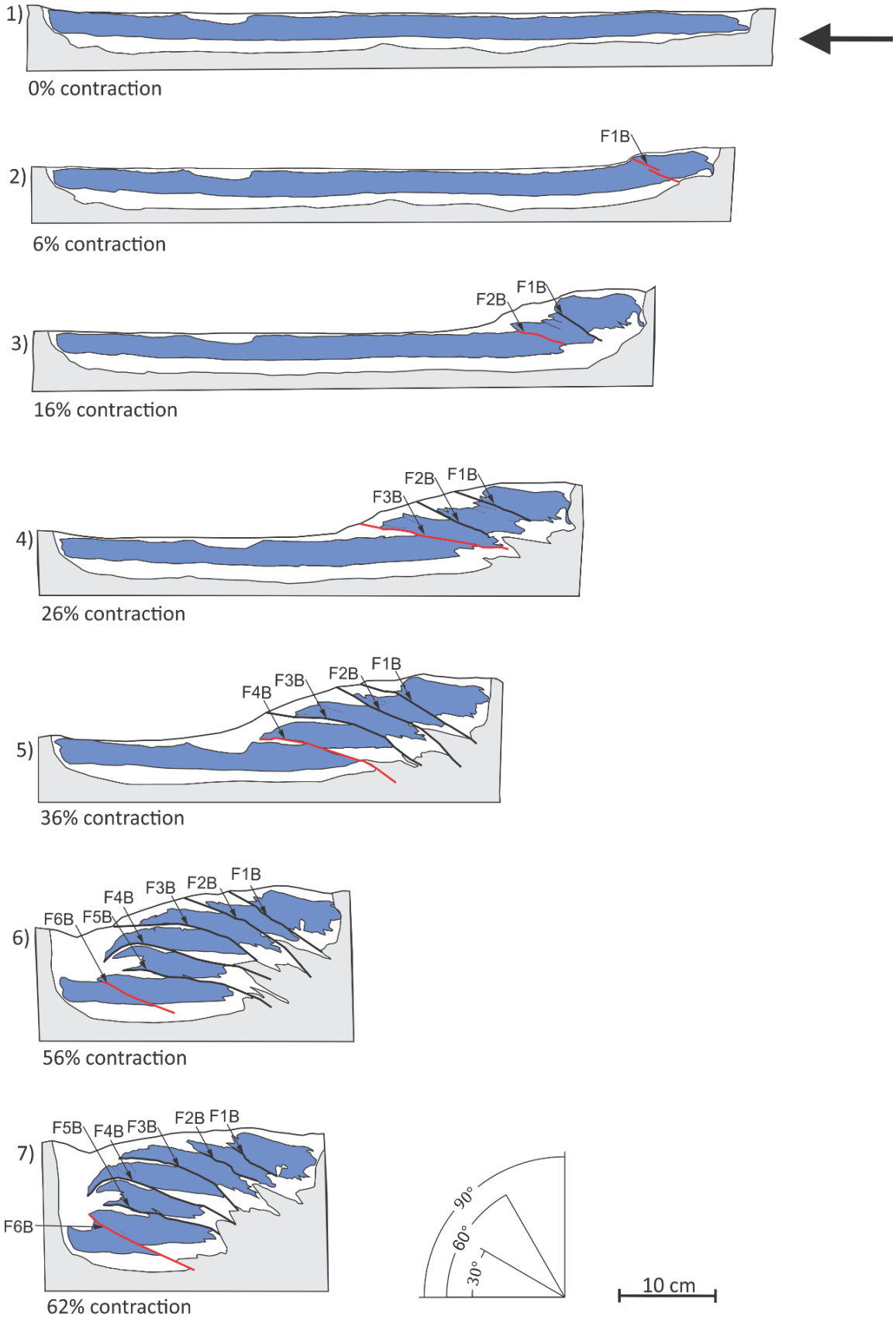

Fig. 5.6. Step-by-step development of experiment 15-14, side B

Summary

The total contraction in this experiment was 62% and a presentation of the active faults on side A and B are shown in figure 5.7. A photo of the final result is shown in figure 5.8. Side A produced five main faults while side B produced six main faults, and the fault development of the two sides becomes different towards the end of the experiment. F1 are produced between 5-7% contraction and branch out from the same place near the moving wall. The main difference between F_1A and F_1B is that F_1B is developing from two segments that are moving towards each other and F_1A is developing from one segment that is developing in one direction. F1 became inactive after 11% contraction. F2 were formed between 13-15% contraction and became inactive after 17% contraction. F3 were formed between 19-20% contraction and becomes inactive after 30-32% contraction. F4 were formed after 31-35%. While F_4A is active until the end, F_4B became inactive after only 38% contraction and a new fault, F_5B, was formed at 40% contraction, which was also active for a short amount of time. The two last faults on each side, F_5B and F_6B, were formed at 56% contraction and were active until the end. The experiment did not produce any back thrusts or pop ups.

The experiment appears to have a less viscous plaster than most of the other experiments because of the late initiation of faults and the ductile nature of the deformation. The older faults got a steeper dip with increasing shortening. When the faults were bent at a late stage in the experiment, it resulted in the formation of several normal faults. When the extension happened while the fault was still active, the fault propagated past the extensional normal faults and formed an out-of the-hinge thrust.

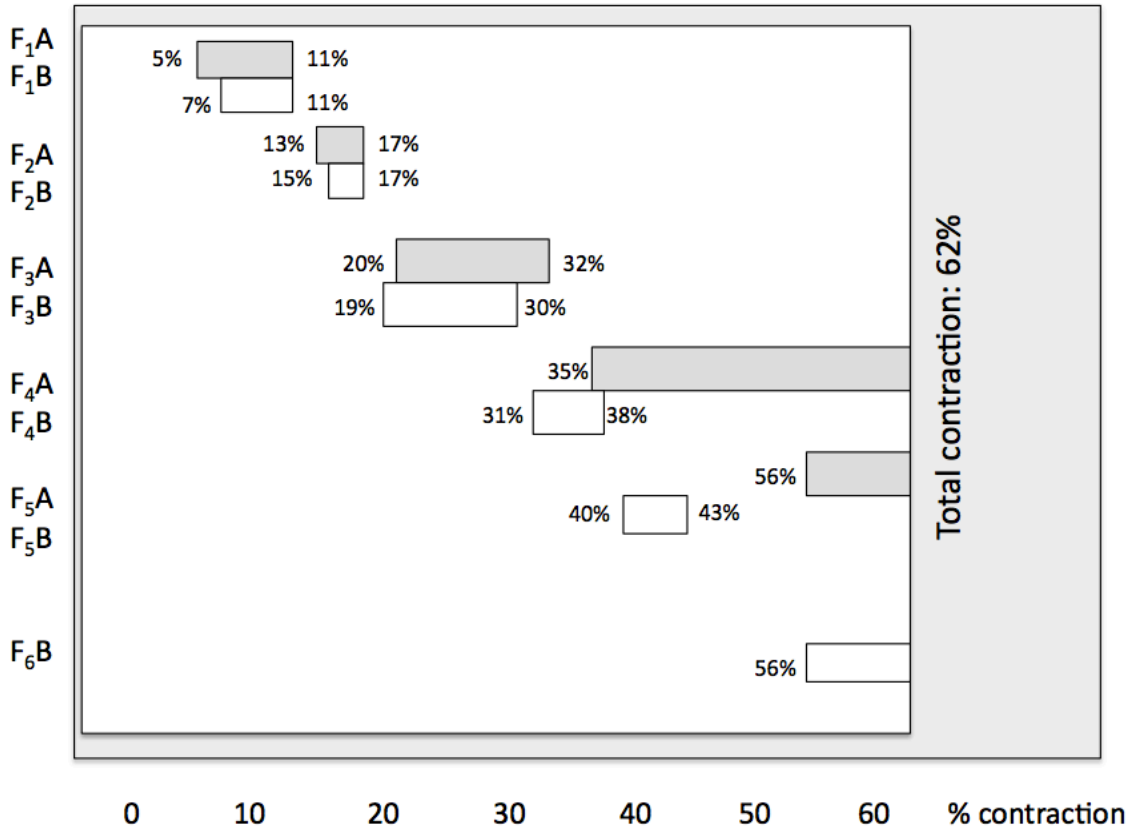

Fig. 5.7: Active faults in experiment 15-14. Fault number and side (A or B) of formation are stated at the vertical axis and amount contraction (%) is stated at the horizontal axis.

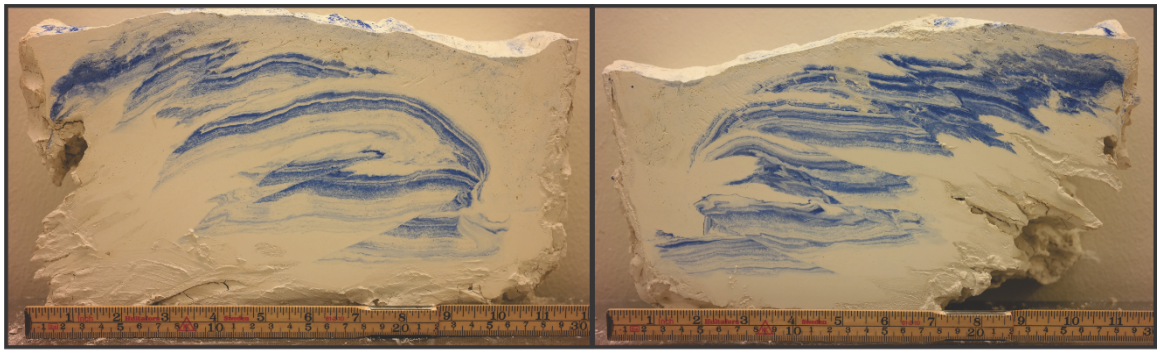

Side A Side B

Fig. 5.8: Photograph of the final result for experiment 15-14, side A (left) and B (right).

5.4 Experiment 27-14

The stepwise development of deformation throughout the experiment can be followed in figure 5.9 and 5.10.

Table 5.3: Experimental data for experiment 27-14.

Date	22.10.14
Plaster/water ratio	4.2 L plaster/3 L water
Experimental conditions	2 mm thin, horizontal basement
Experimental box	Narrow (9 cm width)
Start length	63 cm
End length	32 cm
Start height	7 cm
End height	16 cm
Note	Approximately same amount of plaster as 15-14 was used, however less water made the plaster more viscous

Step 2 – 6% contraction

Side A (Fig. 5.9-2): F_1A was initiated in the lower reference layer after 4% contraction and cuts through the entire reference layer after 5% contraction. The maximum displacement of F_1A is 0.5 cm and is at the base of the box, however the displacement decreases towards the surface. The dip angle is approximately 36° towards the moving wall.

Side B (Fig. 5.10-2): F_1B is initiated in the lower part of the reference layer, then propagating upwards towards the top of the plaster. The fault formed close to the moving wall with a dip of 32° and a displacement of approximately 1 cm in the lower part of the reference layer. Parallel to the fault plane, 1 cm towards the moving wall, a minor fault is initiated with the same dip and displacement as F_1B.

Step 3 – 11% contraction

Side A (Fig. 5.9-3): F_1A has developed a higher maximum displacement of about 2 cm and is no longer active. At this stage, a second major fault, F_2A, is formed parallel to F_1A, with a dip of 26° and 1 cm displacement at the base, decreasing upwards. Several synthetic minor faults are observed near the fault plane.

Side B (Fig. 5.10-3): F_1B has a larger displacement of approximately 2 cm. A fault is initiated in the upper part of the reference layer with a displacement of 0.5 cm.

Step 4 – 23% contraction

Side A (Fig. 5.9-4): F_2A has continued the propagation and has formed a displacement of about 4 cm. F_2A is after this point no longer active. A ramp was created after 20% contraction, localized in the middle of the experimental box, and a fault starts climbing. The fault has a displacement of about 0.5 cm and a dip of 35° towards the moving wall. This fault is developing to become the third major fault, F_3A.

Side B (Fig. 5.10-4): The fault initiated in the top layer has developed to become a second main fault, F_2B. At this stage, the fault has a maximum displacement of 5 cm in the lower part of the reference layer and is no longer active. As a result of the constant shortening, layers in the footwall have been folded. Two parallel, smaller faults were formed in the middle of the experimental box. A third main fault, F_3B, formed in the same area as the smaller faults. The fault has a dip of approximately 34° and a displacement of 1.5 cm in the lower part of the reference layer. A back thrust with small displacement is formed in the hanging wall of F_3B.

Step 5 – 31% contraction

Side A (Fig. 5.9-5): F_3A has propagated up the ramp, creating a displacement of 8 cm. The layers in the hanging wall are folded. In addition, the hanging wall has formed an out-of-the-sequence thrust with 1 cm displacement and a dip of 30°.

Side B (Fig. 5.10-5): The dip of F_1B and F_2B have increased to become 43° and 45° as more faults are accreted at the toe of the wedge. F_3B has propagated forward and creates a large displacement of 13 cm. F_3B fault plane is large and has a

characteristically "S" geometry in the vertical profile. Small faults have formed at the tip of the fault.

Step 6 – 45% contraction

Side A (Fig. 5.9-6): After 45% shortening, F_1A has developed a steep dip of 57°, while F_2A has developed a dip of approximately 37°. F_3A has moved with a dominantly reverse dip slip movement over the ramp creating a typical horse shape formed like an "S". The displacement of the thrust is approximately 14.5 cm and the dip is steep at first, then decreasing towards the tip. The fault is after this stage no longer active. Three small reverse faults with a dip of 50° and a displacement of 0.4 cm are created close to the stable wall. Soon after, a back thrust is formed between F_3A and the smaller faults, with a dip of 46° and a displacement of 0.5 cm in the lower part of the reference layer. The small faults and the back thrust create a pop up structure.

Side B (Fig. 5.10-6): F_3B has started to bend down towards the foreland. The small thrust faults formed at the fault tip have not developed further. Close to the stable wall, there are formed two small thrust faults with a dip towards the moving wall. An out-of-the-sequence fault forms the lower part of the reference layer between F_2B and F_3B with a shallow dip towards the moving wall.

Step 7 - 49% contraction

Side A (Fig. 5.9-7): One of the small reverse faults closest to the stable wall develops to become a main fault, F_4A. The other two smaller faults becomes inactive. A second back thrust develops parallel to the first back thrust with a displacement of about 0.3 cm in the lower part of the reference layer and a dip of approximately 45°.

Side B (Fig. 5.10-7): The out-of-sequence-thrust is no longer active. Only one of the thrust faults formed at 45% contraction has developed further and become the fourth main fault, F_4B, which at this point is the only active fault. F_4B developed a displacement of 3 cm.

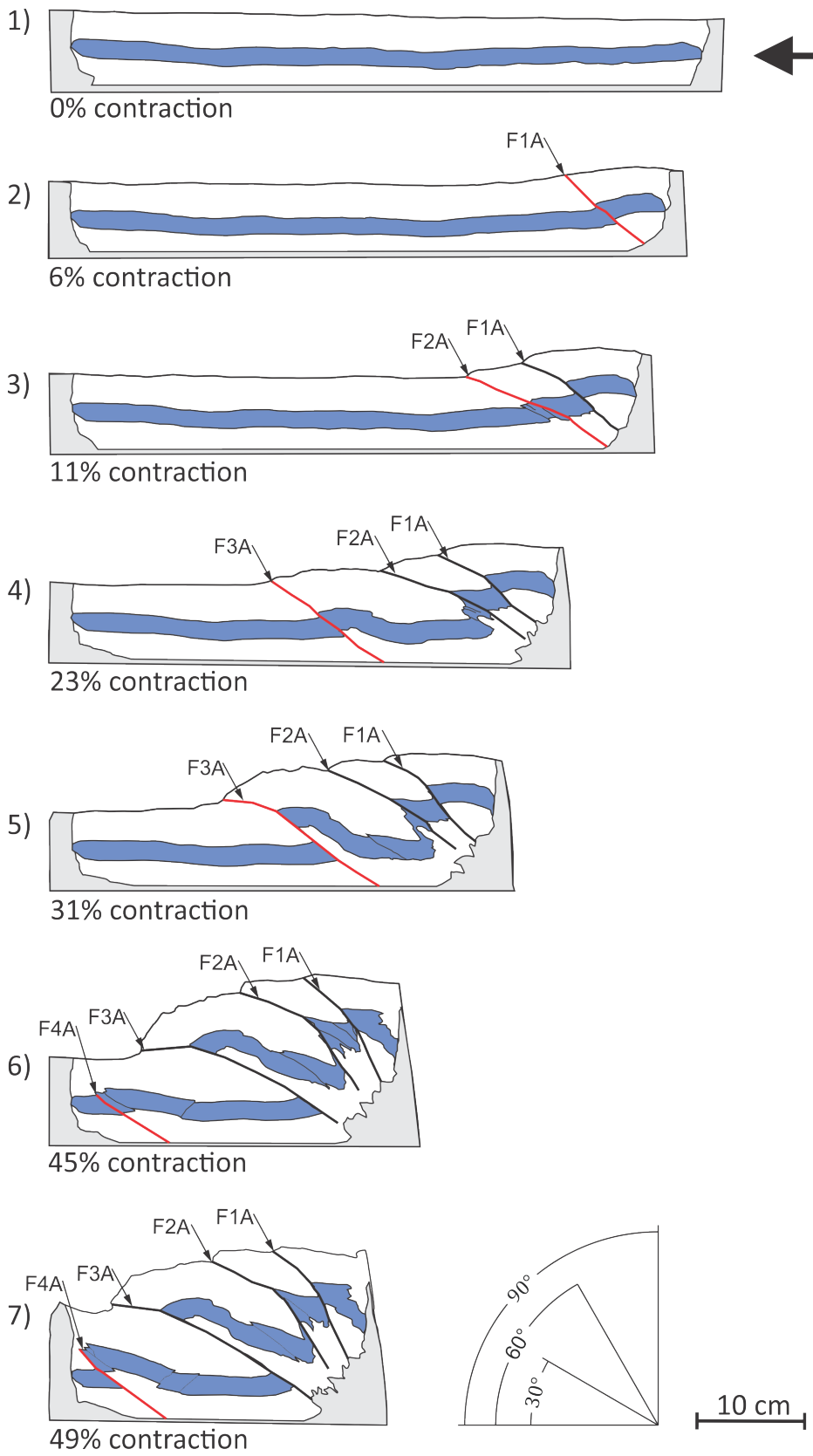

Fig. 5.9: Step-by-step development of experiment 27-14, side A.

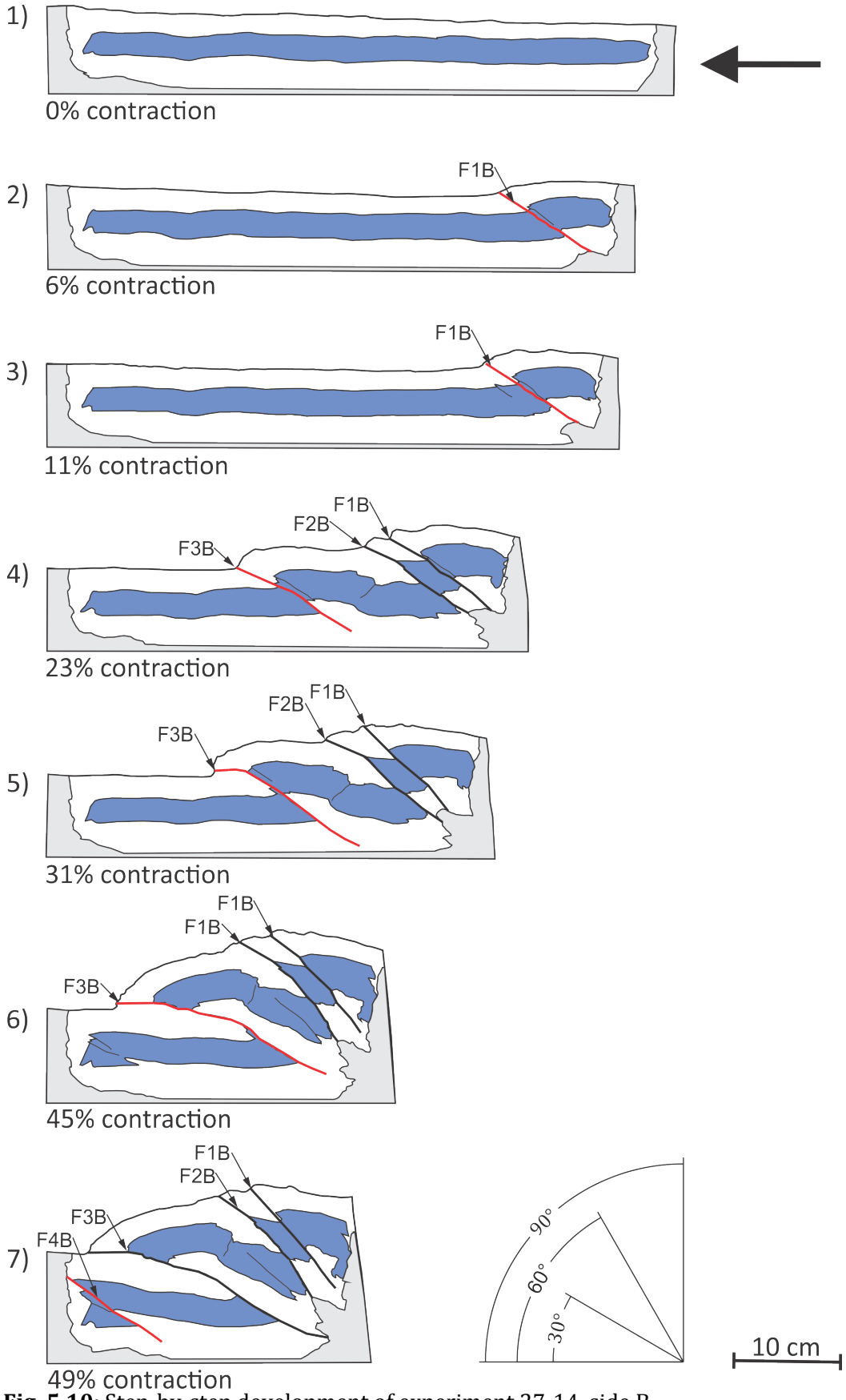

Fig. 5.10: Step-by-step development of experiment 27-14, side B.

Summary

The total contraction in this experiment was 49% and a presentation of the active faults on side A and B are shown in figure 5.11. A photo of the final result is shown in figure 5.12. The experiment was set up with a thin layer of plaster and only one reference layer was painted on the glass wall. Four main faults were formed, one of them developed a typical "S" shape geometry with a large displacement. The thin, horizontal basement used in this experiment was mainly to act as a gliding surface to see how the material would act with a very thin basement in a narrow experimental box. The deformational development on both side A and B are very similar, and fault activity time for the individual faults increase towards the end (same as experiment 12-14). F1 are formed between 5-7% contraction and becomes inactive at 9-11%. The dip increases with increasing shortening. F2 are formed from 9-12% contraction and becomes inactive at 17-20% contraction. There is formed a small out-of-the-sequence thrust fault between F2 and F3 at both sides. F3 are formed from 20-23% contraction and becomes inactive at 43-44% contraction. F4 is on both sides created in the last few percentages of shortening. The main difference between side A and B becomes apparent at the end of the experiment. While side A develops two back thrusts during 46-49% contraction, with one being part of a pop up structure, side B develops only one back thrust, in the hanging wall of F_3B, which is fully developed after only 26% contraction.

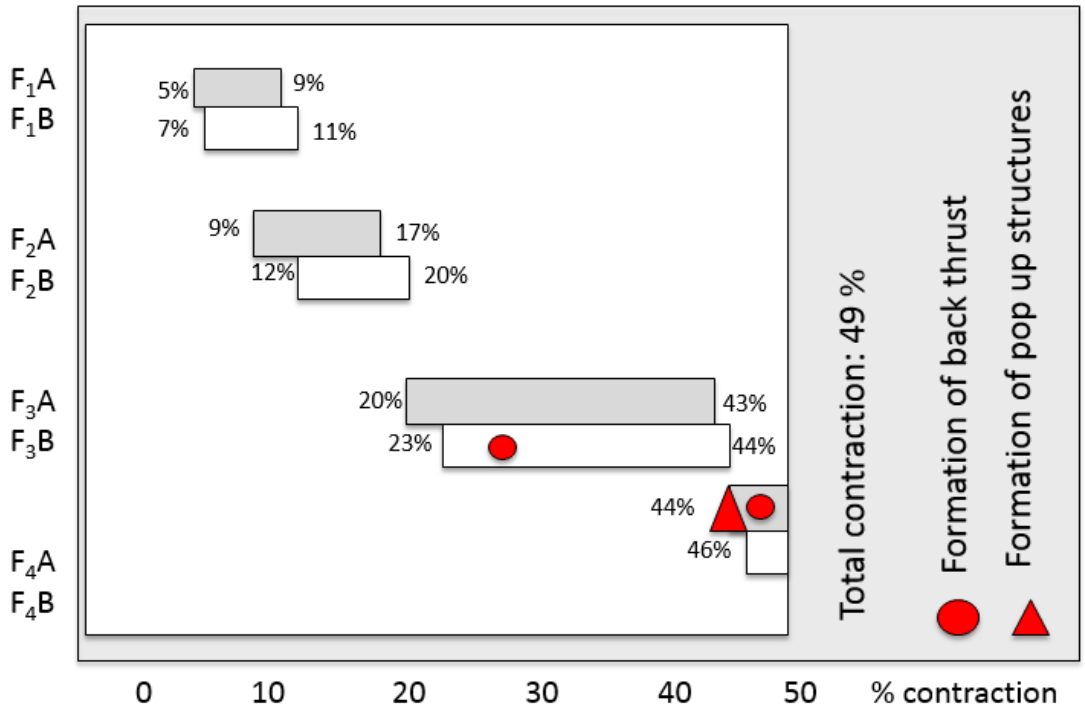

Fig. 5.11: Active faults in experiment 27-14. Fault number and side (A or B) are stated at the vertical axis and amount (%) contraction is stated at the horizontal axis. A pop up structure is formed at side A at 44% and short time after, at 47%, a back thrust is formed behind it. A back thrust was formed after 26% in F_3B.

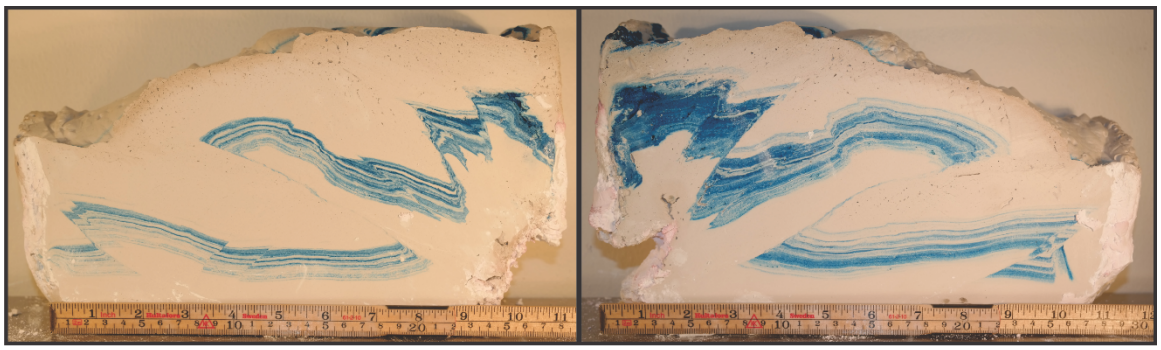

Side A Side B

Fig. 5.12: Photograph of the final result for experiment 27-14, side A (left) and B (right).

5.5 Experiment 44-14

The stepwise development of deformation throughout the experiment can be followed in figure 5.13 and 5.14.

Table 5.4: Experimental data for experiment 44-14.

Date	03.12.14
Plaster/water ratio	10 L plaster/6 L water
Experimental conditions	2 cm horizontal barite basement
Experimental box	Wide (14 cm width)
Start length	84 cm
End length	32 cm
Start height	8 cm
End height	29 cm

Step 2 – 2% contraction

Side A (Fig. 5.13-2): The first main fault, F_1A, was initiated in the lowermost reference layer closest to the moving wall after 1% contraction and the top reference layer was folded as a response to the fault development. After 2% contraction, F_1A had propagated through the entire plaster layer. The displacement of the fault is decreasing as the fault approaches the surface, with 1.8 cm displacement in the lowermost reference layer and 0.4 cm displacement in the top reference layer. The dip of the fault increases as it approaches the top, from 26° at the base to about 45° close to the surface.

Side B (Fig. 5.14-2): The first main fault, F_1B, is initiated at the base of the plaster close to the moving wall with a dip of 26°. The fault has not completely propagated through the entire layer, and creates a fault propagation fold at the tip of the fault. In the lower reference layer, a small synthetic fault has formed next to the fault plane. After further 0.5% contraction, the main fault has propagated through the entire layer.

Step 3 - 13% contraction

Side A (Fig. 5.13-3): F_1A reached a maximum displacement of 8 cm and is no longer active. The dip is approximately 25° in the hangingwall, but is steepening towards the moving wall, becoming almost 65°. A large minor fault with a steep dip has been formed in the footwall of F_1A. The minor fault has propagated to the surface, becoming narrower as it approaches the top. Four small reverse faults with a dip towards the stable wall have been formed in the lower reference layer next to the steep minor fault, creating a small domino structure.

Side B (Fig. 5.14-3): The minor synthetic fault has not developed any further. The hanging wall of F_1B has bent towards the plaster layer closer to the stable wall. A minor fault with a steep dip in the lower reference layer is formed close to F_1B with a displacement of approximately 2 cm. Another minor fault has been created, also in the lowermost reference layer. This fault is starting to propagate towards the top reference layer, but only folding is accommodating the surface. A major fault, F_2B, has been formed next to the two minor faults. F_2B has a dip of 37° and a displacement of 2 cm in the lower part of the reference layer.

Step 4 - 25% contraction

Side A (Fig. 5.13-4): The domino structure has been cut through by a second main fault, F_2A. F_2A is no longer active and a vertical build up of F_1A and F_2A have started as the contraction proceeds. Both fault blocks have developed several small vertical fractures at the top. A third main fault, F_3A, has formed from the lower part of the reference layer with the same dip as F_2A. F_3A has a displacement of 3 cm in the lower reference layer and behaves more ductile at the top accommodated by folding of the layer, which forms a fold-propagation fault. A pop up has been developed in the front of F_3A with approximately 0.5 cm displacement on each side.

Side B (Fig. 5.14-4): F_1B is no longer active. F_2B has now a similar dip as F_1B. A pop up structure is formed in ahead of F_2B, further towards the stable wall. The fore thrust of the pop up structure forms progressively higher displacement than the back thrust, which leads to the development of a third main fault, F_3B. F_3B has at this

point a displacement of 4 cm and a dip of approximately 37°. The back-thrust that forms the pop up structure has a displacement of 0.5 cm.

Step 5 - 31% contraction

Side A (Fig. 5.13-5): F_3A is no longer active. The pop up structure has developed to become a fourth main fault, F_4A, with a back-thrust. F_4A has at this point a displacement of 6 cm and a dip of approximately 36°.

Side B (Fig. 5.14-5): F_2B is no longer active. F_3B has now a displacement of 8 cm in the lower part of the reference layer and a dip of 36°. The tip of F_3B is starting to bend down towards the plaster layer closer to the stable wall, creating fractures at the top of the plaster.

Step 6 - 48% contraction

Side A (Fig. 5.13-6): F_4A has propagated forward and developed a 8 cm displacement. The fault has bent down towards the underlying layers and the extension leads to a large vertical crack developing in the fault block. Small reverse faults have developed in the footwall of F_4A and form with progressive shortening a large pop up structure that cuts through both the bottom and the top reference layer.

Side B (Fig. 5.14-6): The bending leads to extension of the third fault block and formation of a 4 cm deep vertical crack. Another pop up structure is formed, and subsequent minor back-thrusts develop as the fault block deforms while advancing up the ramp.

Step 7 - 60% contraction

Side A (Fig. 5.13-7): F_4A is no longer active. The large pop up structure creates a fifth main fault, F_5A. A part of the pop up structure is smeared between the fault plane. The fracture developed in F_4A has cut through the fault block, leading to a collapse of the fault block. It has also developed larger fractures in the hanging wall of F_5A.

Side B (Fig. 5.14-7): F_3B is no longer active. The third fault block is cut entirely by the crack and has collapsed. The pop up structure has been cut through to create a fourth main fault, F_4B, with a dip of 41°.

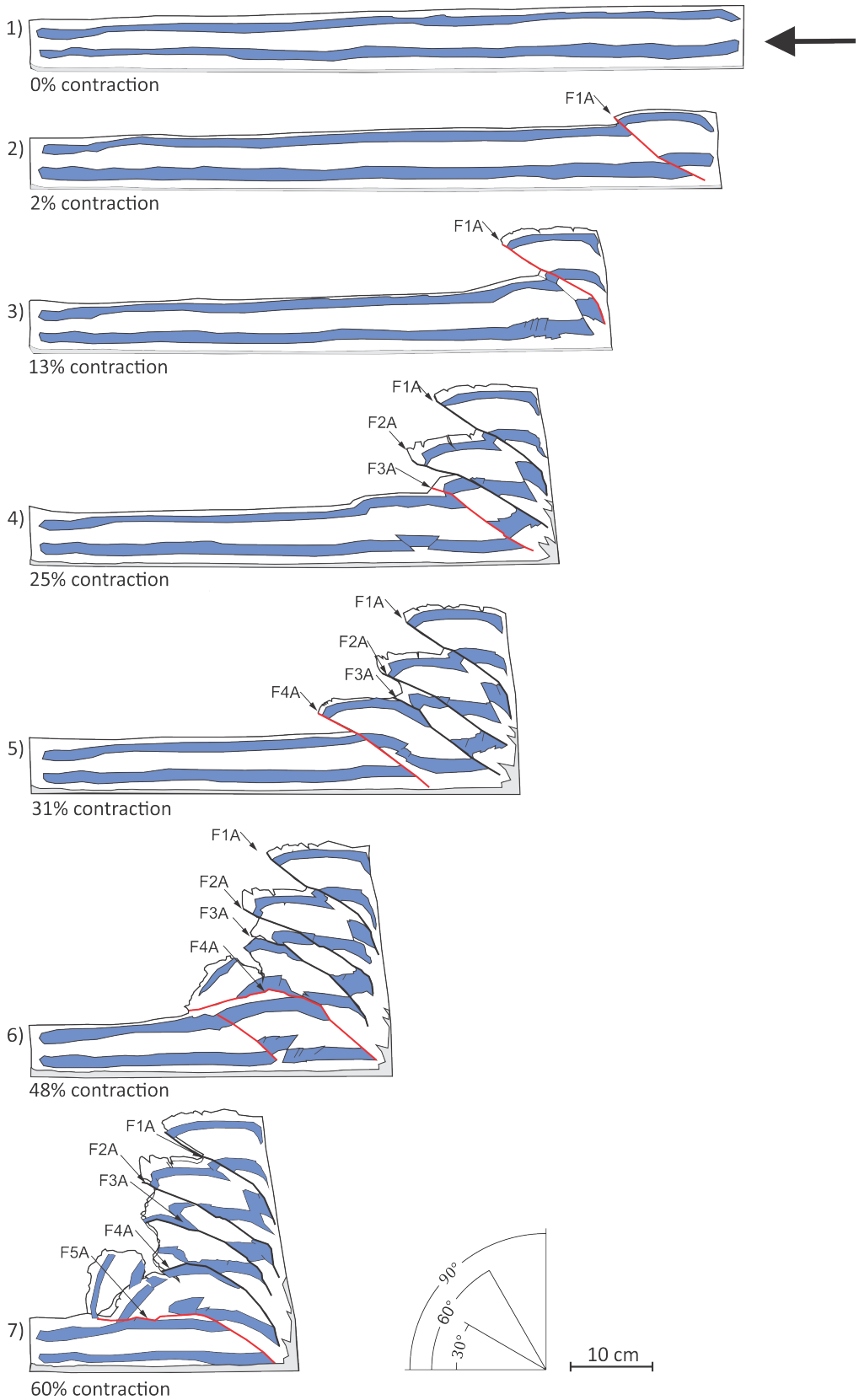

Fig. 5.13: Step-by-step development of experiment 44-14, side A

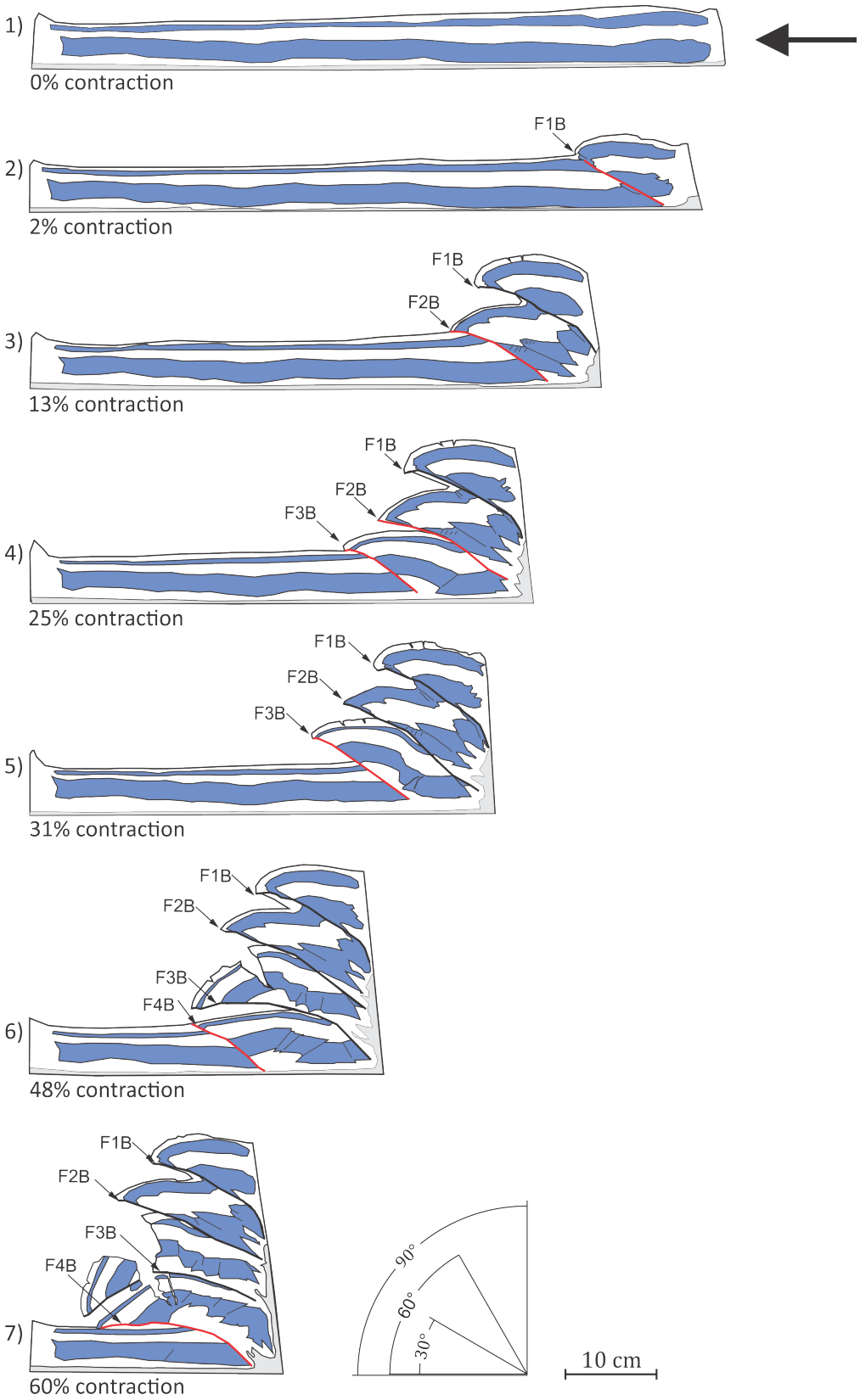

Fig. 5.14: Step-by-step development of experiment 44-14, side B

Summary

The total contraction in this experiment was 60% and a presentation of the active faults at side A and B are shown in figure 5.15. A photo of the final results is shown in figure 5.16. Side A produced five main faults, whereas side B produced four main faults. F1 is formed after 2% contraction and is inactive after 10% contraction on both side A and B. A minor fault with similar dip and displacement was created on both sides close to F1. The minor faults have steeper dip than main faults when first initiated. F2 is formed after 12-14% contraction and is inactive until 20-21% contraction. F_3A is formed after 20% contraction and become inactive at 25% contraction while F_3B is formed at 24% contraction and lasts much longer, until 47% contraction. F_4A is formed at 24% and is inactive at 43% contraction. The last fault at side A and B forms at 46% and both are active until the end of the experiment. Side A produced most amount of faults with shorter active periods, in opposed to side B which developed least amount of faults, but had faults with longer active periods. Side A also had a rapid formation of 3 main faults in the middle of experiment, approximately from 14-24% contraction.

The fault blocks increase in size as the number of fault blocks increases. This leads to the cracks and collapse of the youngest fault blocks (F4 on side A and F3 on side B). Towards the middle and end of the experiment, a pop up structure is formed prior the formation of main faults. The ramp is squeezed against the moving wall, creating an unusual high ramp dip angle.

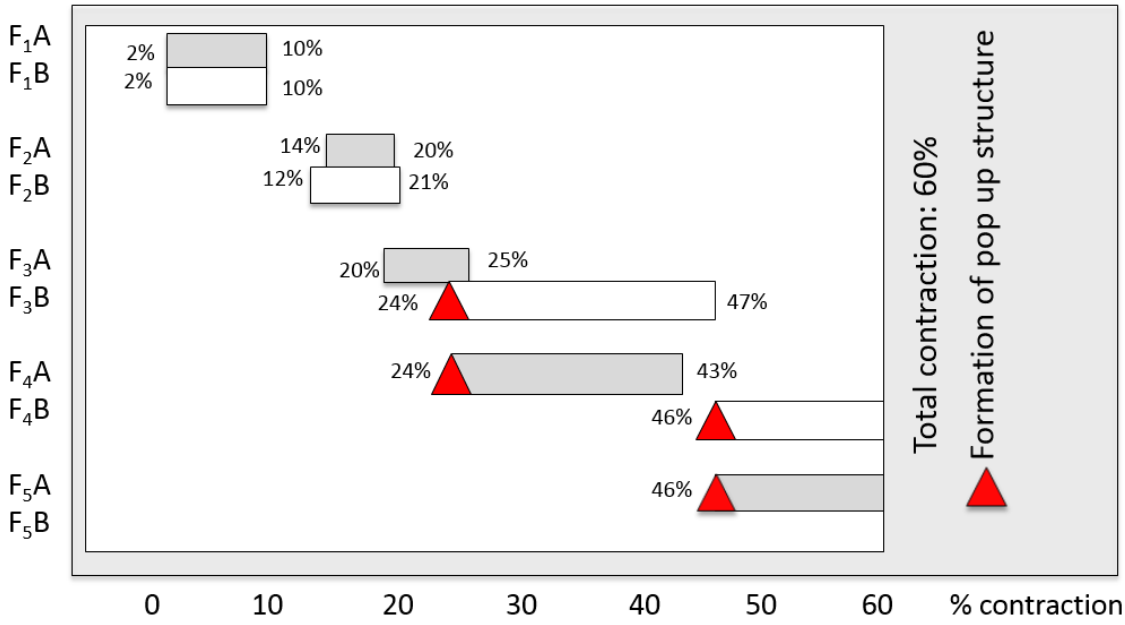

Fig. 5.15: Active faults in experiment 44-14. Fault number and side (A or B) of formation are stated at the vertical axis and % contraction is stated at the horizontal axis. Pop ups were formed at the end of the two last faults on each side.

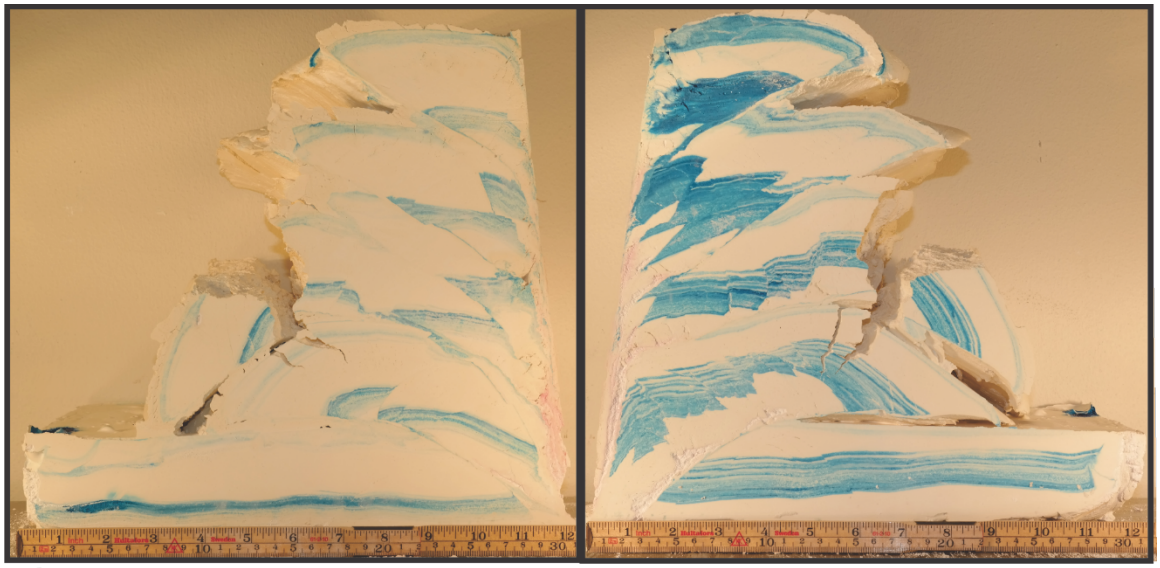

Side A Side B

Fig. 5.16: Photograph of the final results for experiment 44-14, side A (left) and B (right).

5.6 Experiment 45-14

The stepwise development of deformation through the experiment can be followed in figure 5.17 and 5.18.

Table 5.5: Experimental data for experiment 45-14.

Date	04.12.14
Plaster/water ratio	10 L plaster/6 L water
Experimental conditions	30 cm long ramp which is 4-4.5 cm high and has an inclination of 20°
Experimental box	Wide (14 cm width)
Start length	84 cm
End length	33 cm
Start height	9 cm
End height	28 cm
Note	The experiment has the same length and plaster/water ratio as 44-14

Step 2 - 3% contraction

Side A (Fig. 5.17-2): The first main fault, F_1A, is formed in the lower part of the reference layer with a dip of approximately 36° towards the moving wall. The fault has a displacement of approximately 2 cm close to the barite/plaster boundary, which decrease towards the surface.

Side B (Fig. 5.18-2): The first main fault, F_1B, is initiated in the lowermost reference layer and creates a fault-propagation fold as it propagates toward the surface. The fault has at this point a dip of 36° towards the moving wall and a displacement of 1 cm close to the barite/plaster boundary, decreasing as the fault approaches the surface.

Step 3 - 13% contraction

Side A (Fig. 5.17-3): The tip of F_1A starts to bend as the fault passes the ramp, creating small vertical cracks at the top of the fault block as a result of the bending.

The hanging wall of F_1A is squeezed against the moving wall, creating many small, steep, almost vertical reverse faults. F_1A becomes inactive after this point. The second main fault, F_2A, is formed with a dip of approximately 33° towards the moving wall. Small synthetic minor faults are formed along the fault plane.

Side B (Fig. 5.18-3): F_1B has bent at the fault tip. The fault has developed a maximum displacement of 7 cm in the lowermost reference layer and is no longer active. A steep minor fault has developed in the lower reference layer of the footwall of F_1B, with a maximum displacement of 1 cm. A second main fault, F_2B, formed which was also initiated in the lower reference layer. At this point, the fault has a displacement of 5 cm in the lower reference layer and a dip angle of 37°. A minor fault is formed in the top reference layer in the hanging wall in association with the development of F_2B.

Step 4 - 17% contraction

Side A (Fig. 5.17-4): The small synthetic faults created along the fault plane of F_2A after 13% contraction have not developed any further. F_2A has developed a maximum displacement of 4 cm in the lower reference layer and is no longer active. The third main fault, F_3A, is formed close to the base of the box with a dip of 31°. Minor faults are formed in the top reference layer in both the footwall and hanging wall, including small back thrusts in the lower reference layer.

Side B (Fig. 5.18-4): Two minor faults are formed in the top reference layer in the footwall of F_2B with a 35° dip angle.

Step 5 - 25% contraction

Side A (Fig. 5.17-5): F_3A is no longer active. The fourth main fault, F_4A, initiated in the lower reference layer after 21% contraction and propagated to the surface with a dip angle of 41°. Small, closely spaced back thrusts were formed at the top of the lower reference layer prior to main fault formation.

Side B (Fig. 5.18-5): F_2B is no longer active. A third main fault, F_3B, is developed from the lowermost reference layer and has at this stage a displacement of 6 cm in the

lower reference layer. Several small synthetic faults formed in the hanging wall of F_3B ahead of the propagating fault.

Step 6 - 40% contraction

Side A (Fig. 5.17-6): F_4A is no longer active. The tip of F_4A has bent so much that the fault tip has broken off, which created two large, vertical fractures at the top. A large back thrust is formed in the middle of the model, close to the steepening of the ramp.

Side B (Fig. 5.18-6): As F_3B propagated up the ramp, some of the ramp collapsed, which resulted in a lens shape along the fault plane. In addition, several reverse faults have been formed in the lower reference layer. A vertical fracture is a result of bending of the fault tip and appears at the top of the third fault block. F_3B has at this point developed a displacement of 11 cm and is no longer active. A pop up structure develops close to the stable wall, just above the barite ramp, with a larger displacement of the back thrust than fore thrust. The pop up forms the ramp of the fourth main fault, F_4B.

Step 7 - 48% contraction

Side A (Fig. 5.17-7): The back thrust created at 40% contraction developed to become a pop up structure which now is forming the fifth main fault, F_5A, close to the stable wall. This fault is much larger than the other faults. Another back thrust with a small displacement is developed in the hanging wall of F_5A.

Side B (Fig. 5.18-7): F_4B has developed a displacement of 7 cm and a dip angle of 31°. F_4B is larger than all the other faults in this experiment. A minor fault is formed in the upper reference layer in the hanging wall of F_4B.

Step 8 - 60% contraction

Side A (Fig. 5.17-8): F_5A has propagated forward and has at this stage a displacement of 10 cm and a dip of 34°. Two vertical fractures are formed at the top of the pop up structure. Another main fault, F_6A, was formed after 58% contraction

and developed from the plaster/barite boundary close to the stable wall, with a dip of 37° and a displacement of 5 cm.

Side B (Fig. 5.18-8): F_4B has developed a maximum displacement of 12 cm. A fifth main fault, F_5B was formed close to the stable wall after 52% contraction. The fault has two small back thrusts in the hanging wall.

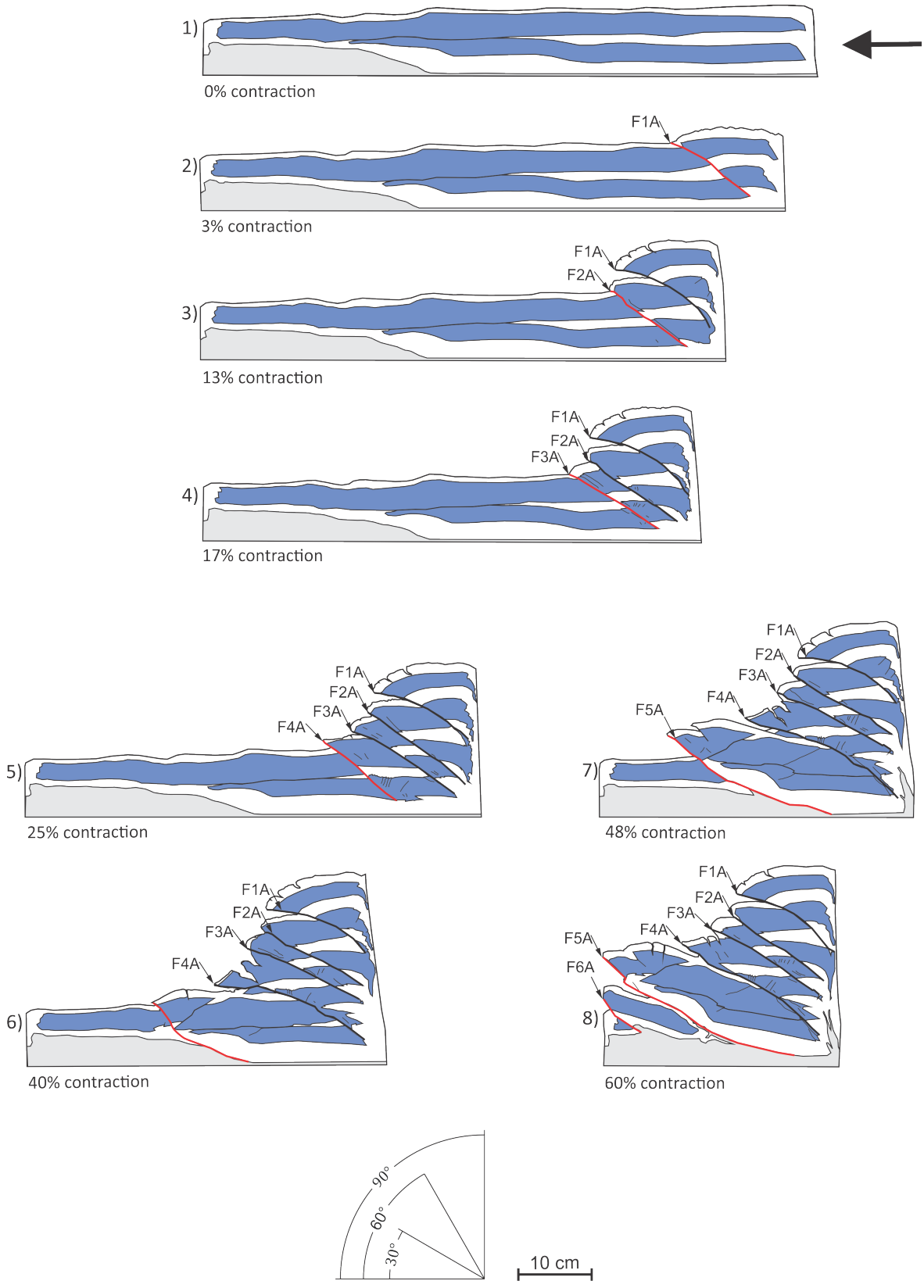

Fig. 5.17: Step-by-step development of experiment 45-14, side A

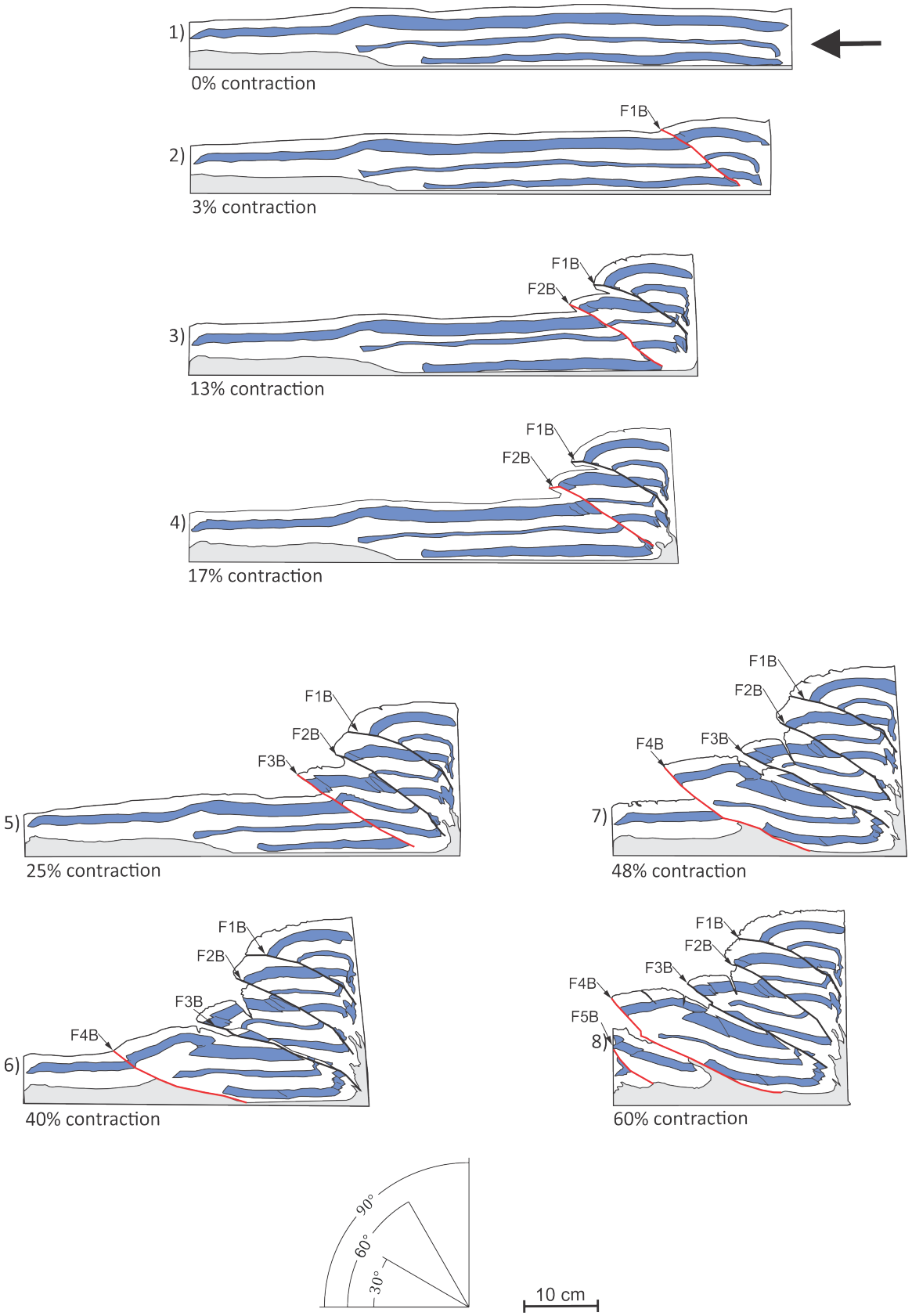

Fig. 5.18: Step-by-step development of experiment 45-14, side B

Summary

The total contraction in this experiment was 60% a low barite ramp with 20° inclination was placed on the foreland side of the box. A presentation of active faults during the experiment of side A and B are presented in figure 5.19 and a photo of the final result is shown in figure 5.20. Six main faults were formed on side A, while 5 main faults were formed on side B. Generally, the faults had increasing active periods with increasing amount of contraction. An exception is the last faults formed on each side. Comparing side A and B at step 4, one find that during the same amount of contraction, side A has developed 3 main faults, while side B still only have 2 main faults. Developments of the subsequent faults are more alike. Both sides produced one fault that is larger both in size and displacement (F_5A and F_4B), which both formed after the formation of a pop up structure. The large faults are formed close to the barite ramp. Both sides also form a smaller fault during the last few percent of shortening (F_6A and F_5B).

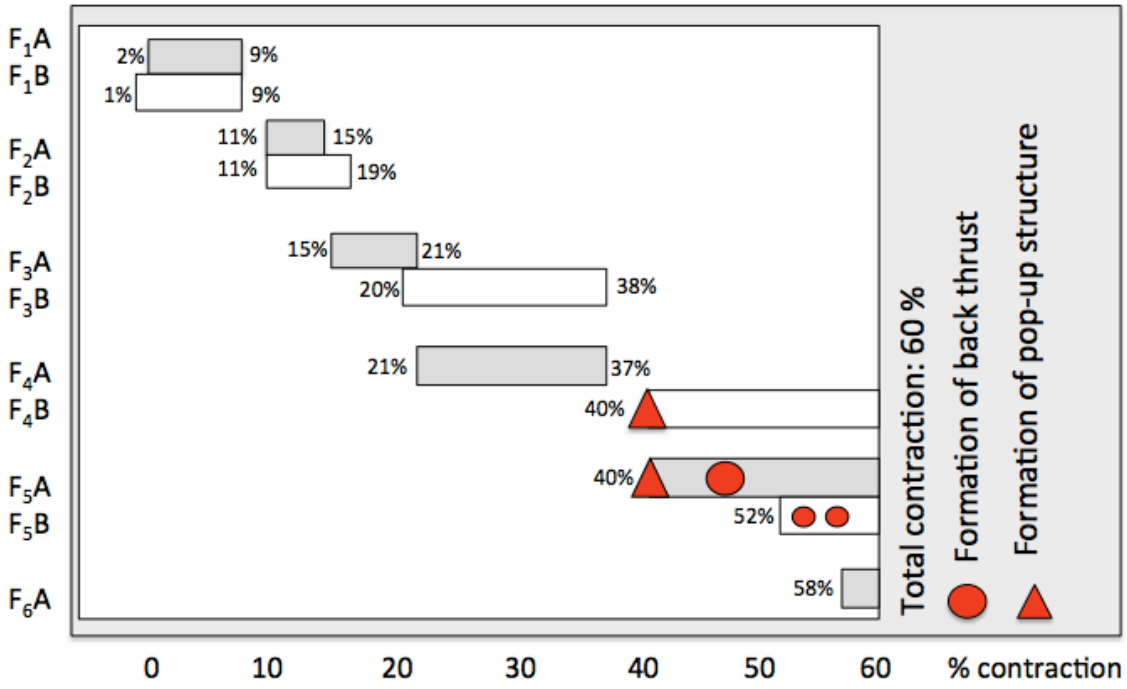

Fig. 5.19: Active faults in experiment 45-14. Fault number and side (A or B) of formation are stated at the vertical axis and amount (%) contraction is stated at the horizontal axis. A pop up was formed prior to the formation of F_4B and F_5A.

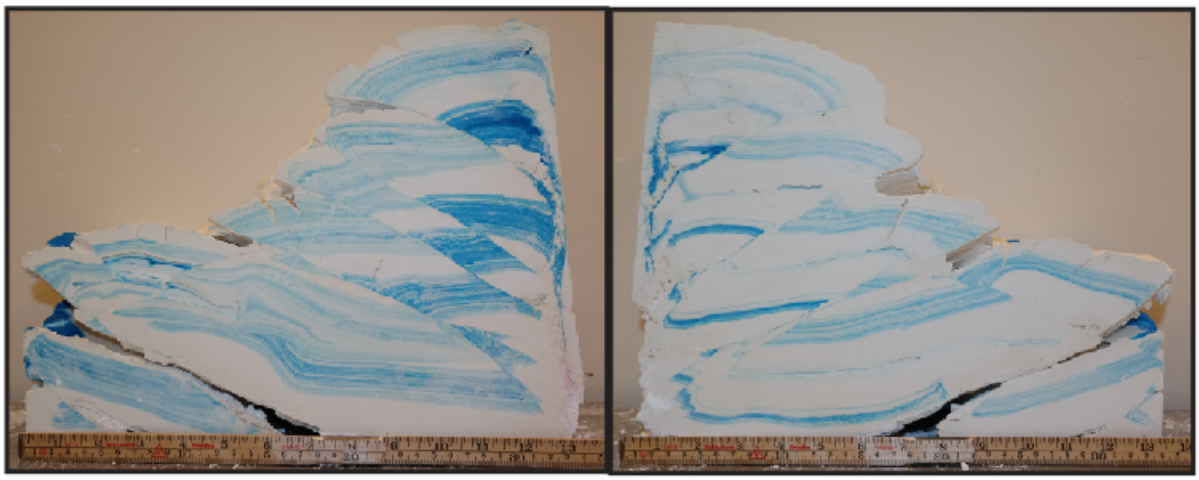

Fig. 5.20: Photograph of the final result for experiment 45-14, side A (left) and B (right).

5.7 Experiment 48-14

The stepwise development of deformation throughout the experiment can be followed in figure 5.21 and 5.22.

Table 5.6: Experimental data for experiment 48-14.

Date	04.12.14
Plaster/water ratio	10 L plaster/6 L water
Experimental conditions	Horizontal basement, 0.2 cm barite
Experimental box	Wide (14 cm width)
Start length	83 cm
End length	28 cm
Start height	8 cm
End height	27 cm
Note	Same experimental set-up as 44-14

Step 2 - 6% contraction

Side A (Fig. 5.21-2): The first main fault, F_1A, is formed in the lower reference layer with a 35° dip towards the moving wall. Prior to this first fault formation the plaster deformed in a ductile manner to the shortening, as can be observed by the folded hanging wall. In the lower reference layer in the hanging wall, there is a formation of small reverse faults.

Side B (Fig. 5.22-2): The first main fault, F_1B, is initiated after 3% contraction in the lowermost reference layer and has propagated through the entire reference layer after 6% contraction. F_1B is formed with a dip of approximately 30° towards the moving wall. Prior to fault formation, ductile deformation is accommodating the plaster, as seen on side A.

Step 3 - 14% contraction

Side A (Fig. 5.21-3): F_1A has developed a displacement of approximately 5 cm in the lower reference layer and is no longer active. The fault plane of F_1A appears to have

been divided in two. The division starts in the middle of the fault plane and the fault reaches the surface in two different places. In addition, an almost vertical fault has been formed close to the moving wall in the lower reference layer. A second main fault, F_2A, is formed and propagates from the lower reference layer. F_2A has a dip of 26° towards the moving wall and minor synthetic faults have formed in the hanging wall in the top reference layer. A small reverse fault has formed in the lower reference layer in the footwall of F_2A, with a dip of 46° towards the moving wall.

Side B (Fig. 5.22-3): Some of the reference layer in F_1B has been smeared between the fault plane. F_1B has a displacement of 6 cm in the lowermost reference layer and is no longer active. A second main fault, F_2B, is well developed, with a dip of 36° and a displacement of approximately 3 cm, decreasing as the fault reaches the surface.

Step 4 - 27% contraction

Side A (Fig. 5.21-4): F_1A has a higher dip of 37° as a response of the constant shortening and vertical build up. F_2A is no longer active. The minor fault that formed in the footwall of F_2A was not able to reach the surface before the third main fault, F_3A, was formed. F_3A initiated in the lower reference layer has a dip of 25°.

Side B (Fig. 5.22-4): F_2B has developed a displacement of 7 cm and is no longer active. A third main fault is established with a similar dip as F_1B and F_2B. A low angle minor fault has been formed in the hanging wall of F_3B.

Step 5 - 39% contraction

Side A (Fig. 5.21-5): F_3A is no longer active. A fourth main fault is initiated close to the plaster/barite boundary with a dip of 34°. A small pop up structure with shallow dip at both sides is formed in the top reference layer as a part of the initiation of the fourth main fault, F_4A. Initiation of a minor fault is observed with a dip of 25° in the lower reference layer in the hanging wall of F_4A.

Side B (Fig. 5.22-5): F_3B has developed a displacement of 10 cm and is no longer active. A fourth main fault, F_4B, is formed with a displacement of 2 cm and a dip of 30°. The fault block has a complex structure, with minor faults in the top of the reference layer and back thrusts in the lower part of the reference layer.

Step 6 - 48% contraction

Side A (Fig. 5.21-6): The small thrust that was initiated in the hanging wall of F_4A has grown to become a small out-of-the-sequence thrust with 21° dip and propagates over the base of F_4A, leading to a deviation of the fault and the lowermost part of F_4A becomes inactive.

Side B (Fig. 5.22-6): F_4B is still active and has developed a displacement of 9 cm and starts to bend towards the stable wall.

Step 7 - 57% contraction

Side A (Fig. 5.21-7): F_4A has developed a displacement of 11 cm and has propagated up the ramp and bends over the underlying layers. The lower part of F_4A has been divided into two small thrusts. Fault block 4 has developed vertical fractures at the top. A pop up structure is formed in front of the plaster layers closer to the stable wall, which starts the formation of another main fault, F_5A.

Side B (Fig. 5.22-7): F_4B progress forward, with the minor faults at the top reference layer and back thrusts in the lower reference layer, and creates a displacement of 15 cm. A large pop up structure is formed in the plaster ahead of the youngest fault with only 0.5 cm displacement on each side.

Step 8 - 66% contraction

Side A (Fig. 5.21-8): At the end of the experiment, only F_5A is active. The pop up structure that was formed at 57% contraction is only showing by a back thrust at F_5A.

Side B (Fig. 5.22-8): The pop up structure has developed to become a fifth main fault, F_5B. This fault has three listric back thrusts with only mm displacements found in the hanging wall. Some of the fault is smeared between the fault plane, creating a small lens structure. When the contraction stops, F_5B has developed a displacement of 8 cm and small vertical fractures have started to develop in both F_4B and F_5B from the extension during the bending.

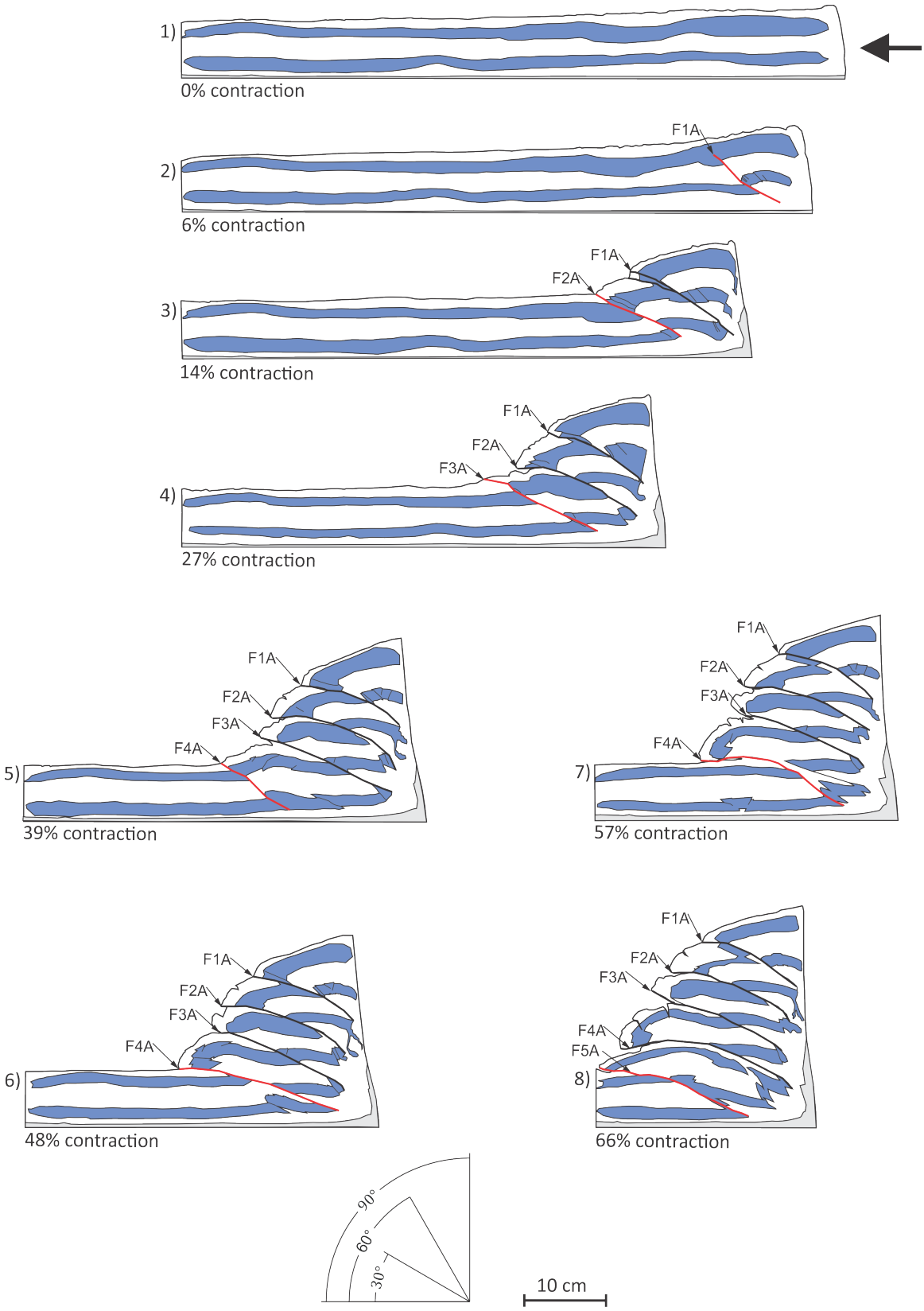

Fig. 5.21: Step-by-step development of experiment 48-14, side A

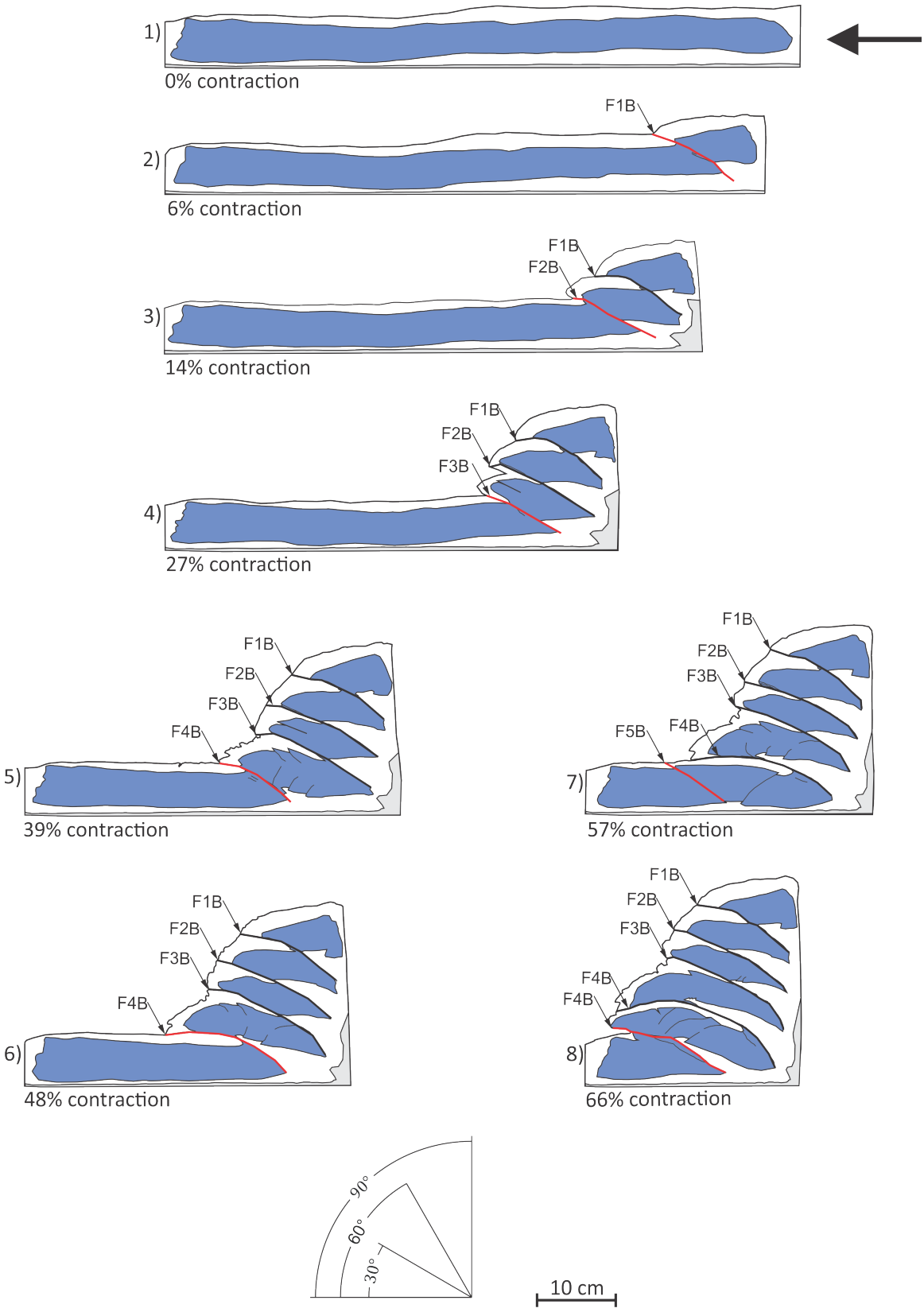

Fig. 5.22: Step-by-step development of experiment 48-14, side B

Summary

The total contraction in this experiment was 66% and a presentation of the active faults at side A and B are shown in figure 5.23. A photo of the final result is shown in figure 5.24. Both sides shows similar fault developments and formed 5 faults on each side. F1 is formed after 6% contraction and becomes inactive after 12-14% contraction. F2 is formed after 13-14% and becomes inactive after 24-28%. F3 is formed after 24.5-26% and becomes inactive after 37% contraction. Side A creates a small pop up structure initiated and only present in the upper reference layer before the initiation of F_4A. As shortening proceeds, F_4A becomes inactive due to the formation of an out-of-the-sequence thrust, which was formed in the lower reference layer. This structure is not observed at side B, where the top reference layer is influenced by small thrust faults and the lowermost reference layer is influenced by small back-thrusts. F4 is formed at 38-40% contraction and becomes inactive at 53-54% and F5 is formed at 55% contraction and is active until the end of the experiment. Pop ups were formed prior to the formation of the last fault on each side.

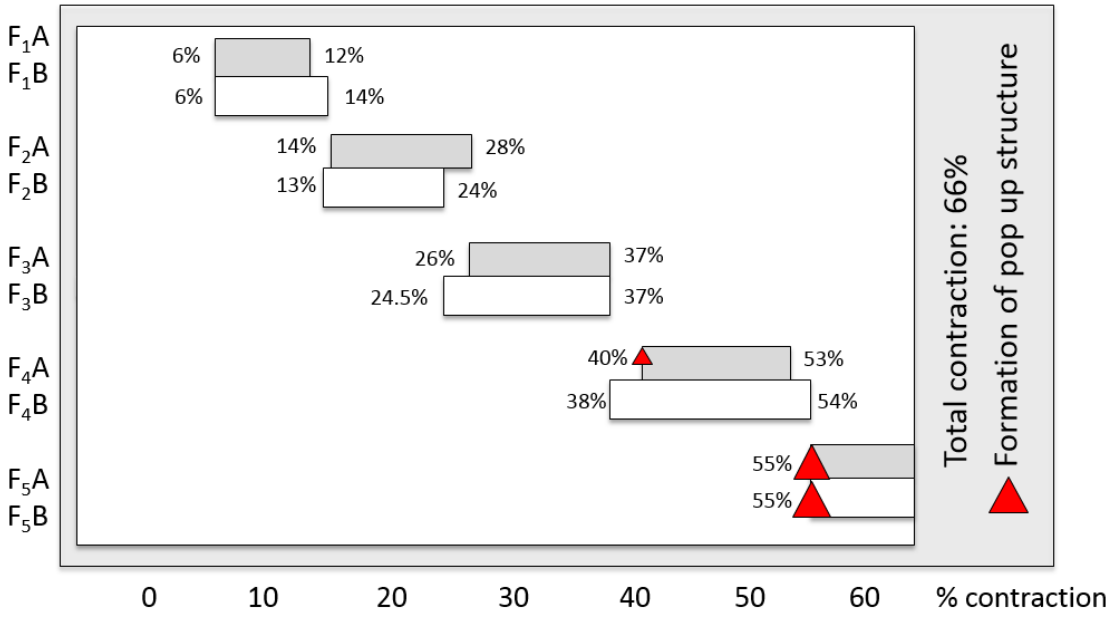

Fig. 5.23: Active faults in experiment 48-14. Fault number and side (A or B) of formation are stated at the vertical axis and amount (%) contraction is stated at the horizontal axis. A small pop up was formed prior to the formation of F_4A and larger pop ups formed prior to the formation of F5 on both sides.

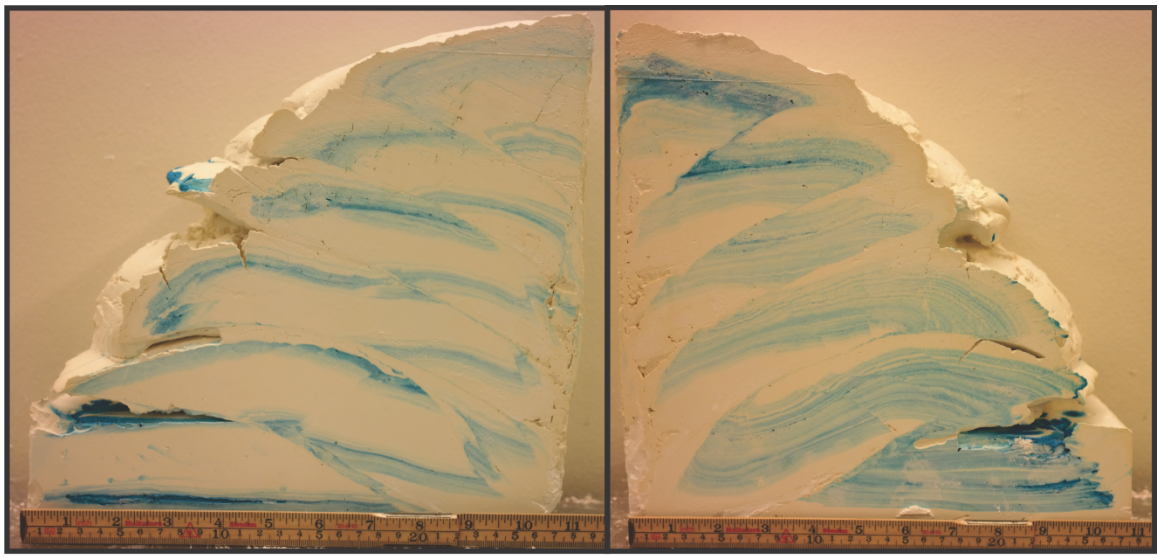

Fig. 5.24: Photograph of the final result for experiment 48-14, side A (left) and B (right).

5.8 Fault development in the horizontal plane

A three dimensional view of the experiments give a better understanding of how thrusts develop in the horizontal plane. The experiments were photographed from above to document the horizontal development (Fig. 5.25) and link the horizontal and vertical perspective of thrust propagation. The analysis is done with photographs of experiment 44-14.

Step A (Fig. 5.25A) present the plaster prior to shortening and show a horizontal surface. This step is equivalent of step A from the description of experiment 44-14 (subchapter 5.5). Step B (Fig. 5.25B) show the development after 13% contraction, and indicate formation of one main fault. Several segments are formed ahead of the main fault. The segments seem to be initiated at different sites in the plaster and interlink to become longer prior to main fault development. Comparing step B (Fig. 5.25B) with the equivalent shortening percent in the step-by step description (Fig. 5.13-3 and 5.14-3), it is apparent that side B (vertical view) has formed two main faults, while side A (vertical view) only has formed one main fault. This indicates that the main fault has propagated differently and not yet reached side A which could also indicate that the fault nucleation centre is relatively closer to side B than

side A. The same pattern is seen at 25% contraction (Fig. 5.25C and D). Several segments are formed at the right side of the box, and are believed to be a result of interaction with the moving wall. The faults are developing a curved shape as they propagate toward the stable wall. Small open fractures (green, Fig. 5.25) perpendicular to the transport direction have formed close to the moving wall and is observed to be a result of the bending of the hanging wall which leads to extension after passing a ramp.

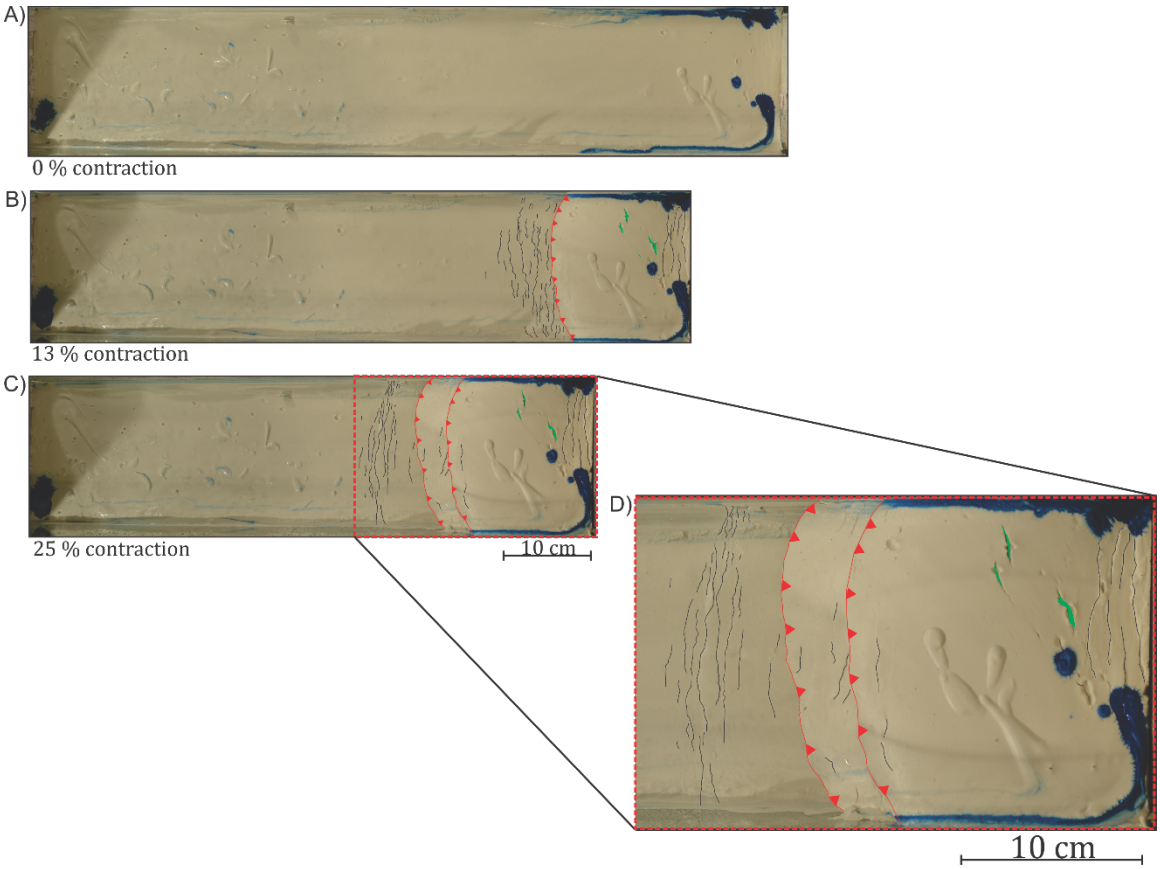

Fig. 5.25: Fault development in the horizontal plane. A) Prior to contraction, B) after 13% contraction, C) after 25% contraction and D) close-up of 25% contraction where two main faults have developed and segment linkage is apparent ahead of the faults. Green illustrates fractures, black represent propagating segments and red illustrates full developed thrust faults.

CHAPTER 6 – FAULT DEVELOPMENT AND CHARACTERISTICS

6.1 Introduction

The aim of this chapter is to present how the contractional faults developed in the plaster experiments. An overall description of how the main faults developed, their fault dip angles, displacement evolution and fault spacing generation will be given. Further more a detailed description of wedge height and wedge angle, fault related folding and minor faults will be given. Finally, a full restoration of experiment 12-14 will be presented.

Table 6.1: General overview of the experiments. The degree of viscosity is determined based on observations, fault initiation and plaster/water ratio.

Experiments	Plaster/ water ratio (L)	First main fault initiation (%)	Viscosity (1 - 3*)	Experiment duration (Time)
12-14	4.5/4	1.5 - 3 %	2	36 sec.
15-14	4/4	5 - 7 %	1	18 sec.
27-14	4.2/4	5 - 7 %	2	43 sec.
44-14	10/6	2 %	3	28 sec.
45-14	10/6	1 - 2 %	3	37 sec.
48-14	10/6	6 %	2	35 sec.

*Viscosity: 1 = low, 2 = medium, 3 = high

6.2 Main fault activity

In the experiments, the main faults are cutting through the entire plaster layer and appear as discontinuities. Most of the faults are formed in an in-sequence fashion, where new faults form progressively in the foreland direction leaving the previous faults inactive. A graphical assembly of the six experiments is presented in figure 6.1. Before fault initiation, contraction is accommodated through folding/layer parallel shortening until reaching a critical point and the fault initiates. The average amount contraction for F1 to form is 3.9%, F2 is formed after an average of 11.8% contraction, F3 formed after average 20.8% contraction, F4 formed after 37.7%, F5 after average 49.6% and F6 after average 56% contraction. It is therefore between

6.7% and 16.9% shortening of the experimental box between each new fault formation.

In most of the experiments, only one main fault is active at a certain time, meaning that one fault is accommodating all contraction (discarding contraction accommodated from folds, minor faults and layer parallel shortening). Some limited overlapping fault activity is observed (see for example 48-14, side A, F2-F3) as the subsequent fault is initiated. However in most cases, the previous faults are active for only a limited time before the fault becomes inactive. At the end of experiments, faults are active for a longer period and some models show an overlapping tendency of the last two faults, as is apparent in experiment 12-14.

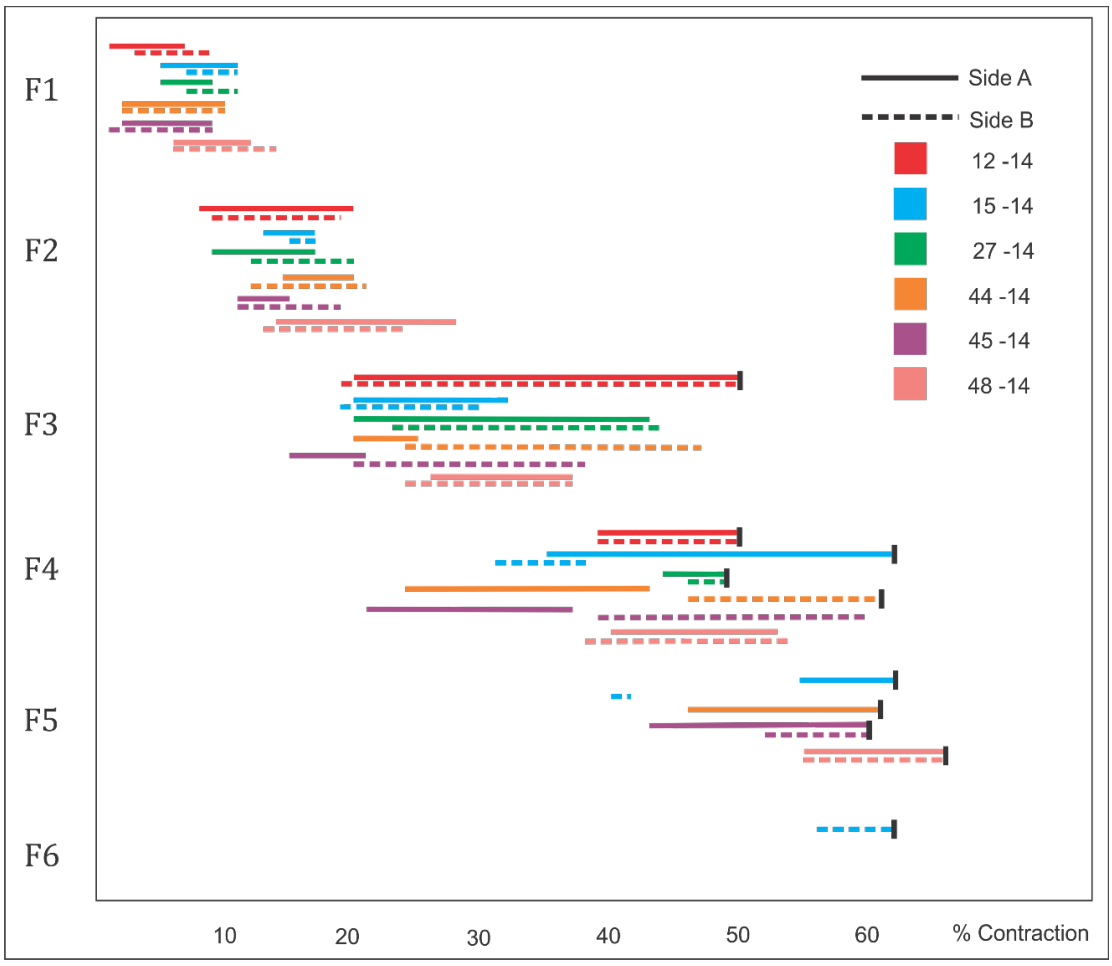

Fig. 6.1: Assembly of main faults formed in experiments 12-14, 15-14, 27-14, 44-14, 45-14 and 48-14. Fault number is stated at the vertical axis, amount (%) contraction is stated at the horizontal axis. Straight and stippled lines represent side A and side B respectively, which are colour coded according to experiment number. The short, black lines represent the end of the experiments.

6.3 Fault dip

The fault dip angles in the experiments show a trend of becoming steeper from the time they were initiated towards the end (Fig. 6.2). Consequently, the older faults are often steeper than the younger faults. However, some of the latest faults developed are initiated with a steep angle and does not increase dip from start to the end (e.g. 4A in experiment 12-14). Experiments 44-14, 45-14 and 48-14 have ramps that are squeezed against the moving wall with increasing contraction, which creates an unrealistic high wedge angle. This is clear from figure 6.2 were the experiments have an averagely larger dip development (red vs. blue stippled box).

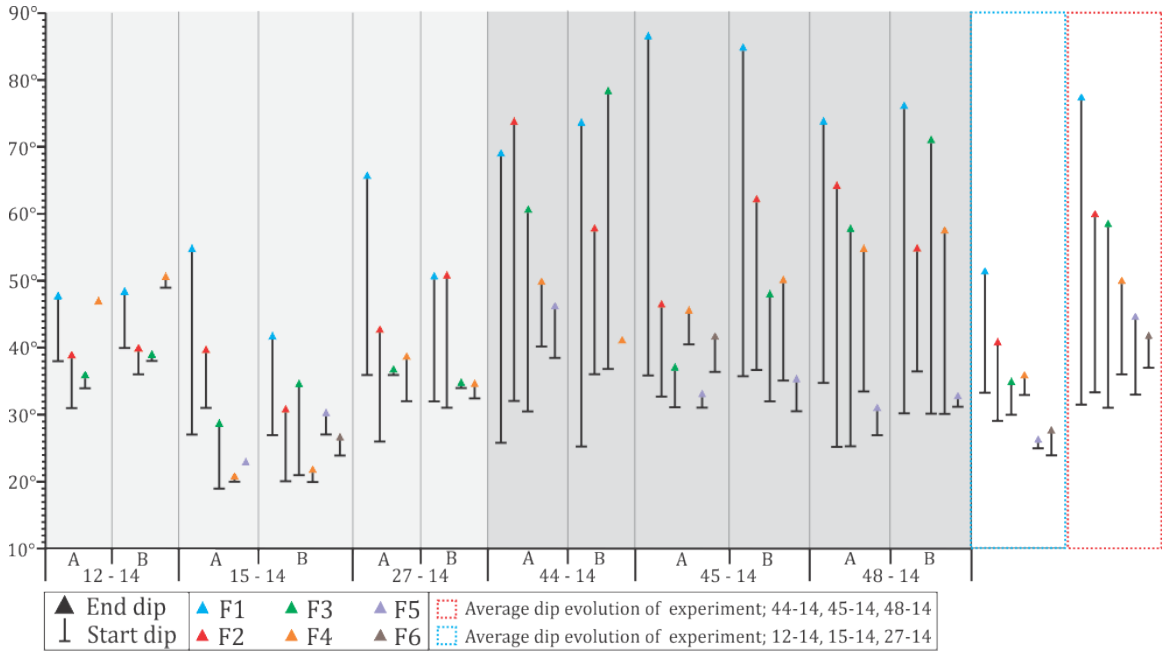

Fig 6.2: Fault initiation dip angles and dip angles at the end of experiment measured along the ramp. Letters A and B represents sides of development. Average dip evolution is marked with stippled lines and are found to be higher for experiment 44-14, 45-14 and 48-14. Experiments with 5-6 faults will increase the average since more faults are formed and leads to higher rotation of the oldest faults. Data for the graph is found in Appendix B.

The first and second main fault has an average initiation angle of 32°. The third has an average of 29°, the fourth average of 35° and the fifth 32°. A sixth main fault is only developed in two of the experiments (15-14 and 45-14) and had an average initiation angle of 30.5°.

The faults are in most cases forming flat-ramp-flat geometries, causing the fault planes to be curved to curvy-planer as it changes from low to high dip as the

fault propagate toward the surface. The fault planes also changes from high to low dip angle after passing a ramp, and bends towards the foreland.

6.4 Fault displacement

By studying Table 8, a general trend is observed where the first faults create small displacements and does not develop to become large faults. Fault displacement increases with progressive shortening, which leads to the formation of high displacement faults towards the end of the experiments. The oldest faults have approximately 2-9 cm maximum displacement, while the younger faults develop a maximum displacement of up to 20 cm. From the step-by-step development described in Chapter 5, the rate of displacements along the fault are observed to decrease after formation of a new fault. The displacement is then moved to the subsequent fault. At the end of the experiments, some of the younger faults have small displacement as the faults approach the stable wall. A change in displacement along the individual faults is evident, and maximum displacement is located in the lower part of the fault, closest to the barite.

Table 6.2: Maximum fault displacement.

Experiment nr.	Fault nr.	Maximum fault displacement, side A (cm)	Maximum fault displacement, side B (cm)
12-14	F1	5	5
	F2	8	8
	F3	16	14
	F4	4	2.5
15-14	F1	2	2
	F2	3	3
	F3	9	10
	F4	20	8
	F5	4	6
	F6	-	5
27-14	F1	2	2.5
	F2	5	5
	F3	14.5	11
	F4	3	3
44-14	F1	8	7
	F2	4	6
	F3	5	13
	F4	9	12
	F5	12	3
45-14	F1	8	7
	F2	4	6
	F3	5	13
	F4	9	12
	F5	12	3
	F6	5	-
48-14	F1	5	6
	F2	9	7
	F3	11	10
	F4	15	19
	F5	19	8

6.5 Fault spacing

The kinematics of imbricates spacing is studied (Fig. 6.3) and it is found that the amount of contraction needed for the first fault to form varies between the experiments. The less viscous experiment (15-14) had the latest fault initiation whereas the more viscous experiment (44-14 and 45-14) had very early fault initiation. Figure 6.3 display that in most experiments, the imbricates exhibited increased spacing with progressive shortening. However, some experiments produced thrusts more closely spaced towards the end. As the spacing of imbricates increased towards the stable wall, the rate of imbricates decreased (Fig. 6.4). The lines representing rate of nucleation, show a general trend of becoming less steep with increasing time, which indicates a progressively larger time gap between thrust nucleation. However, this pattern is not clear in all the experiments, as some experiments continued to have a steep gradient (e.g. experiment 15-14).

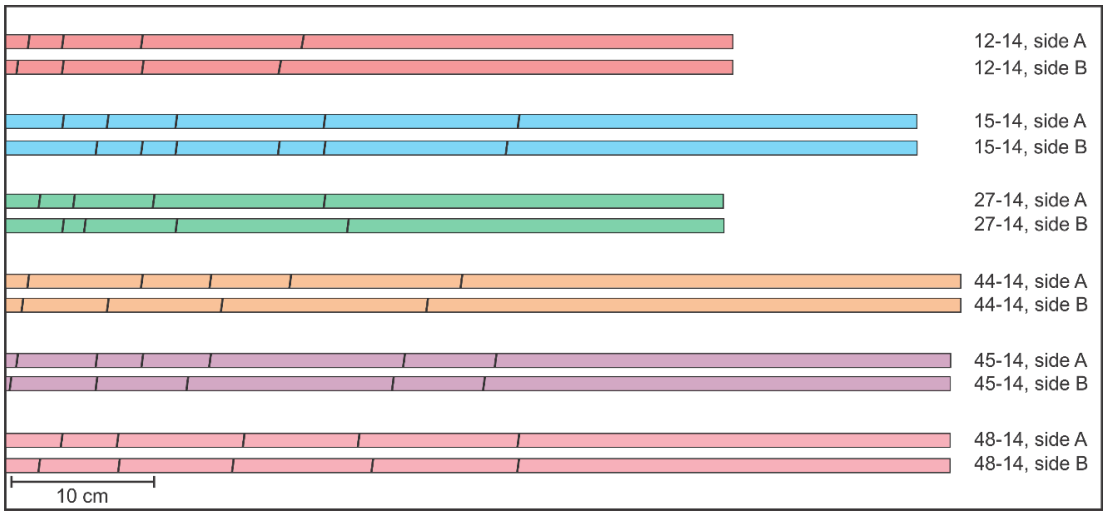

Fig. 6.3: Initial spacing between nucleating imbricates (small black lines). Coloured bars present total length of the experimental box prior to shortening.

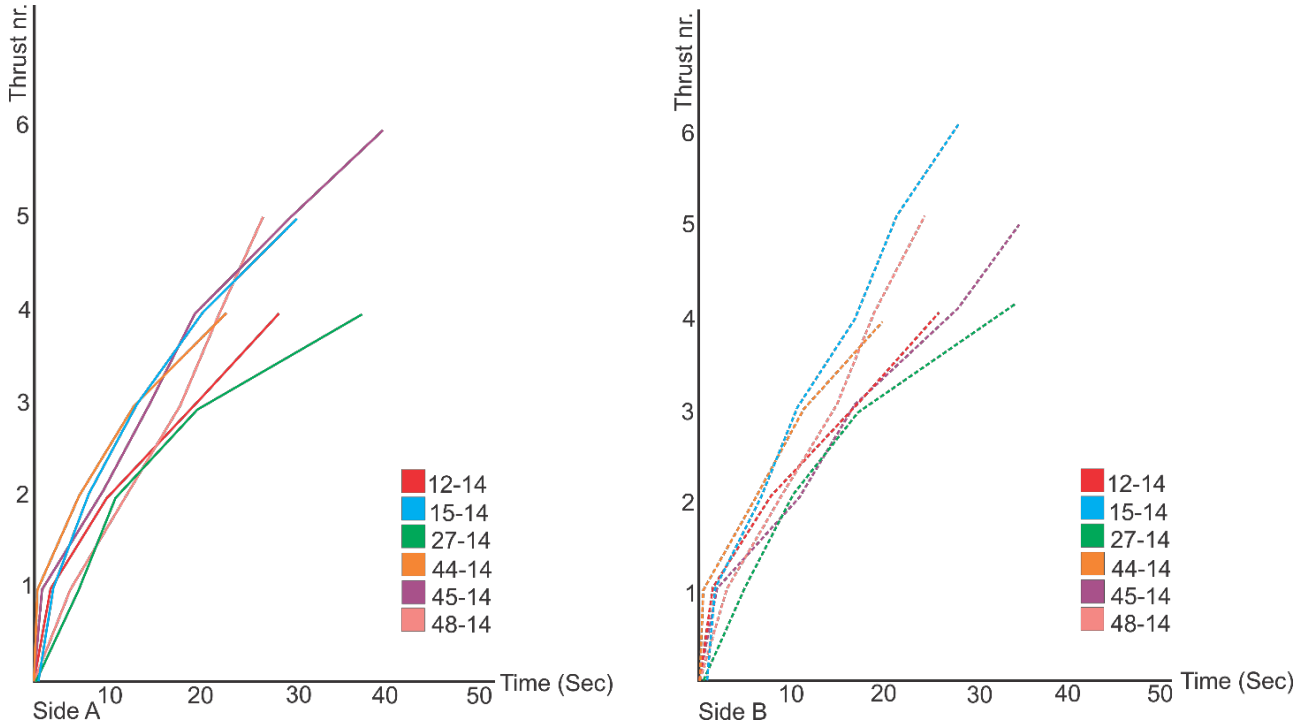

Fig. 6.4: Nucleation rate of the same imbricates presented in Fig. 6.3. The graph shows a trend of becoming less steep with increasing time.

6.6 Wedge height and geometry

The shape of the wedge created in the different experiments varies. However, a common feature of thinning towards the stable wall is observed in all the models, with exception of 44-14. A graphical presentation of the growing wedge height with contraction is shown in Graph 6.1. The experiments with lowest wedge height were 15-14 and 27-14, which had less amount of plaster and were produced in a narrow experimental box. These wedges are almost half the height when compared to some other experiments (e.g. 15-14 compared with 44-14) and are building more horizontally instead of vertically. Graph 6.1 show that 12-14, 44-14, 45-14 and 48-14 had similar development of wedge height. They all produced 4-5 main faults and were contracted 50-60%.

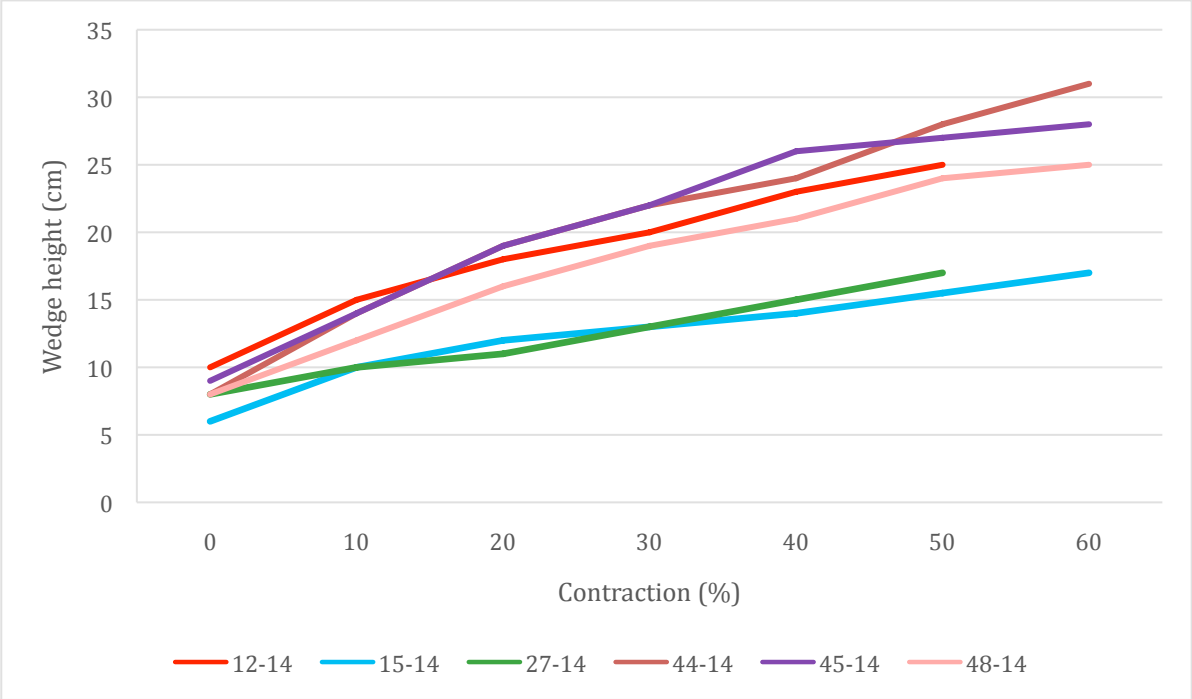

Graph 6.1: Wedge height vs. contraction for the six experiments.

The wedge geometry is analysed by looking at the wedge angle (surface slope) throughout the experiments (Graph 6.2). The more ductile experiment 15-14 had the lowest wedge angle, which ranged between 16-20°. Experiment 27-14 also had quite low wedge angle, however the experiment was shorter than the other experiments. Wedge angle of the most brittle experiment 44-14 was found to be difficult to measure as the fault blocks formed large irregular shapes on top of the model. However, an overall trend was measured. All six experiments formed a wedge that reached a maximum wedge angle at a certain shortening range. After reaching this maximum height, the wedge angle decreased, before again increasing or stabilising at a constant wedge angle.

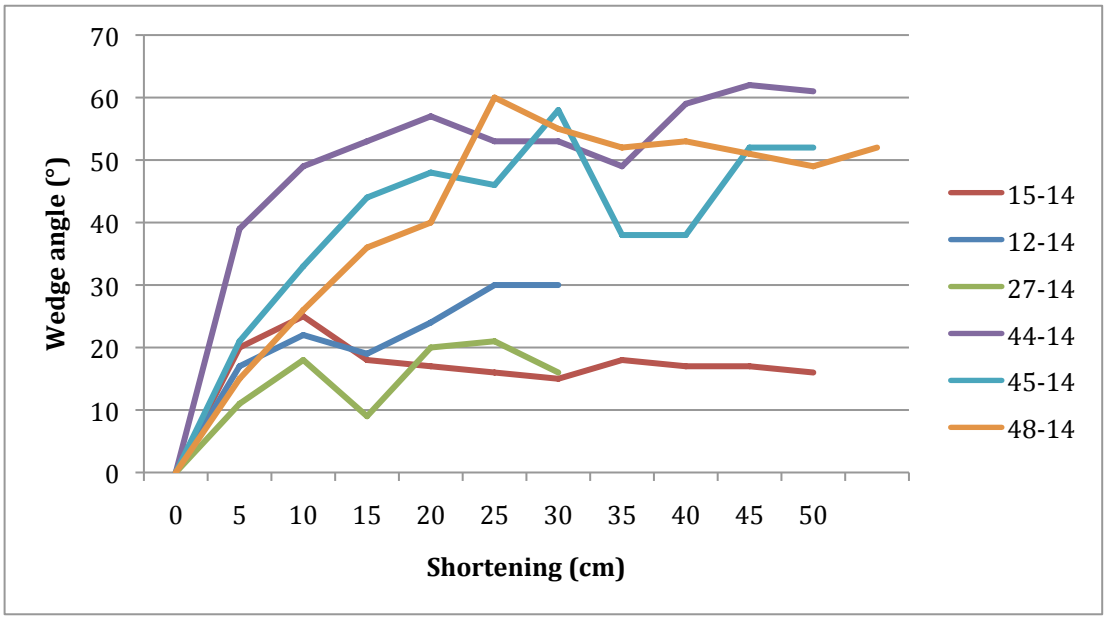

Graph 6.2: Wedge angle for the six experiments. Shortening is presented at the horizontal axis while wedge angle is presented at the vertical axis.

6.7 Fault related folding

Folding is observed in relation to faults as described in Chapter 5. Fault-propagation folding, in which folding happens in advance of a propagating fault tip, is the most abundant fold type observed in the models and is seen in models; 27-14, 44-14, 45-14 and 48-14 (e.g. Fig. 6.5A). Fault bend folds occur in the middle and later part of the thin and less viscous experiment 15-14 (Fig. 6.5B) and they are not present in the more brittle experiments.

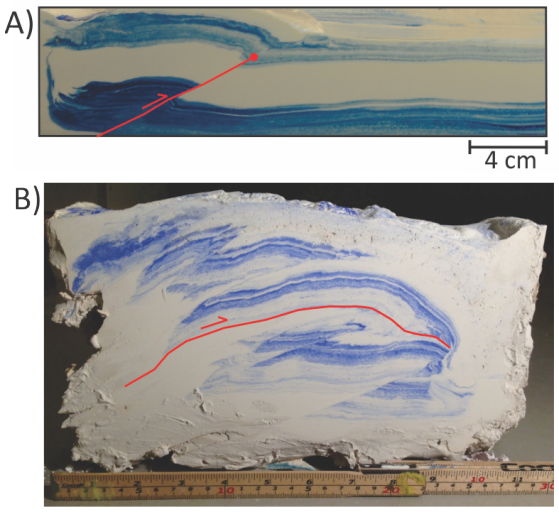

Fig. 6.5: Examples of folds produced in the experiments. A) Fault-propagation fold in experiment 44-14 and B) fault-bend fold in experiment 27-14.

6.8 Minor faults

In the models, minor faults often appear in association with main faults (Fig. 6.6), as synthetic or antithetic faults. The synthetic minor faults are observed to form in the footwall of a main fault, which often develop a higher dip than the main fault. This is observed for instance in experiment 44-14, side A after 7% contraction (Fig. 6.6A). Synthetic minor faults are also observed to form ahead of a main fault, close to the fault tip in the hanging wall of the propagating main fault, and can be observed in experiment 45-14, side B after 25% contraction (Fig. 6.6B). In the experiments with more firm plaster, a group of antithetic minor faults are commonly formed before main fault formation. This can be observed for instance in experiment 44-14, side A after 12% contraction (Fig. 6.6C). Antithetic faults also appear in the hanging wall of an active thrust (Fig. 6.6D), often in associated with pop up structures.

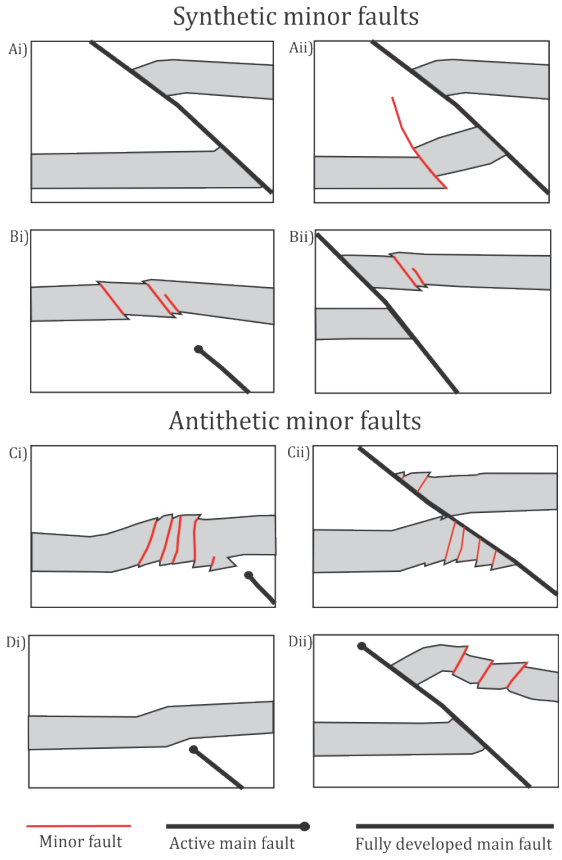

Fig. 6.6: Synthetic and antithetic faults formed in the experiments in relation to main faults. Transport direction is towards the left in all four examples. Ai-ii: The development of a minor synthetic fault in the footwall of the main fault. Bi-ii: A synthetic fault formed ahead of a main fault. Ci-ii: Small antithetic faults formed prior to formation of a main fault, which cuts through the antithetic faults. Di-ii) Small antithetic back thrusts formed in the hanging wall of an active thrust.

The formations of pop up structures are in most cases a primary event related to the development of a main fault. The pop ups initiated from the bottom of the box, penetrated the surface and formed immediately in front of the previous fault. The formation starts with a low displacement and a back thrust with a steep dip. The back thrust keeps accommodating the shortening until the fore thrust forms, which has a more shallow dip, and the resulting structure becomes a pop up (Fig. 6.7). Some experiments also form parallel back thrusts as the fore thrust moves up the ramp (Fig. 6.8).

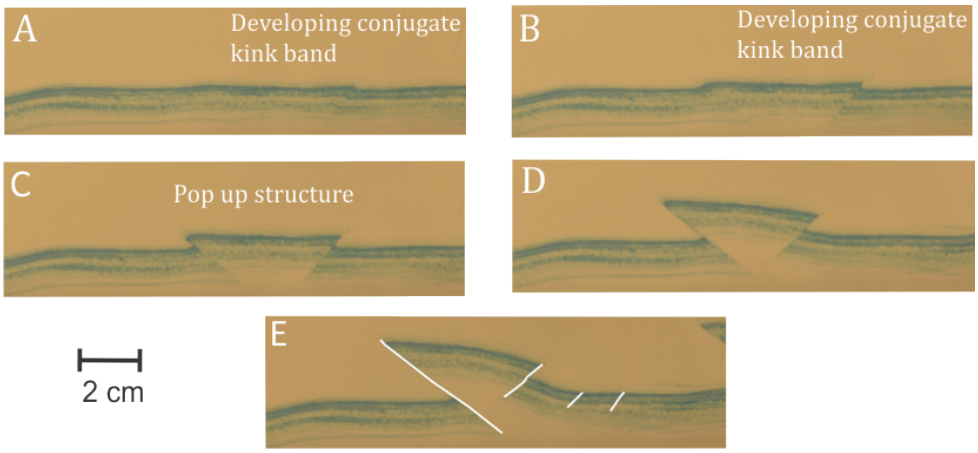

Fig. 6.7: The formation of a pop up structure in experiment 44-14, side A from 35-40% shortening with transport direction towards the left. A)-B) shows development of a conjugate kink band eventually forming a small displacement, high angle back thrust, C) a fore thrust has formed which creates a pop up structure, D)-E) the development of a major fault propagating up the ramp towards the foreland.

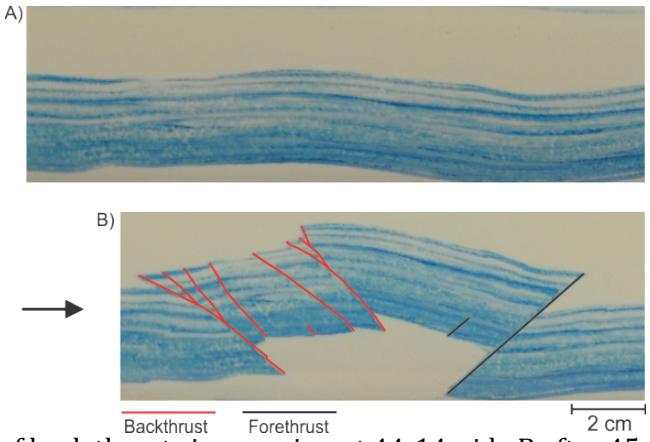

Fig. 6.8: Formation of back thrusts in experiment 44-14, side B after 45-49% contraction. A) Illustrates the plaster layer before contraction whereas B) represents the layer after contraction.

The back thrusts of the pop ups had generally steeper dip than the fore thrusts (Table 6.3) with an average of 10° higher. The exceptions are 12A, which formed during the last few percentages of shortening and had little place to propagate as the fault reached the back wall, and 45A, which formed above a ramp.

Table 6.3: Angle of fore thrusts and back thrusts during the development of a pop up structure. 44A1 refers to the first pop up formed in experiment 44-14 side A and so forth, 44A2 refers to the second pop up formed in experiment 44-14 side A and so forth.

Experiment nr.	Fore thrust angle (°)	Back thrust angle (°)
12A	45	45
27A	24	46
44A1	39	48
44A2	45	60
44B1	37	43
44B2	41	47
45A	35	35
45B	35	46
48A	26	56
48B	32	43
Average	**36.9**	**46.9**

Irregularities also developed along the fault plane in the form of upward splaying faults (Fig. 6.9), or formation of small lenses between the hanging wall and the footwall. Lenses developed as a result of ramp collapse during climb of a fault.

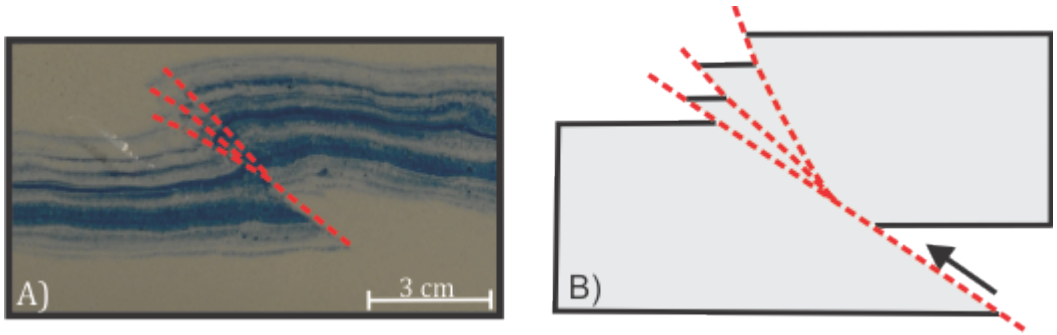

Fig. 6.9: Upward-splaying fault. A) In experiment 27-14 and B) theoretical illustration.

6.9 Restoration of experiment 12-14

After 15% contraction (Fig. 6.10), two main faults have developed (F1 and F2). The reference layers are close to horizontal near to the moving wall (right). However, approaching the fault planes, ductile deformation becomes more apparent and the reference layers become increasingly sheared. The best result for restoration is found with a rotation of 2° for fault block 1 and a shearing angle of 23° (light blue area in Fig. 6.10). Approaching the fault plane, shear angle increases with about 28° (dark blue area in Fig. 6.10). For fault block 2, the reference layers are sheared with 18° (light grey area in Fig. 6.10), increasing to about 38 degrees close to the fault plane (dark grey are in Fig. 6.10). This indicates that the shear angle is not constant through the experiment, and varies according to the distance from the fault plane (higher shear angle close to the fault plane). Layer parallel shortening (LPS) has been measured to be 2% for both reference layer A (red) and B (blue).

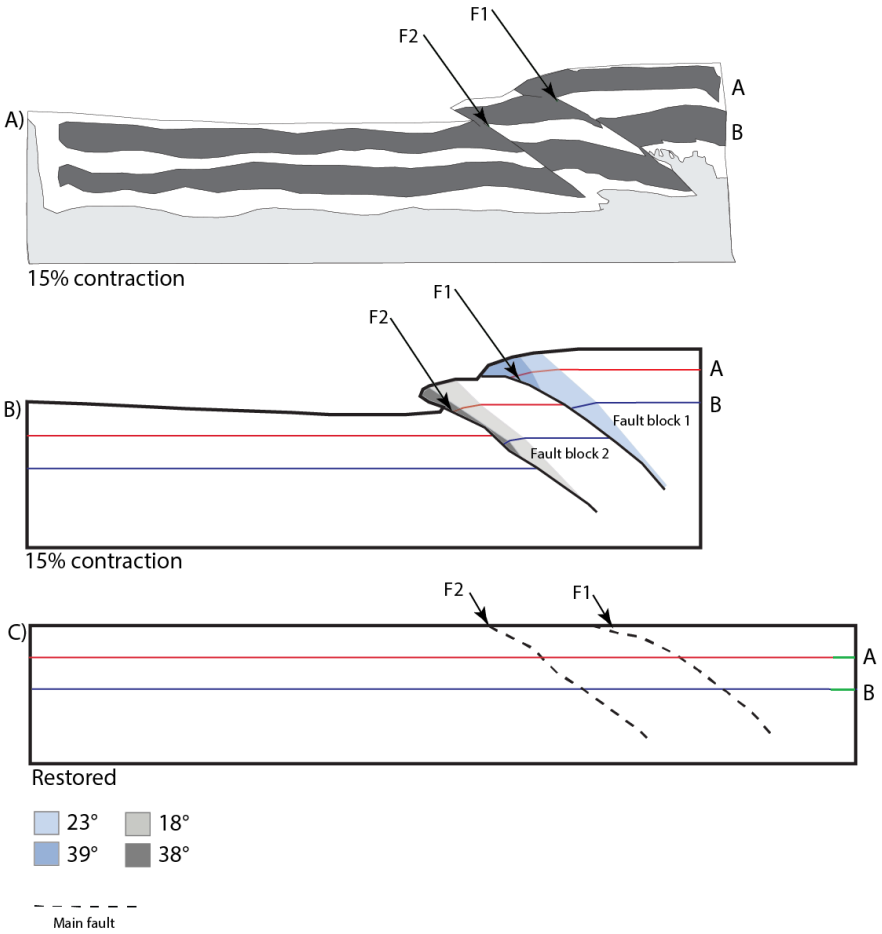

Fig. 6.10: Restored illustration of experiment 12-14 after 15% shortening. A) Model redrawn from photo taken during experiment. B) Two reference levels are labelled A (red) and B (blue). Coloured polygons represent shear angles used for restoration. C) Black dashed lines show the location of faults F1 and F2 at the final stage of restoration. Note that the amount of deformation not accommodated by faults F1 and F2 is interpreted as layer parallel shortening, shown with green line in C).

After 34% contraction (Fig. 6.11), one additional main fault (F3), and a large back thrust are formed in the fault block between F2 and F3 (fault block 3). Fault block 3 has been rotated 6° and the layers are sheared 25° (light pink area in Fig. 6.11). Approaching the fault plane, shearing is higher with additional 20° and forms a total of 45° (dark pink area in Fig. 6.11). Fault block 2 has been rotated 8°. The shearing angle is 29° with additional 37° at the tip of the fault plane, which together creates 66° shearing angle (light and dark grey area in Fig. 6.11). Fault block 1 is rotated 8°. Shearing angle is 27° and additional 27° closer to the fault plane with a total of 54° (light and dark blue area in Fig. 6.11). LPS has been measured to be 4% and 5% for reference layer A (red) and B (blue) respectively.

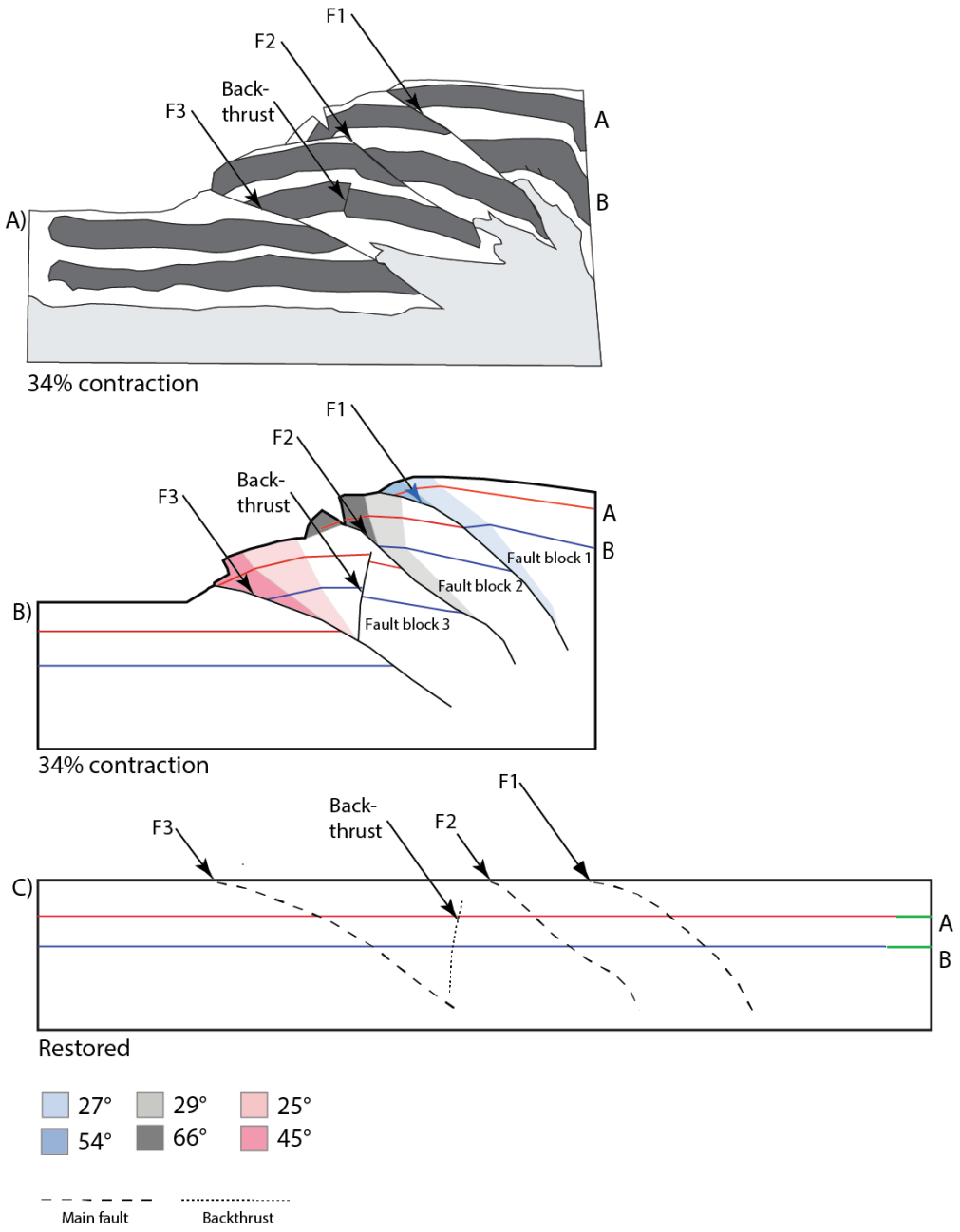

Fig. 6.11: Restored illustration of experiment 12-14 after 34% shortening. A) Model redrawn from photo taken during experiment. B) Two reference levels are labelled A (red) and B (blue). Coloured polygons represent shear angles used for restoration. C) Black dashed lines show the location of faults F1, F2 and F3 at the final stage of restoration. Note that the amount of deformation not accommodated by faults F1-F3 is interpreted as layer parallel shortening, shown with green line in C).

After 50% contraction (Fig. 6.12), one additional main fault (F4), and a large back thrust are formed in the fault block between F3 and F4 (fault block 4). Fault block 4 has been rotated with 6° and only been sheared with approximately 6° close to the

fault plane (light green area in Fig. 6.12). Fault block 3 has been rotated 10°. Shearing angle is 16° and additional 23° closer to the fault plane (light and dark pink area in Fig. 6.12), making a total of 39°. Fault block 2 has rotated 11° and the top reference layer (A) has increasing shearing angles towards the tip with as much as 56° (light and dark grey area in Fig. 6.12). Fault block 1 has been rotated with 14° and shearing angle is 12° (light blue area in Fig. 6.12). Approaching the fault plane, the shearing is higher with a total of 32° (dark blue area in Fig. 6.12). LPS has been measured to be 5% and 6% for reference layer A (red) and B (blue) respectively.

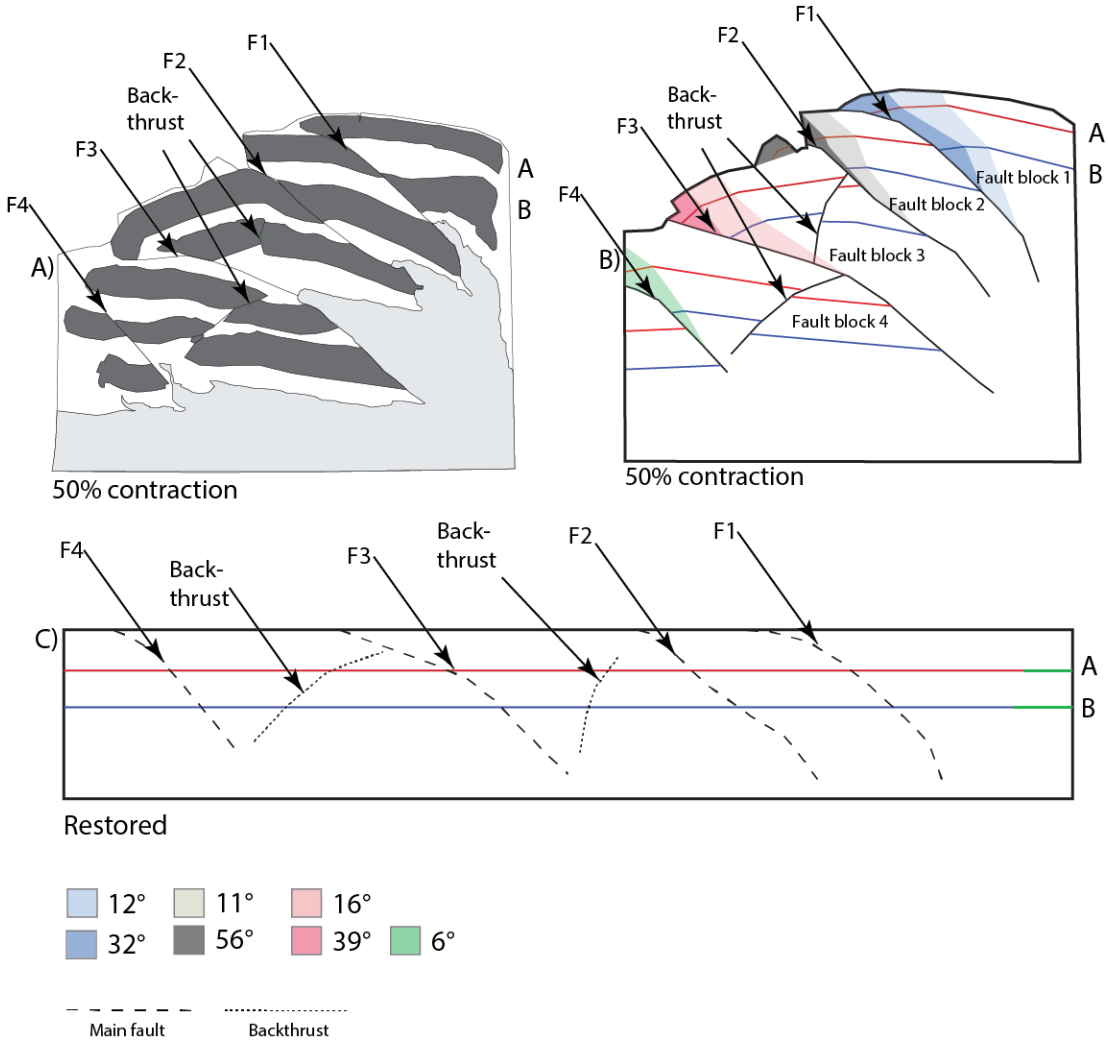

Fig. 6.12: Restored illustration of experiment 12-14 after 15% shortening. A) Model redrawn from photo taken during experiment. B) Two reference levels are labelled A (red) and B (blue). Coloured polygons represent shear angles used for restoration. C) Black dashed lines show the location of faults F1-F4 at the final stage of restoration. Note that the amount of deformation not accommodated by faults F1- F4 is interpreted as layer parallel shortening, shown with green line in C).

Summary

Three different steps (15%, 34% and 50%) of experiment 12-14 are restored. The shearing angles for the different fault blocks vary, however a clear trend is apparent in the hanging wall; shearing angle increase further towards the fault plane and decreases with distance away from the fault plane. LPS increase for every step restored and is found to become larger in the lower reference layer. Folding is not observed prior to main fault initiation, as can be seen from the video in Appendix A.

CHAPTER 7 - DISCUSSION

7.1 Introduction

The aim of this chapter is to discuss the stress components related to fault initiation, growth and termination of thrusts. Then the deformation mechanisms observed in the modelled thrust wedge, ramp localization, thrust fault activity and the order and geometry of thrust fault formation are discussed with respect to published and reported examples in the literature. Finally, a comparison with natural fold and thrust structures will be conducted.

7.2 Stress evolution during experiments

When considering a plaster model as an unstable tectonic system, the main potential driving forces will be the body force of gravity and stress transmitted through the surroundings (moving wall) to the boundary of the system. Other forces, such as stress generated by a change in volume of a part of the system due to phase change and stress generated around suddenly developing fractures, are usually much smaller and not considered in this thesis.

7.2.1 Stress components

Before the initiation of the experiment, the horizontal and vertical stress in the box will be approximately equal (Hubbert, 1951). This state of stress is therefore said to be hydrostatic and can be expressed as:

$\sigma_1 = \sigma_2 = \sigma_3 = pgh$

In this equation, p is the density of the plaster, g is the acceleration of gravity and h is the height from the chosen point in the plaster to the surface.

Maximum shear stress is found by

$\sigma_{s\,max} = \sigma_1 - \sigma_3/2$

Thus maximum shear stress prior to the contraction is found to be 0 (since $\sigma_1 = \sigma_2 = \sigma_3$).

During modelling of the contractional regime, horizontal stress gradually increases and becomes the largest principal stress axis (σ_1) (Fig. 7.1A). There is also an

intermediate stress state (σ_2) at right angles to σ_1 and σ_3, but in a two dimensional situation it does not need to be accounted for (Hubbert, 1951). Thrust faults will form when the horizontal stress increases and the vertical (overburden) stress (σ_3) remains constant (Hubbert, 1951).

In a Mohr diagram, hydrostatic stress will only be represented by a point (Fig. 7.1B). As soon as the horizontal stress increase, the Mohr circle will grow in line with the increasing deformation. When the difference between σ_1 and σ_3 becomes larger than $\sigma_{s\,max}$, the circle will reach the failure criterion, which leads to fracturing (Fig. 7.1C). This differs from normal fault fracturing where the horizontal stress is the minimum stress (σ_3) and diminish during modelling, while the vertical stress become largest (σ_1) and remains stationary (Hubbert, 1951). In a Mohr diagram, this will plot as a fixed maximum stress and a diminishing minimum stress, which causes the radius of the circle to grow in line with increasing deformation (Fig. 7.1D), which again will lead to fracturing when the circle tangents the fracture line.

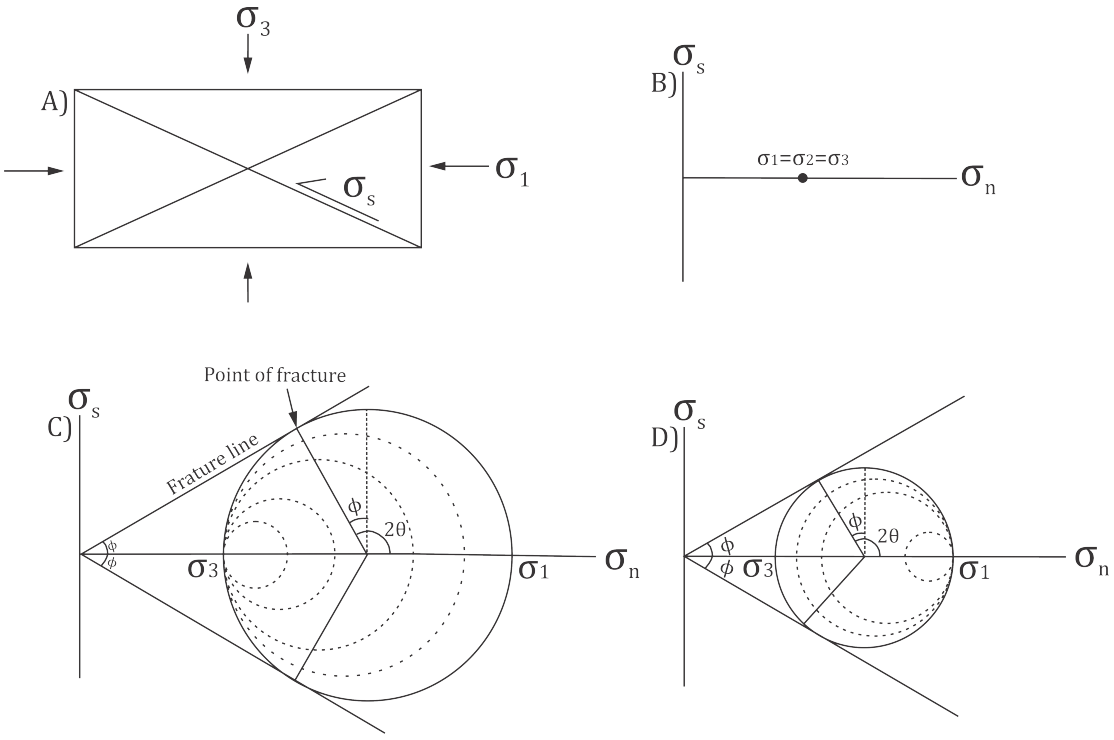

Fig. 7.1: Stress states during modelling. A) Main stress component acting on the experimental box, B) hydrostatic stress (before contraction), C) Mohr's circle during reverse fault conditions. σ_1 increases until the circle reaches fracture lines and D) Mohr's circle during normal fault conditions, σ_3 decreases until Mohr's circle reaches fractures lines. C) and D) is redrawn from Hubbert (1951).

7.2.2 Stress related to fault initiation, growth and termination

Faults will have components of normal (σ_n) and shear stress (σ_s) acting normal and parallel to the fault plane respectively. The initiation angle of a fault is found to be averagely close to 30° in the experiments (Fig. 6.2), which is in accordance to typical andersonian faulting in a contractional regime. This angle must then also be the angle between the largest principal stress and the shear plane. When looking at a Mohr diagram, the highest shear stress is found when the angle is 45° ($\theta = 45$) to the maximum principal stress (Fig. 7.2A). However, at this point, the normal stress is also large. Both the normal and shear stress will decrease as the angle (tetha, θ) increase, but the normal stress will decrease even more, which causes the material to fail into shear fractures (Fossen, 2010).

All of the experiments show a pattern of increasing fault dip with shortening, where newly accreted material in front of the wedge causes the fault blocks to rotate towards the moving wall (see subchapter 7.5.2). The rotation results in a higher dip angle, which create a higher normal stress component working on the fault surface. When plotting these new fault orientations in a Mohr circle diagram (Fig. 7.2B) it is evident that the shear stress increases a small amount relatively to the larger normal stress (Δs, Δn, Fig. 7.2), which leads to a locking position of the fault and termination of further displacement. The subsequent fault will then proceed to be the dominating component in accommodating the shortening. As new faults forms, the oldest faults will rotate and change its dip due to the rotation. The normal stress will thus become increasingly higher and more similar to σ_1 (7.2C).

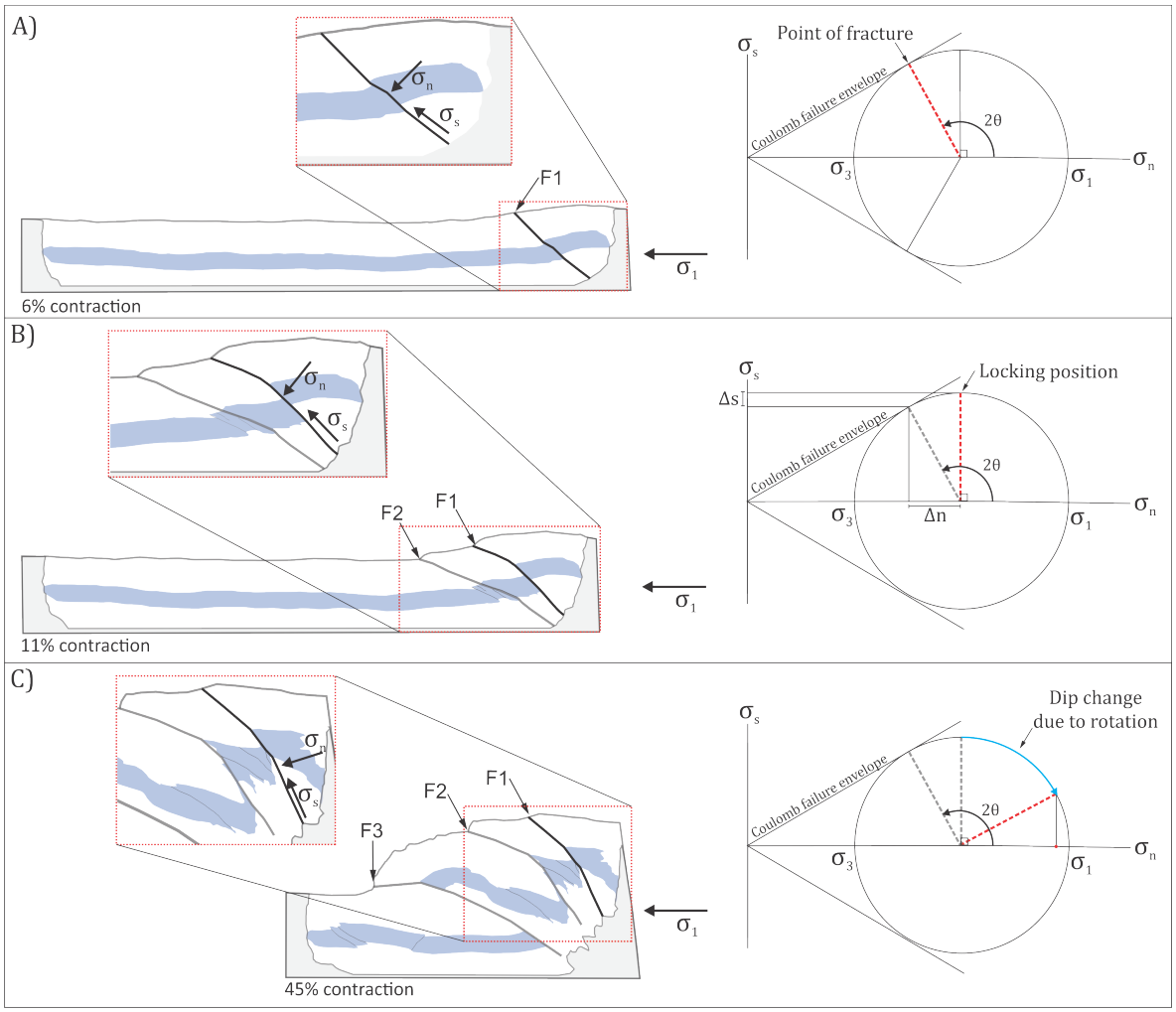

Fig. 7.2: Normal (σ_n) and shear stress (σ_s) acting at the fault plane of the first fault in experiment 27-14, after 6%, 11% and 45% contraction. A) Fault initiation, B) Locking position of the fault were displacement stops, C) increased dip angle due to imbrication at the toe of the wedge. Tetha (θ) is defined as the angle between σ_n and σ_s.

7.3 Deformation mechanisms within the contractional plaster experiments

Deformation mechanisms within a thrust wedge are different in both space and time (Mulugeta and Koyi, 1987). The dominating deformation component depends on the mechanical and petrophysical properties of the deformed material and boundary conditions. By balancing experiment 12-14 (subchapter 6.9) and analysing step-by-step developments (Chapter 5), deformation has been found to be partitioned into three deformation mechanisms; thrusting, folding and layer parallel shortening (LPS) (Fig. 7.3).

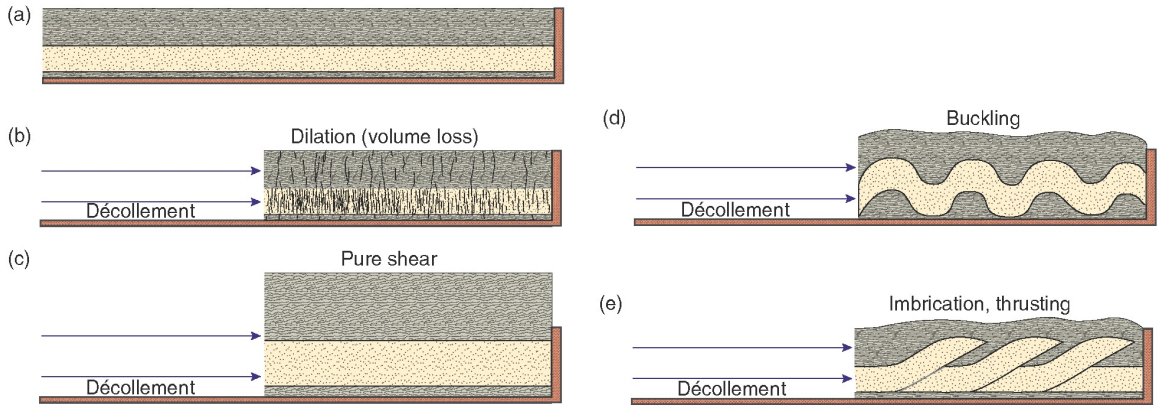

Fig. 7.3: Deformation mechanisms acting during plaster modelling. Shortening of the plaster layers can result in a wide range of structures; a) before shortening, b) dilation, c) pure shear, d) buckling and e) imbrication/thrusting. From Fossen (2010).

7.3.1 Layer parallel shortening

LPS in this study seems to be related to two different deformation mechanisms, dilation/horizontal compaction (7.3b) and pure shear (Fig. 7.3c). Horizontal compaction in the context of contractional plaster experiments is when shortening is parallel to a layer without any vertical change of height (inducing volume loss), whereas pure shear is when horizontal shortening leads to an increase in height (without folding or faulting) to compensate for the horizontal shortening (coaxial deformation with no volume loss).

In experiment 12-14, LPS was found to increase with progressive shortening, being 2% (1.3 cm) at 15% contraction, 4-5% (2.5-3.2 cm) at 34% contraction and 5-6% (3.2-3.9 cm) at 50% contraction for reference layer A and B respectively. These numbers are assumed to be a combination of both pure shear and horizontal compaction. Pure shear was primarily observed to be dominant prior to initiation of a main fault, where the plaster increased height during the shortening of the box. At later stages in the experiment, it becomes difficult to differentiate pure shear from other deformation mechanisms that accommodate shortening. LPS was found in the restoration to increase with depth of the plaster, being higher in the lower reference layer. The increased overburden in the lower part of the box may inhibit vertical

movement and result in vertical compaction of the layers, whereas in the upper layers, overburden is lesser and material can also move in the vertical direction. Horizontal compaction may occur due to excess water within the plaster, which is squeezed out prior to and during contraction in some experiments (e.g. 12-14) and induce volume loss.

LPS in natural examples are often found to be much higher than 5-6%. For instance, Cooper et al. (1983) documented that in a total shortening of 49% in a small scale duplex in a limestone quarry, LPS accommodated 27%. Higher LPS values may be an expression of chemical changes to sediment volume, this includes stylolitization, porosity reduction and impingement of grains (Pierson, 2014). These factors, as well as the natural time frame for fold and thrust belts development, are not simulated in the experiments and may be a reason for the relatively low LPS component. The relatively small amount of LPS found in experiment 12-14 is assumed to be a consequence primarily of plaster properties, which for experiment 12-14 was relatively firm and accommodated shortening by thrusting in a higher degree than LPS. One would expect that restoration of a less viscous experiment, like 15-14, would exhibit higher LPS values. Strain accumulation prior to first fault initiation can be interpreted as an indicator for LPS, which for 15-14 were 5-7% contraction, and only 1.5-3% contraction for 12-14 (Fig. 5.3 and 5.7).

7.3.2 Folding

Folding is, together with LPS, a deformation mechanism that dominates prior to fault initiation. Folding is predominant toward the surface, as is described by Koyi (1995). Fault-propagation folds were the most prevalent folds formed in the experiments (e.g. 44-14) and developed at the tip of the fault concurrently with fault displacement. Other, less common, fold types produced in the experiments were fault-bend folds that only formed in less viscous plaster (e.g. 15-14). Fault-propagation folds and fault-bend folds have been observed to appear in the same geological environment (Fig. 7.4) and are therefore believed to form in very similar lithologic and regional stress conditions (Hughes et al., 2014). Material strength play an important role in development of folds, and weaker material promotes

development of fault-bend folds (Hughes et al., 2014). This theory correlates well with observations from the experiments.

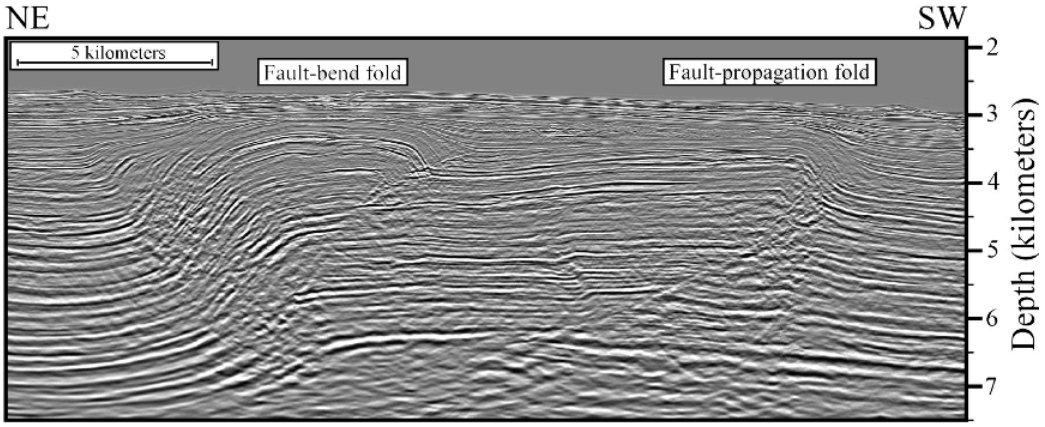

Fig. 7.4: Seismic reflection image from the offshore Niger delta, showing a fault-bend fold and a fault-propagation fold formed in similar geologic environment. From Hughes et al. (2014).

Comparing natural folds with the folds produced during modelling, several similarities are observed. Fault-propagation folds are found in Tertiary rocks in Svalbard and similarities between field, theoretical and observed structures are evident (Fig. 7.5). A large-scale field example of a fault-bend fold is the McConnell thrust sheet near Alberta, Canada. Paleozoic strata have been displaced over 5 km vertically and 40 km horizontally and now lie above Cretaceous foreland basin deposits (Fig. 7.6) (Van der Pluijm and Marshak, 2004).

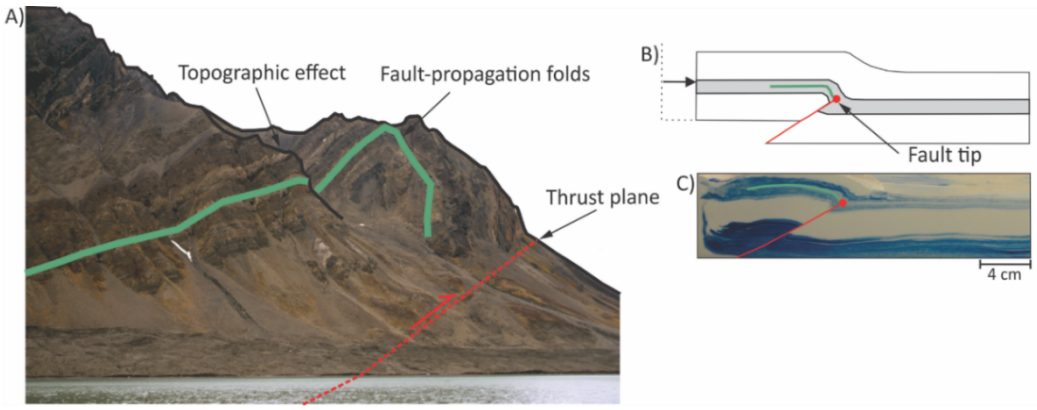

Fig. 7.5: Fault-propagation folds A) Tertary fold and thrust belt in Svalbard, Norway. From Fossen, (2010). B) theoretic sketch, redrawn from Brandes and Tanner (2014) and C) experiment 44-14, side B after 2% shortening. Red and green lines in A), B) and C) correlates.

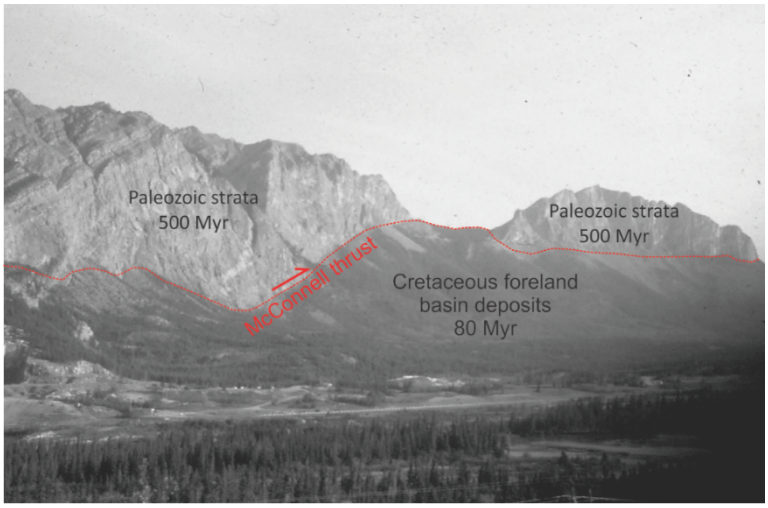

Fig. 7.6: Eroded fault-bend fold in Alberta, Canada. The McConnell thrust has displaced Paleozoic strata above younger Creaceous foreland basin deposits. Compare with fault-bend fold in figure 6.5. Photo from Van der Pluijm and Marshak (2004).

7.3.3 Faulting and domains within a wedge

Before nucleation of a thrust fault, folding and LPS are the mechanisms which accommodate shortening. However, when a fault is developed, thrusting takes over and accommodates the majority of shortening. At the start of the experiment, high amount of stress will be applied to the area closest to the moving wall and result in fault initiation. With progressive shortening, the fault will propagate up its ramp. This movement result in an increase of stress to the area in front of the fault, which now becomes closer to the moving wall. The highest amount of stress will now be applied in the footwall of the first fault, which again will lead to a creation of a new fault and thrusts are formed in-sequence. Due to termination of fault segments as new faults nucleate in an in-sequence fashion, thrust stacks are transported as piggy-back stack of thrusts by the presently active fault.

In a longitudinal cross section, the models shows a piggyback stack of thrusts and it has been documented different domains within the models throughout the experimental period. The front of the wedge was dominated by fault ramp initiation and thrust propagation, the middle was characterised by rotation and steepening of the thrust sheets, whereas the back of the wedge was dominated by vertical thickening. This pattern is best illustrated in experiment 12-14, 15-14 and 27-14

(Fig. 5.1, 5.2, 5.5, 5.6, 5.9 and 5.10). The different domains within the thrust wedge correlates well with sandbox experiments described by Mulugeta and Koyi (1987). More detailed description of thrust characteristics are described in subchapter 7.4 and 7.5.

7.4 Fault initiation and ramp evolution

Initiation of the first main fault is expected to start near the moving wall as this area firstly experience contractional forces. This theory is in coherence with observations from all the experiments described in Chapter 5. Main faults nucleated preferably at the base of the plaster and developed in concentric ellipsoids towards the surface (Fig. 7.7) (Watterson, 1986). When the ellipsoid reached the vertical glass wall, it appears as a fault (Odinsen, 1992). As the faults are only observed at the sides of the model, the nucleation point and the development path for the faults are difficult to determine (Grunnaleite, 1991). This means that even though some faults are observed to initiate at the surface (as for experiment 15-14), they might actually be initiated elsewhere and be first observed at the top of the plaster.

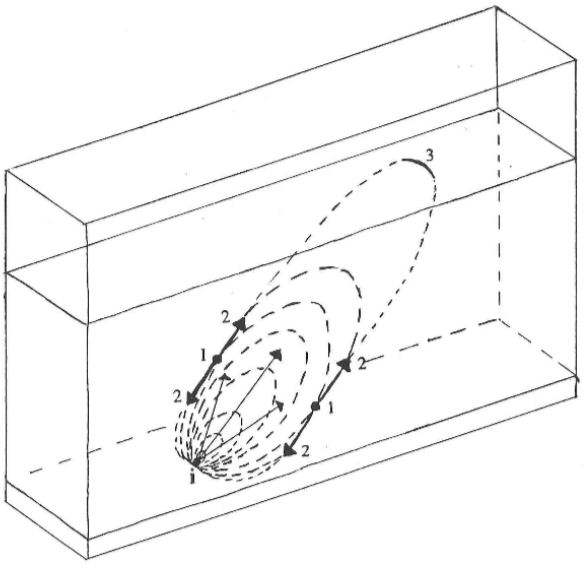

Fig. 7.7: Development of a fault plane from the bottom of the experimental box. i represents the initiation of the fault, 1 represent the faults tangent line with the side of the box, 2 represent development of the fault plane and 3 represents the fault reaching the surface. From Grunnaleite (1991).

The formation of the first fault is shown to be dependent of plaster properties; more firm plaster promotes early fault formation (e.g. at 1% contraction in experiment

45-14), while softer plaster experiments have later fault formations (e.g. 7% contraction in experiment 15-14). The differences in fault formations are seen when comparing the less viscous plaster experiment 15-14, with experiments 12-14, 44-14 and 45-14 (Fig. 6.1). The experiments with later fault formation have a higher component of LPS and folding prior to faulting, and this can be a measure of the ductility of the experiments. The formation of the first fault is expected to affect future fault development. Predicting initiation of subsequent faults is difficult and the development is affected by numerous factors (e.g. applied stress and viscosity of deforming material), which varies among the experiments. This problem is also described by Odinsen (1992). However, in experiment 45-14 a fixed barite ramp was set up prior to shortening and the ramp affected fault formation in which the faults preferred it as a propagation path. This indicates that fault development can be affected by the substrate, a theory that is applicable to nature (Zhou et al., 2007).

Throughout the experiments, faults initiated at the base of the models and propagated upwards forming a wider monoclinal fault-propagation fold in front, whereas towards the middle and end of the experiments, faults initiated as a set of conjugated shears (between 20-55% contraction) which are related to formation of pop up structures (Fig. 7.8A). This characteristic feature is also described in Mulugeta and Koyi (1992). The monoclinal shape of the thrusts suggest that nucleation occurs in a stress field where the main principal stresses are oriented obliquely to the passive layering (7.8A) (Mulugeta and Koyi, 1992).

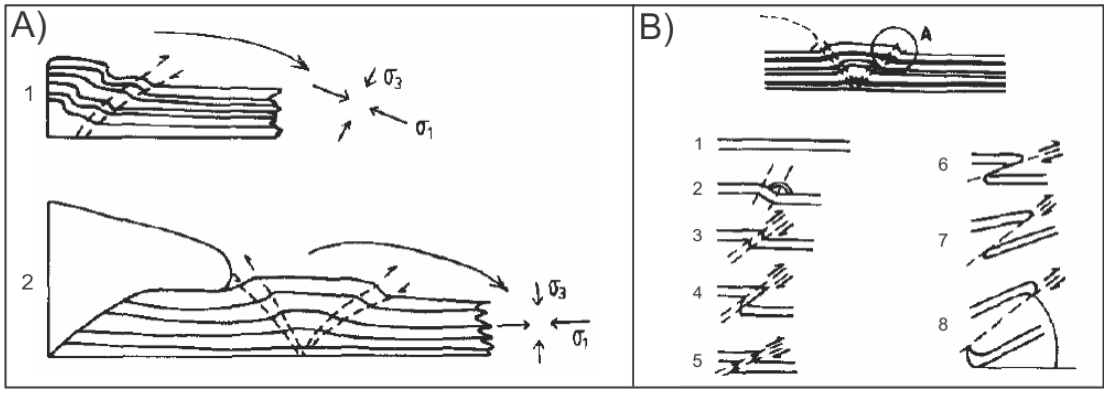

Fig. 7.8: A): Monoclinal and conjugate kink bands stress arrays, from different stages in the experiments. B): Development of a conjugate kink band from ductile shearing (stages 1-5) to localization and steepening of imbricates (stages 6-8). The dark layer in A (top) is used to illustrate. Transport direction is toward the right. Modified after Mulugeta and Koyi (1992).

After approximately 20% shortening, conjugate kink bands (Fig. 6.7) occur in more viscous experiments. Changing nucleation styles during experiments are believed to be a result of reorientation of local directions of principal stresses due to the loading conditions when the thrust sheet overrides the footwall layer (Mulugeta and Koyi, 1992). With progressive shortening, the conjugate kink zone narrows, breaks and results in a pop up structure (7.8B). The forward verging kink (i.e. the kink with dip towards the moving wall) develops faster than the back kink and result in asymmetry in the pop up, which now creates a ramp. The shear band structures and pop ups only exists for a short period before a main fault develops. Similar structures are found in nature, e.g. along the Yukon River, Alaska (Fig. 7.9) from Upper Devonian-Upper Mississippian shale and carbonates (Ellis and Dunlap, 1988).

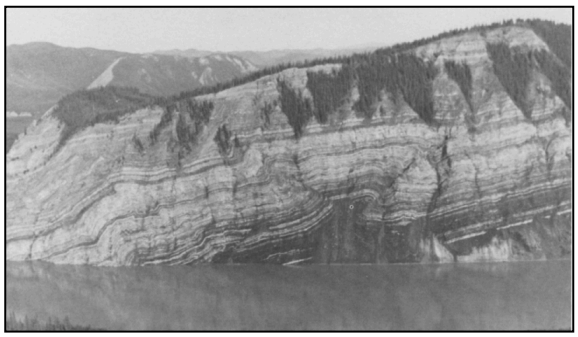

Fig. 7.9: Pop up structure along the Yukon River, Alaska. This 250 m high pop up is believed to have similar development to pop ups formed in several of the experiments. From Ellis and Dunlap (1988).

Analysis showed that the forward breaking thrust in a pop up structure had an average of 10° lower angle than the back thrust (Table 6.3). The dip angles depend on the angle between the principal stress and the décollement (ψ_b) in addition to the internal friction (Φ) of the material (Davis and Von Huene, 1987). The dip angle formulas for the fore- and back thrusts are;

$$\delta_f = 45 - \Phi/2 - \psi_b$$

$$\delta_b = 45 - \Phi/2 + \psi_b$$

This result in a higher back thrust angle (Fig. 7.10).

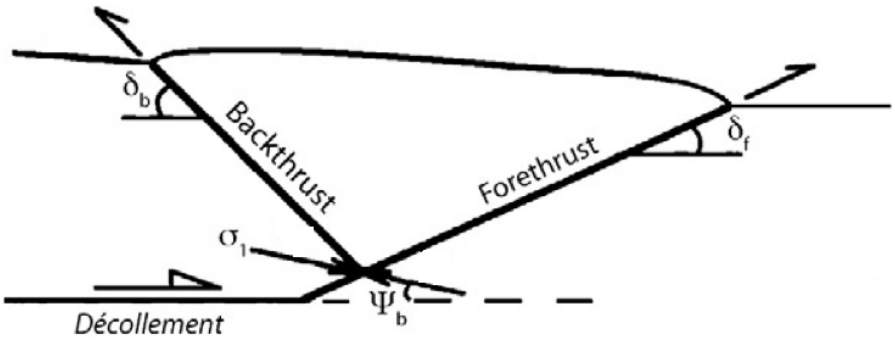

Fig. 7.10: Back- and fore thrust dip angles depend on ψ_b (see text) and the internal angle of friction. The back thrust dip angle will thus become larger. Modified after Lallemand et al., (1994).

Although most of the experiments produced pop ups, the less viscous experiment, 15-14, had no such structures. When the thrust formed, it propagated over the ramp with no back thrusting to accommodate the shortening. This implies that folding and/or LPS accommodate contraction to a higher degree and might replace back thrusting as a shortening component. The plaster did not have the consistency needed to form pop ups and back thrusts, as it appears that the plaster needs to be somewhat firm for these structures to form.

7.5 Thrust fault characteristics and associated structures

Faults investigated in this study show several similar characteristic features that are also found in sandbox modelling and in field examples.

7.5.1 Displacement and fault activity

Displacement accommodated along a fault increases during its lifetime (Table 6.2). The displacement increases with progressive shortening until reaching a maximum. As a subsequent fault is initiated, the displacement rate of the older fault decrease rapidly and the fault eventually becomes inactive. The new fault will start to accommodate shortening by continuously developing a higher displacement. Thrust slip rate is constant at the beginning of a new thrust, then gradually slowing to zero as new faults develop. Analysis of the six experiments reveals that mainly one fault is active at a certain time. However, some overlap is present, which corresponds with sandbox modelling work by Koyi (1995).

Analysis also revealed that the older faults formed the smallest displacement while younger faults created larger displacement, as seen from Table 6.2. This observation was also done by Koyi (1995) who found that the degree of displacement along imbricate surfaces decreased with age and distance away from the newly formed faults. This might be related to the solidification of the plaster, developing higher mechanical strength towards the middle and end of experiment. Progressively younger faults will therefore require higher stress for fault initiation. The active faults will allow more friction along the fault plane before initiation of the subsequent faults. However, some of the youngest faults created small displacements, which might be because they did not have time, or space, to develop, as they came close to the stable wall at the end of the experiment.

Trends of increasing active periods for progressive younger faults are found in figure 6.1. For instance, in experiment 12-14, the oldest faults had an active period of 6% while the youngest faults had an active period of up to 31% (Fig. 5.3). The increase of active periods can be explained by increase in mechanical strength of the plaster, which requires more stress for new fault initiation which again allows more friction and longer fault activity. The trend of increasing fault activity is not as apparent in experiment 15-14 (side B) were the faults have more equal active periods, and the faults are active for 2-11% contraction. This might be a result of less friction along the fault plane due to the ductile nature of the experiment and less stress is required for new fault formations.

7.5.2 Fault dip angles

The fault dip angles in the experiments are formed with an average of 29-35° (subchapter 6.3). The faults develop increasing dip angles with progressive shortening due to formation of new thrusts at the front of the wedge. Older faults will therefore have a higher rotation than the younger faults. Figure 6.2 confirm this trend by showing the evolution between initiation dip angle and dip at the end of the experiments. Some of the latest faults developed (e.g. F_4B, experiment 44-14), had high initiation dip of 41° and had a constant dip throughout the experiment. This is thought to be because the fault formed at a late stage and the stable wall

affected the nucleation. However, it could also be affected by increasing mechanical strength of the plaster, which is assumed higher at the end of experiment.

Experiments 44-14, 45-14 and 48-14 have a more complex ramp dip evolution were these experiments develop much higher rotation, as is apparent from figure 6.2. This high rotation is thought to be because the ramp is squeezed against the moving wall as the wedge builds up with increasing shortening, creating an unusual high ramp dip angle (Fig. 7.11). The increase in ramp dip for these three experiments is primarily believed to be a result of interaction with the moving wall, although new accreting material at the toe also promotes rotation.

Rotation and steepening of thrusts have been reported for sandbox experiments by Mulugeta and Koyi (1987), Mulugeta and Koyi (1992) and Koyi (1995). Koyi (1995) found that the older imbricate surfaces back rotated to almost upright position. Steepening of natural imbricate surfaces have also been reported in the Moine thrust zone in the northwest Scotland, dip ranging from 25-55° (Boyer and Elliott, 1982). The shallow dipping thrusts are found in the northeast of the zone, i.e. towards the foreland (Boyer and Elliott, 1982) whereas steepening of thrusts is found in the hinterland (Butler and Coward, 1984). Butler (1987) illustrated the steepening of the thrust sheets due to new thrusts in their footwall, and suggested that rotation was due to a longer straining history for the older thrusts.

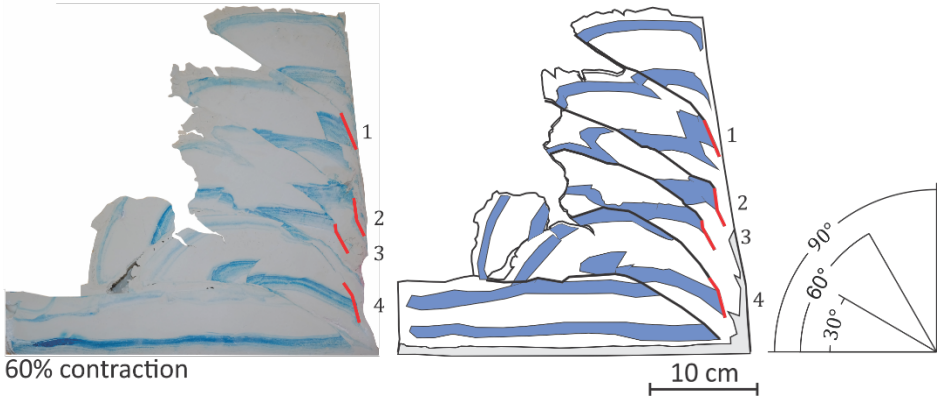

Fig. 7.11: Squeezed ramps at the end of experiment (red line), illustrated with experiment 44-14. The ramp dip angle is affected by the moving wall and believed to be unrealistic. Numbers 1-4 indicates when the faults were formed.

7.5.3 Thrust spacing

The spacing of imbricates show a trend of being close at the beginning of the experiments, varying from 2-6 cm shortening between each new thrust (see Fig. 6.3 and restored experiment Fig. 6.9-6.11). The imbricate spacing increase with progressive shortening, having a maximum of 15 cm shortening between each thrust formation. Ramp spacing is described in several papers and found to be a function of thrust sheet thickness and decreases towards the foreland, an area which is relatively thinner than the hinterland (Panian and Wiltschko, 2004). This pattern is however not observed in these experiments, although a relation between thickness and fault spacing has been documented as increased spacing of the faults are accompanied by progressive wedge height development. This relation is strengthened by the fact that faults develop underneath or in close proximity of the wedge. The pattern is most apparent in experiments with thicker plaster layer (e.g. 44-14, 45-14). The pattern described by Panian and Wiltschko (2004), has not been recognized in this study and may be due to a unrealistic growth of wedge height, plaster thickness vs. lateral length and laterally restricted development area. Increasing mechanical strength towards the end of the experiments will in addition increase stress necessary for fault initiation. Some thrusts were closely spaced towards the end of experiments and might be a result of the influence of the stable back wall, which promote earlier formation of faults and inhibit thrusts to propagate and form freely. Increasing space between imbricates is shown to result in an increase in time between each nucleation, a phenomenon also seen in several sandbox experiments (e.g. Mulugeta, 1988; Mulugeta and Koyi, 1987).

In natural settings, the basement has variable friction along the sole and/or has pre-existing basement features, which can affect the spacing of imbricates (Mulugeta and Koyi, 1987). In addition, facies changes in sediments, erosion-deposition cycles and variations in thickness above a décollement can also influence the frequency of imbricate spacing (Mulugeta and Koyi, 1987). The experiments lack the diversity of factors and influences found in nature, and may therefore not be directly transferable to nature.

7.5.4 Shear angle

Restoration of experiment 12-14 show a clear trend of higher shearing angle in the hanging wall towards the fault plane (Fig. 6.10-6.12). An explanation of the higher shear angle might be folding events in the form of fault-propagation folds, which creates a trishear zone ahead of the propagating fault. The trishear zone distribute shear in a triangular shear zone ahead of the fault, and increases the shear along the fault plane as the fault propagate towards the surface (Erslev, 1991). When the fault cuts through the fault-propagation fold, drag along the fault plane can be seen (Fossen, 2010). The drag is in most cases notably in the hanging wall (Fossen, 2010). Friction along the fault plane when the hanging wall moves over the footwall, can also be an explanation for the increased shear angles. The reconstructed shear angles is interpreted as a combination of both drag and friction.

Experiment 12-14 show increased shear at the tip of the faults. This interpretation might be due to gravitational folding of the layer when they are bent after passing the ramp.

7.5.5 Minor fault development

Minor faults are formed in the experiments under various settings. In some cases, minor faults, often in groups (Fig. 6.6C), are created prior to main fault formation. This is thought to create a zone of weakness, which influences main fault formation and propagation path (Fig. 6.6C). Faults will favour development along these weakness zones, as less stress is required for fault initiation. In field examples, weakness zones can be created by other factors than minor faults, such as evaporites, which is known as a weak stratigraphic layer. These types of weakness zones are not simulated in the experiments since the plaster is a homogenous material and no layering was created. In other cases, minor faults developed after or during main fault development. Late minor fault formation can be a result of friction along the fault plane as the fault propagates up a ramp and influence the surrounding plaster. As some of the minor faults form in the footwall, additional overlying weight from the hanging wall can promote minor fault development and be another possible trigger for the formation of minor faults (Fig. 6.6A).

A characteristic feature of the main faults is the formation of smaller faults that branch out from the major fault. As a major fault approach the surface, the fault often turn into a network of diverging minor faults, recognised as splays (Boyer and Elliott, 1982). Splays can have different geometrical relationships to the main fault (Fig. 7.12), which are explained by Boyer and Elliott (1982). Since the plaster is not transparent, an attempt to classify the splays is difficult. The deformation is divided into a wider zone as the splays reach the surface at different locations than the main fault. The deformation is seen as segments on the top of the model, which are illustrated in figure 5.25. The segments are interpreted as splays on a theoretical basis, however other explanations cannot be ruled out due to the untransparent nature of the plaster. Upwards splaying major faults are also seen on seismic images (Fig. 7.13) and when compared to experimental splaying faults (Fig. 6.9), similarities become apparent.

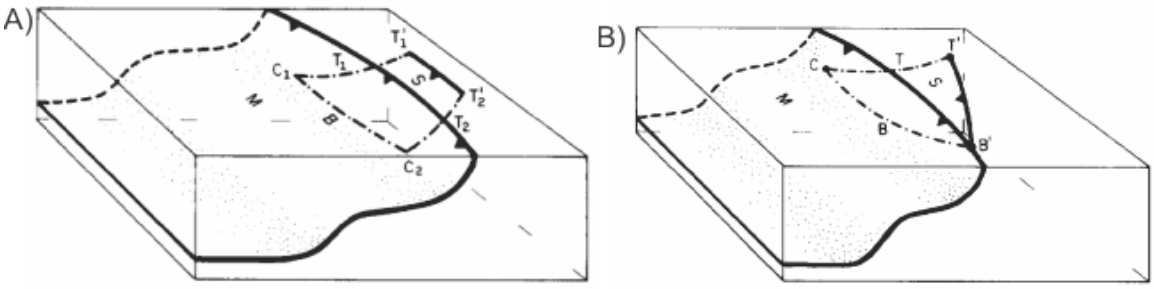

Fig. 7.12: Two classifications of splays; A) Isolated splay and B) diverging splay illustrated and explained by Boyer and Elliott (1982). M-major fault, T-tip line, S- splay, B-branch and C- corners.

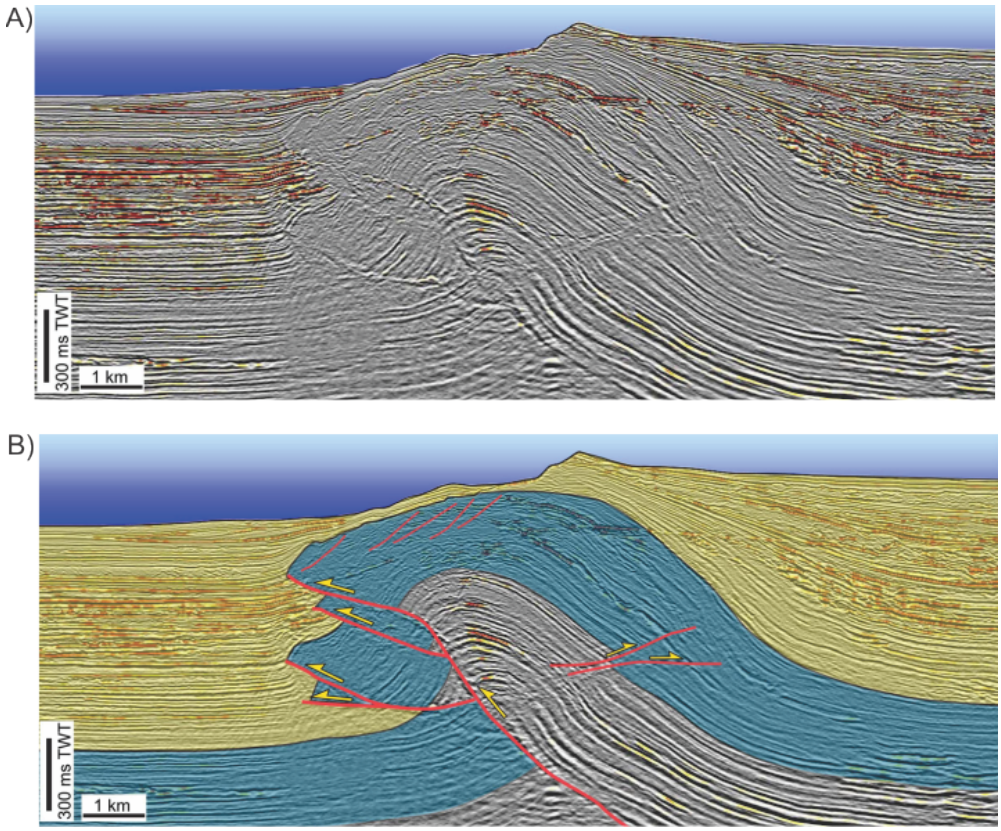

Fig. 7.13: Splaying faults on a seismic profile. A) Uninterpreted seismic image and B) interpreted. Compare with figure 6.9 in Chapter 6. Seismic profile and interpretation from Butler (2006).

7.5.6 Horizontal extension

Horizontal extension of the plaster model is restricted to the highest elevation of the thrusts and is especially clear in the less viscous experiments where extension result in normal faults development and out-of-the-hinge thrusts as seen in experiment 15-14 (Fig. 7.14). Extension happens because the rate of horizontal flow driven by gravity change with depth (Graveleau et al., 2012). Material flows faster at the surface than in the middle or at the base of the experimental box (Graveleau et al., 2012). Extension also happened in the more viscous models, which created large fractures at the surface of the models. The largest fractures where the tip of fault blocks broke off, are believed to be unrealistic structures and formed as a result of too firm plaster. Firm plaster also created cavities underneath the hanging wall.

These structures are also considered unrealistic and not possible to scale to geological reality.

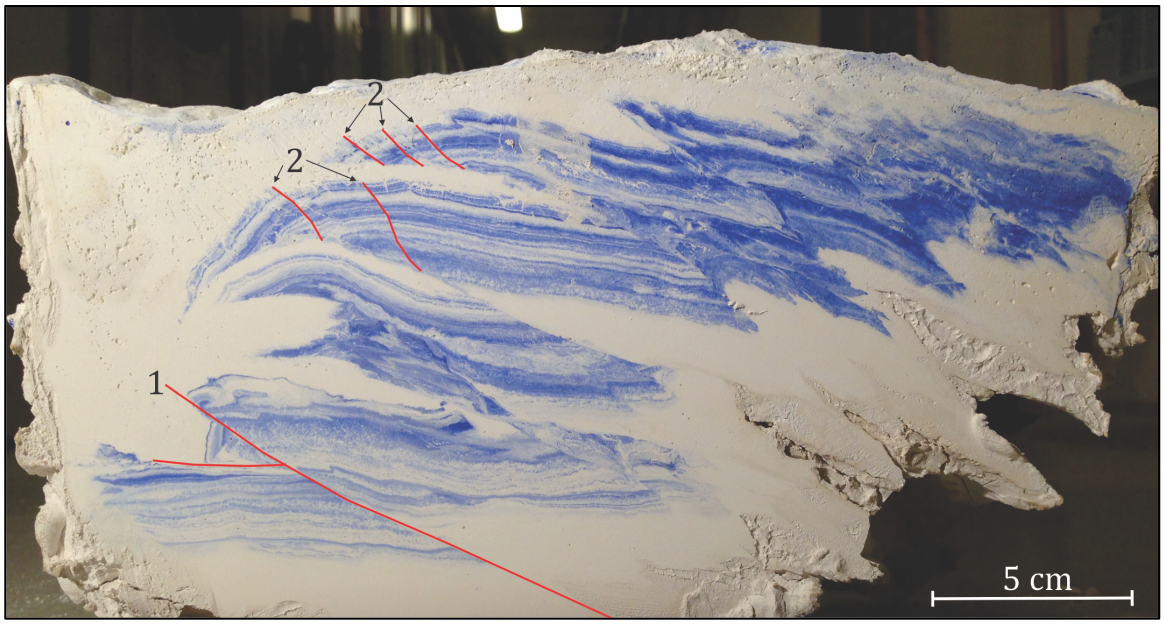

Fig. 7.14: Structures formed during horizontal extension; 1 represent out-of-the-hinge thrust and 2 represent normal faults. Both structures formed at a late stage during modelling.

7.6 Wedge geometry and critical taper

Observations throughout the experiments show that a monovergent wedge is formed, which grows in both length and height with progressive shortening. Throughout the experiment, the wedge height grew approximately linearly (Graph 6.1), as the wedge had constant supply of material. The less viscous plaster experiments had low wedge height and grew more laterally compared to the more brittle experiments, which implies that more firm plaster will produce a higher wedge. Experiment 15-14 and 27-14 were performed in a narrow box with a total start height of 6 and 7 cm, and developed an expected lower wedge height. Experiment 12-14 had approximately the same amount of plaster as 15-14 and 27-14, but in a wider box with a thicker barite basement with a total of 10 cm starting height. This created a higher and similar end wedge height as 44-14, 45-14 and 48-14 (Graph 6.1), which had a start height of 8, 9 and 8 cm respectively. Other important parameters for wedge height development might be plaster/water ratio and most importantly the degree of solidification before initiation of experiment.

The model wedge cannot represent the height of a natural wedge or mountain. In a real system, the mountain building would lead to subsidence of the Earth's crust due to isostasy where the mantel and crust is in constant equilibrium (Watts, 2001). This means that thicker crust would lead to more subsidence and only the upper part of the thickened crust would become part of the mountain range. Second, plaster modelling assumes similar strength of the material throughout the model, however it is well known that the strength of rocks increase with depth. Finally, the constant erosion and sedimentation of mountains were not simulated and the wedge could grow freely, creating an unrealistic high wedge angle.

Measurements of the wedge angle throughout the experiments are shown to vary (Graph 6.2). Variations are believed to form due to constant formation of new major thrusts. Experiment 15-14 with less viscous plaster formed a very shallow wedge angle of approximately 16°, whereas experiment 44-14, a more viscous experiment, formed a much steeper wedge of up to 62°. This implies that the geometry of the wedge is set by the strength of the deforming material; higher material strength results in higher wedge angle. The stable wall is believed to influence the wedge angle, as flow of the plaster is more restricted to a certain area. The highest decline in wedge angle of 20° is seen in experiment 45-14, from 30-35 cm shortening (Graph 6.2). From the step-by-step description in subchapter 5.6, a formation of a large fault is observed at the same time, which was formed above the ramp (Fig. 5.17-5.18). This implies that new faults will decrease the wedge angle.

The wedge angle in most experiments in this study had steeper angle than what is observed in sandbox modelling (e.g. Davis et al., 1983). Plaster is more resistant to gravitational forces as it solidifies prior to and throughout the experiment, whereas sand properties remain approximately constant throughout the experiment and the wedge form a critical taper and slide stably as material is accumulated at the toe (Davis et al., 1983). Experiment 15-14 formed a somewhat stable angle. However, most of the experiments have large variations in the wedge angle and do not show evidence for attaining a constant angle or a critical taper. Critical taper theory might

therefore not be applicable for plaster experiments as the angle is thought to primarily be governed by the properties of plaster.

7.7 Comparisons with field examples

Many orogens have characteristic features similar to those simulated in the experiments, including the Pyrenees, the Appalachians, the Alps and the Himalayas. Some of their characteristic features are difficult to attain since uplift and erosion has removed material that could provide important information (McClay and Whitehouse, 2004) and give clues about thrust activity and characteristics.

Natural thrust systems like fold and thrust belts are commonly considerably more complicated than the simple analogue models illustrated in this thesis. Several limitations during modelling are present, as mentioned by McClay and Whitehouse (2004). One important limitation is the presence of a rigid baseplate and thus no simulation of the flexural or isostatic responses of thrust stack loading and underthrusting of the lithosphere in either the hinterland or foreland. Also pore fluid pressure effects, thermal effects, competency contrasts and anisotropies were not considered in the modelling. Despite these limitations, the models are kinematic and geometric similar in many ways and give a good insight in natural fold and thrust belts.

Ketobe Knob (Fig. 7.15) is a remarkable field example where it is possible to study several small and large reverse faults in three vertical sections. The formation is a part of the Jurassic stratigraphy of the Colorado Plateau and the area is believed to have been a part of two orogenic events, the Sevier and post-Sevier Laramide orogenies (Wacker, 2001). Comparing structures found in the models with this fault zone, several similarities become apparent. First of all, the main fault plane of Ketobe Knob has upward splaying faults that distribute movement along several smaller-scale thrusts, which is also observed in the experiment during development of thrust faults (subchapter 7.5.5). The dip of Ketobe Knob is 34° (Neuhauser, 1988), which is similar to the simulated thrusts in the models which have average dip angles of 29-35° (subchapter 6.3). Other major thrusts in the area have dips of 37° and 41° (Neuhauser, 1988).

Fig. 7.15: Ketobe knob, Utah. Reverse fault zone in a fine grained sandstone and siltstone in the Entrada sandstone (lower reddish part) and Curtis formation (upper lighter part). The fault can be studied in three perpendicular vertical sections in addition to the top, and has shown to have a similar dip (34°) as formed in the experiments. (Photo by Marita Thomassen).

The Apennines in Italy is a fold and thrust belt, which presently is partially submerged under the Adriatic Sea (Fig. 7.16A) (Wu and McClay, 2011). The rear of the wedge is subaerial and has been exposed to erosion. In addition, high sedimentation completely buries the thrusts found at the front. The wedge has multiple high displacement thrusts in the rear and up to 30 km widely spaced, small displacement thrusts at the front (Wu and McClay, 2011). These resemble structures found in experiment 27-14 and also resemble structures simulated in sedimentation and erosion models by Wu and McClay (2011) (Fig. 7.16B, C). Fault-propagation folds have been formed at the front of the wedge, similar to those observed in for instance experiment 44-14 (Fig. 6.5A). There is also evidence of fault splays formed at the front limb, which are structures that resembles several of the plaster models (subchapter 7.5.5).

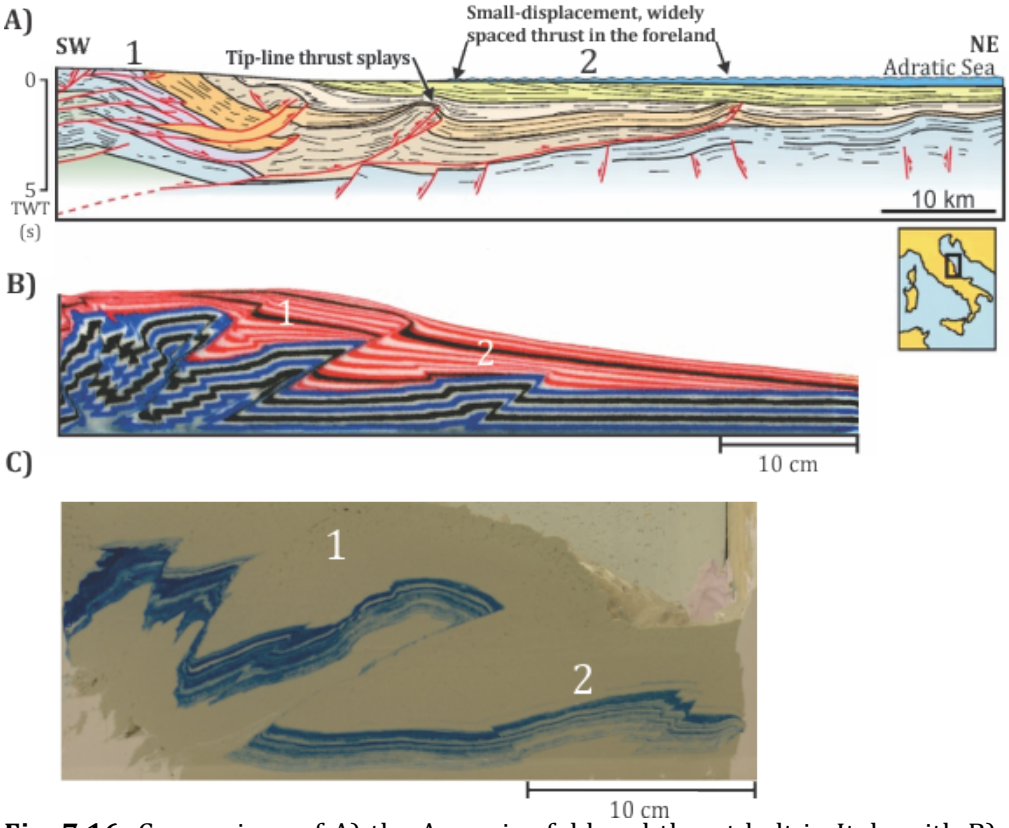

Fig. 7.16: Comparison of A) the Apennies fold and thrust belt in Italy with B) erosion and sedimentation sandbox models performed by Wu and McClay (2011) and C) plaster experiment 27-14. They show similarities by having large displacement faults (1) and small displacement faults (2). The Apennines has in addition fault-propagation folds and fault splays at the tip of thrusts, similar to structures seen in several other plaster experiments (e.g. 48-14, F_1A). A) and B) is modified from Wu and McClay (2011).

CHAPTER 8 - CONCLUSIONS

8.1 Conclusions

After a detailed analysis of six models simulating the contractional regime, similar structures to natural contractional systems have been identified and a better understanding of the sequential evolution of a thrust system is established.

The following conclusions can be drawn:

- Characteristics of contractional structures formed from plaster modelling have shown to be highly dependent on the firmness of the plaster, which is a function of plaster/water ratio, solidification time prior to experiment and duration of experiment.
- Deformation is partitioned into three deformation mechanisms; thrusting, folding and layer parallel shortening (LPS). LPS and folding dominates prior to fault formation and only constitutes a small percentage of the total shortening. LPS is also found to increase with depth.
- Different domains are recognized within the wedge; the front is dominated by fault ramp initiation and thrust propagation, the middle is characterised by rotation and steepening of faults, whereas the back of the wedge is dominated by vertical thickening and continued rotation of older faults.
- With increasing rotation of the faults, normal stress working on the fault surface increases a large amount relative to the shear stress, which leads to a locking position of the fault and termination of further displacement.
- Initiation dip of the thrusts are found to be on average 29-35° and increases due to rotation with progressive shortening as new faults are formed at the front of the wedge.
- High viscous models promote early fault development whereas less viscous models accumulate more strain before fault formation.
- Mainly one fault is active at any given time and the faults are formed in-sequence. Older faults forms less displacement than younger faults and fault spacing increase with progressive shortening.

- Throughout the experiments, faults initiated at the base of the models and propagated upwards forming a wider monoclinal fault-propagation fold in front. In the middle and towards the end (20-55% contraction), faults also initiated as sets of conjugated shears (pop ups), which developed into main faults.
- Pop up structures and back thrusts are exclusively observed in the more viscous experiments where they accommodate shortening.
- The geometry and height of the wedge is set by the mechanical strength of the plaster; higher strength results in higher wedge and wedge angle.
- Horizontal extension in the plaster models is restricted to the top of the faults and forms out-of-the-hinge thrusts and normal faults when faults are bent at a late stage during modelling.

8.2 Suggestions to further work

There are many possibilities in plaster modelling and the findings can potentially be of great value.

What if:

- Different ramp inclinations were used to see how basement irregularities influence fault development.
- Different materials were used as basement to investigate how variations in basal friction affect fault characteristics.
- 3D models of the final plaster models were made with use of 3D imaging techniques and laser scanning.

REFERENCES

ANDERSON, E. M. 1905. The dynamics of faulting. *Transactions of the Edinburgh Geological Society,* 8**,** 387-402.

AYDIN, A. & JOHNSON, A. M. 1983. Analysis of faulting in porous sandstones. *Journal of Structural Geology,* 5**,** 19-31.

BALLY, A. W., GORDY, P. & STEWART, G. A. 1966. Structure, seismic data, and orogenic evolution of southern Canadian Rocky Mountains. *Bulletin of Canadian Petroleum Geology,* 14**,** 337-381.

BOYER, S. E. & ELLIOTT, D. 1982. Thrust Systems. *The American Association of Petroleum Geologists Bulletin,* 66**,** 1196-1230.

BRANDES, C. & TANNER, D. C. 2014. Fault-related folding: A review of kinematic models and their application. *Earth-science reviews,* 138**,** 352-370.

BUITER, S. J. H. 2012. A review of brittle compressional wedge models. *Tectonophysics,* 530 531**,** 1.

BUROV, E. B. 2011. Rheology and strength of the lithosphere. *Marine and Petroleum Geology,* 28**,** 1402-1443.

BUTLER, R. 2006. *Fold-thrust complex on VERNG02_02* [Online]. Available: http://seismicatlas.org/entity?id=1768dab5-4b09-403c-aec1-4363ad59b109. Retrieved: 01.05.15

BUTLER, R. W. 1982. The terminology of structures in thrust belts. *Journal of structural geology,* 4**,** 239-245.

BUTLER, R. W. H. 1987. Thrust sequences. *Journal of the Geological Society,* 144**,** 619-634.

BUTLER, R. W. H. & COWARD, M. P. 1984. Geological constraints, structural evolution, and deep geology of the northwest Scottish Caledonides. *Tectonics,* 3**,** 347-365.

CADELL, H. M. 1889. VII.—Experimental Researches in Mountain Building. *Transactions of the Royal Society of Edinburgh,* 35**,** 337-357.

CAINE, J. S., EVANS, J. P. & FORSTER, C. B. 1996. Fault zone architecture and permeability structure. *Geology,* 24**,** 1025-1028.

CHESTER, F. M., EVANS, J. P. & BIEGEL, R. L. 1993. Internal structure and weakening mechanisms of the San Andreas fault. *Journal of Geophysical Research: Solid Earth (1978–2012),* 98**,** 771-786.

CLOOS, E. 1955. Experimental analysis of fracture patterns. *Geological Society of America Bulletin,* 66**,** 241-256.

COOPER, M. A., GARTON, M. R. & HOSSACK, J. R. 1983. The origin of the Basse Normandie duplex, Boulonnais, France. *Journal of Structural Geology,* 5**,** 139-152.

DAVIS, D., SUPPE, J. & DAHLEN, F. 1983. Mechanics of fold-and-thrust belts and accretionary wedges. *Journal of Geophysical Research: Solid Earth (1978–2012),* 88**,** 1153-1172.

DAVIS, D. M. & VON HUENE, R. 1987. Inferences on sediment strength and fault friction from structures at the Aleutian Trench. *Geology,* 15**,** 517-7613-15-6-517-12370.

DENNIS, J. G., PRICE, R. A., SALES, J. K., HATCHER, R., BALLY, A. W., PERRY, W. J., LAUBSCHER, H. P., WILLIAMS, R. E., ELLIOTT, D., NORRIS, D. K., HUTTON, D. W., EMMETT, T. & MCCLAY, K. R. 1981. What is a Thrust? What is a Nappe? *Geological Society, London, Special Publications,* 9**,** 7-9.

DENNISON, J. M. & WOODWARD, H. P. 1963. Palinspastic maps of central Appalachians. *AAPG Bulletin,* 47**,** 666-680.

ELLIOTT, D. 1976. The motion of thrust sheets. *Journal of Geophysical research,* 81**,** 949-963.

ELLIS, M. A. & DUNLAP, W. J. 1988. Displacement variation along thrust faults: Implications for the development of large faults. *Journal of Structural Geology,* 10**,** 183-192.

ERSLEV, E. A. 1991. Trishear fault-propagation folding. *Geology,* 19**,** 617-620.

FOSSEN, H. 2010. *Structural Geology,* Cambridge, Cambridge University Press.

FOSSEN, H. & GABRIELSEN, R. H. 1996. Experimental modeling of extensional fault systems by use of plaster. *Journal of Structural Geology,* 18**,** 673-687.

GABRIELSEN, R. H. & CLAUSEN, J. A. 2001. Horses and duplexes in extensional regimes: A scale-modeling contribution. *MEMOIRS-GEOLOGICAL SOCIETY OF AMERICA***,** 207-220.

GRAVELEAU, F., MALAVIEILLE, J. & DOMINGUEZ, S. 2012. Experimental modelling of orogenic wedges: A review. *Tectonophysics,* 538**,** 1-66.

GRUNNALEITE, I. 1991. *En tektonisk/kinematisk analyse av Bjørnøyrenneforkastningskomplekset, SV-Barentshavet, med spesiell vekt på den kritassiske og tertiære utviklingen : 1 : Tekst,* Bergen, I. Grunnaleite.

GWINN, V. E. 1970. Kinematic patterns and estimates of lateral shortening, Valley and Ridge and Great Valley provinces, central Appalachians, south-central Pennsylvania. *Studies of Appalachian Geology: Central and Southern.* Wiley-Interscience New York.

HALL, J. 1815. II. On the Vertical Position and Convolutions of certain Strata, and their relation with Granite. *Transactions of the Royal Society of Edinburgh,* 7**,** 79-108.

HATCHER, R. D. 1995. Structural geology : principles, concepts, and problems / Robert D. Hatcher, Jr. *Englewood Cliffs, N.J. : Prentice Hall*.

HOSSACK, J. R. 1979. The use of balanced cross-sections in the calculation of orogenic contraction: a review. *Journal of the Geological Society,* 136**,** 705-711.

HUBBERT, M. K. 1937. Theory of scale models as applied to the study of geologic structures. *Geological Society of America Bulletin,* 48**,** 1459-1520.

HUBBERT, M. K. 1951. Mechanical basis for certain familiar geologic structures. *Geological Society of America Bulletin,* 62**,** 355-372.

HUGHES, A. N., BENESH, N. P. & SHAW, J. H. 2014. Factors that control the development of fault-bend versus fault-propagation folds: Insights from mechanical models based on the discrete element method (DEM). *Journal of Structural Geology,* 68**,** 121-141.

KOYI, H. 1995. Mode of internal deformation in sand wedges. *Journal of Structural Geology,* 17**,** 293,297-295,300.

KOYI, H. A., SANS, M., TEIXELL, A., COTTON, J. & ZEYEN, H. 2004. The significance of penetrative strain in the restoration of shortened layers—insights from sand models and the Spanish Pyrenees.

LALLEMAND, S. E., SCHNÜRLE, P. & MALAVIEILLE, J. 1994. Coulomb theory applied to accretionary and nonaccretionary wedges: Possible causes for tectonic erosion and/or frontal accretion. *Journal of Geophysical Research: Solid Earth (1978–2012),* 99**,** 12033-12055.

MANDL, G. & CRANS, W. 1981. Gravitational gliding in deltas. *Geological Society, London, Special Publications,* 9**,** 41-54.

MANSFIELD, C. & CARTWRIGHT, J. 2001. Fault growth by linkage: observations and implications from analogue models. *Journal of Structural Geology,* 23**,** 745-763.

MCCLAY, K. 1990. Extensional fault systems in sedimentary basins: a review of analogue model studies. *Marine and petroleum Geology,* 7**,** 206-233.

MCCLAY, K. & WHITEHOUSE, P. 2004. Analog modeling of doubly vergent thrust wedges.

MCCLAY, K. R. & ELLIS, P. G. 1987. Geometries of extensional fault systems developed in model experiments. *Geology,* 15**,** 341-7613-15-4-341-12339.

MUGNIER, J.-L., HUYGHE, P., LETURMY, P. & JOUANNE, F. 2004. Episodicity and rates of thrust-sheet motion in the Himalayas (western Nepal).

MULUGETA, G. 1988. Modelling the geometry of Coulomb thrust wedges. *Journal of Structural Geology,* 10**,** 847-859.

MULUGETA, G. & KOYI, H. 1987. Three-dimensional geometry and kinematics of experimental piggyback thrusting. *Geology,* 15**,** 1052-1056.

MULUGETA, G. & KOYI, H. 1992. Episodic accretion and strain partitioning in a model sand wedge. *Tectonophysics,* 202**,** 319-333.

NEUHAUSER, K. R. 1988. Sevier-age ramp-style thrust faults at Cedar Mountain, northwestern San Rafael swell (Colorado Plateau), Emery County, Utah. *Geology,* 16**,** 299-7613-16-4-299-6294.

ODINSEN, T. 1992. *Modellering av normalforkastninger; analoge ekstensjons-gipsmodeller og balansering,* Bergen, [T. Odinsen].

OTTESEN, S. 1991. Den strukturelle utviklingen av Swaengraben, og dens implikasjoner for struktureringen av Lopphøgda med omgivelser. Bergen: S. Ottesen.

PANIAN, J. & WILTSCHKO, D. 2004. Ramp initiation in a thrust wedge. *Nature,* 427**,** 624-627.

PIERSON, N. 2014. Assessing Layer Parallel Shortening in the Eastern Colorado Front Range Using Thin Section Analysis and Analog Sandbox Models.

POBLET, J. & LISLE, R. J. 2011. Kinematic evolution and structural styles of fold-and-thrust belts. *Geological Society, London, Special Publications,* 349**,** 1-24.

PRICE, R. & MOUNTJOY, E. 1970. Geologic structure of the Canadian Rocky Mountains between Bow and Athabasca Rivers—a progress report. *Structure of the southern Canadian Cordillera: Geological Association of Canada Special Paper,* 6**,** 7-25.

RAMBERG, H. 1981. *Gravity, deformation and the earth's crust: in theory, experiments and geological application*, Academic Press London.

RAMBERG, I. B., SOLLI, A., NORDGULEN, Ø., BINNS, R., GROGAN, P. & NORSK GEOLOGISK, F. 2008. *The Making of a land : geology of Norway,* Trondheim, The Norwegian Geological Association.

RAMOS, V. A., ZAPATA, T., CRISTALLINI, E. & INTROCASO, A. 2004. The Andean thrust system - latitudinal variations in structural styles and orogenic shortening.

ROWAN, M. G., PEEL, F. J. & VENDEVILLE, B. C. 2004. Gravity-driven fold belts on passive margins.

SAINT-GOBAIN. 2015. *Molda 3 Normal* [Online]. Available: http://www.saintgobainformula.com/Products/Plaster/Molda-3-Normal. Retrieved: 03.03.15

SALES, J. K. 1987. Tectonic models. *Structural Geology and Tectonics.* Springer.

SCHMIDT, C. J., GENOVESE, P. W. & CHASE, R. B. 1993. Role of basement fabric and cover-rock lithology on the geometry and kinematics of twelve folds in the Rocky Mountain foreland. *Geological Society of America Special Papers,* 280**,** 1-44.

STEYRER, H.-P. 2009. Teaching principal plate tectonic processes by means of analogue modeling. *Studia UBB, Geologia,* 54**,** 13-16.

TWISS, R. J. & MOORES, E. M. 1992. *Structural geology,* New York, Freeman.

VAN DER PLUIJM, B. A. & MARSHAK, S. 2004. *Earth structure: an introduction to structural geology and tectonics*, New York: WW Norton; 2nd ed.

VEKINIS, G., ASHBY, M. & BEAUMONT, P. 1993. Plaster of Paris as a model material for brittle porous solids. *Journal of Materials Science,* 28**,** 3221-3227.

WACKER, M. A. 2001. Geometries and kinematics of thrust related drag folds: an example from the San Rafael Swell, Central Utah.

WALSH, J. J. & WATTERSON, J. 1988. Analysis of the relationship between displacements and dimensions of faults. *Journal of Structural Geology,* 10**,** 239-247.

WATTERSON, J. 1986. Fault dimensions, displacements and growth. *Pure and Applied Geophysics,* 124**,** 365-373.

WATTS, A. B. 2001. *Isostasy and Flexure of the Lithosphere*, Cambridge University Press.

WILCOX, R. E., HARDING, T. T. & SEELY, D. 1973. Basic wrench tectonics. *AAPG Bulletin,* 57**,** 74-96.

WILTSCHKO, D. V. & GROSHONG, R. H. 2012. The Chamberlin 1910 balanced section: Context, contribution, and critical reassessment. *Journal of Structural Geology,* 41**,** 7-23.

WU, J. E. & MCCLAY, K. R. 2011. Two-dimensional analog modeling of fold and thrust belts: dynamic interactions with syncontractional sedimentation and erosion.

YAMADA, Y., BABA, K. & MATSUOKA, T. 2006. Analogue and numerical modelling of accretionary prisms with a decollement in sediments. *Analogue and Numerical Modelling of Crustal-Scale Processes,* 253**,** 169-183.

ZHOU, J., XU, F., WEI, C., LI, G., YU, F. & TONG, H. 2007. Shortening of analogue models with contractive substrata: Insights into the origin of purely landward-vergent thrusting wedge along the Cascadia subduction zone and

the deformation evolution of Himalayan–Tibetan orogen. *Earth and Planetary Science Letters,* 260**,** 313-327.

ØYGAREN, M. 2002. Analoge modellforsøk i gips: sammensatte ekstensjonsforkastninger. Bergen: M. Øygaren.

APPENDIX A

Table A: Videos of the experiments.

Experiment nr.	File	Experiment date	Length (sec)	Size (MB)
12-14, side A	12-14, side A.mov	29.01.14	38	43.3
12-14, side B	12-14, side A.mov	29.01.14	32	46
15-14, side A	15-14, side A.mov	07.02.14	43	37.7
15-14, side B	15-14, side B.mov	07.02.14	45	40.9
27-14, side A	27-14, side A.mov	22.10.14	32	33.5
27-14, side B	27-14, side B.mov	22.10.14	32	45.1
44-14, side A	44-14, side A.mov	03.12.14	79	58.4
44-14, side B	44-14, side B.mov	03.12.14	68	57.3
45-14, side A	45-14, side A.mov	04.12.14	28	32.6
45-14, side B	45-14, side B.mov	04.12.14	53	45.5
48-14, side A	48-14, side A.mov	04.12.14	36	33.7
48-14, side B	44-14, side B.mov	04.12.14	36	36.5

APPENDIX B

Table B: Data for figure 6.2. Fault initiation dip angles and dip angles at the end of experiment measured along the ramp. Letters A and B represents sides of development.

Experiment nr.	Faults side A	Fault initiation dip	Dip angle at the end of experiment	Faults Side B	Fault initiation dip	Dip angle at the end of experiment
12-14	1A	38	48	1B	40	47
	2A	31	39	2B	36	40
	3A	34	36	3B	38	39
	4A	47	47	4B	49	51
15-14	1A	27	55	1B	27	42
	2A	31	40	2B	20	31
	3A	20	29	3B	21	35
	4A	20	21	4B	20	22
	5A	23	23	5B	27	30
				6B	24	28
27-14	1A	36	66	1B	32	51
	2A	26	43	2B	31	52
	3A	35	36	3B	34	35
	4A	32	39	4B	31	35
44-14	1A	26	69	1B	26	74
	2A	32	74	2B	36	59
	3A	31	61	3B	37	78
	4A	40	50	4B	41	41
	5A	38	46			
45-14	1A	36	87	1B	36	86
	2A	33	46	2B	37	62
	3A	31	37	3B	32	48
	4A	41	46	4B	35	51
	5A	31	33	5B	31	36
	6A	37	42			
48-14	1A	35	74	1B	30	76
	2A	26	64	2B	36	56
	3A	25	58	3B	30	71
	4A	34	55	4B	30	58
	5A	27	31	5B	32	33